Surface Plasmon Polariton Mediated Coupling of Cavity Modes in Nanostructured Slit Arrays Analyzed by Electron Energy Loss Spectroscopy in a Transmission Electron Microscope

Zur Erlangung des akademischen Grades eines
DOKTORS DER NATURWISSENSCHAFTEN
von der Fakultät für Physik
des Karlsruher Institutes für Technologie (KIT)

genehmigte
DISSERTATION
von

Dipl.-Phys. Roman Michael Walther
aus Dresden

Tag der mündlichen Prüfung 16.01.2015

Referentin: Prof. Dr. D. Gerthsen
Korreferent: Prof. Dr. K. Busch

angefertigt am
Laboratorium für Elektronenmikroskopie (LEM)
Karlsruher Institut für Technologie (KIT)

Table of Contents

List of Acronyms

ADF	Annular dark-field
Ag	Silver
AS	Anti-symmetric
Au	Gold
BF	Bright field
CCD	Charge-coupled device
DGTD	Discontinuous Galerkin Time Domain
EDXS	Energy-dispersive x-ray spectroscopy
EELS	Electron energy loss spectroscopy
EFTEM	Energy-filtered transmission electron microscopy
EOT	Extraordinary optical transmission
FEM	Finite element method
FFT	Fast-Fourier transformation
FIB	Focused ion beam
FWHM	Full width at half maximum
Ga	Gallium
HAADF	High-angle annular dark-field
LSP	Localized surface plasmon
MANDOLINE	Magnetic aberration-free noticeably dispersive Omega-like inhomogeneous energy
PSF	Point-spread function
PVD	Physical vapor deposition
RL	Richardson-Lucy (algorithm)
S	Symmetric
SESAM	Sub-electron sub-angstrom microscope
Si	Silicon
SP	Surface plasmon
SPP	Surface plasmon polariton
STEM	Scanning transmission electron microscopy
TE	Transversal electric
TEM	Transmission electron microscopy
TIA	TEM Imaging and Analysis (Microscope software)
TM	Transversal magnetic
ZLP	Zero-loss peak

List of Symbols

a	Lattice period	
a_0	Bohr's radius	$0.529\ 177\ 210\ 92\ (17) \cdot 10^{-10}$ m
$\mathbf{B}$	Magnetic induction	
c	Speed of light in vacuum	299 792 458 m/s
χ	Electronic susceptibility	
d	Inter-slit/inter-hole distance	
$\mathbf{D}$	Electric displacement	
$\delta(r)$	Delta function	
d/λ	Coupling parameter	
e	Electron charge	$-1.602\ 176\ 565(35) \cdot 10^{-19}$ C
$\mathbf{E}$	Electric field	
$\varepsilon(\omega)$	Dielectric function	
ε_0	Vacuum permittivity	$8.854\ 187\ 817 \cdot 10^{-12}$ F/m
E_0	Electric field amplitude	
ε_1	Real part of the dielectric function	
ε_2	Imaginary part of the dielectric function	
ε_d	Permittivity of the dielectric	
$\varepsilon_m(\omega)$	Permittivity of the metal	
E_n	Cavity mode energy of order n	
$\mathbf{F}$	Force	
Φ	SPP phase difference	
$\phi(\mathbf{r},t)$	Electrostatic potential	
$\mathbf{G}$	Reciprocal lattice vector	
γ	Free electron gas damping constant	
h	Planck constant	$4.135\ 667\ 616(91) \cdot 10^{-15}$ eV s
$\mathbf{H}$	Magnetic field	
$\hbar = h / 2\ \pi$	Reduced Planck constant	$6.582\ 119\ 28(15) \cdot 10^{-16}$ eV s
$\mathbf{k}$	Wave vector	
k'	Real part of the wave vector	
k''	Imaginary part of the wave vector	
k_0	Wave vector in vacuum	
$k_{1,2}$	Evanescent SPP wave vector	
L	Slit length	
λ	Wavelength	

λ_n	Cavity mode wavelength of order n	
L_{SPP}	SPP propagation length	
m	Effective electron mass	
m_0	Electron rest mass	$9.109\ 382\ 91(40) \cdot 10^{-31}$ kg
μ_0	Vacuum permeability	$4\ \pi\ \cdot 10^{-7}$ N/A^2
n	Mode order of the cavity modes	
n_e	Number of electrons per unit volume	
n_i	Iteration number of the RL algorithm	
π	Circle constant	3.141 592 6
P	Polarization	
q	Scattering vector	
$q_\perp$	Component of the scattering vector perpendicular to v	
r	Position	
σ	Surface charge density	
τ	Relaxation time of the electron plasma	
t	Time	
v	Electron velocity	
ω	Angular frequency	
ω_c	Cutoff wavelength	
ω_n	n^{th} harmonic of a cavity mode	
ω_P	Plasma frequency	$[n_e\ e^2 / (\varepsilon_0\ m)]^{1/2}$
ω_{SP}	Surface plasmon frequency	
x	Electron position	
Z	Atomic number	

1 Introduction

Fundamental effects and applications based on the excitation and interaction of surface plasmons, i.e. collective excitations of valence band electrons, in metals are summarized in a modern field of physics denoted as plasmonics. It allows the directing and manipulating of light at the sub-wavelength nanoscale.[1-3] This field has becomes more and more important in everyday life. In nature, plasmonics is responsible for iridescent and color-rich beetle carapaces[4]. Ancient artisans unknowingly employed nanoparticles as coloring agents for glasses. A prominent example is the Lycurgus Cup which was crafted in the fourth century AD.[5] The cup appears green if it is illuminated from outside, however, if a candle is placed in the cup, it appears red. This effect is related to the collective excitation of localized surface plasmons (LSP) supported by alloyed Au-Ag nanoparticles within the glass. Excitation of LSPs results in reflected green light for outside illumination. However, for illumination from within the cup, the green part of the light is absorbed by the LSP resonance and thus the cup will appear red in color.

The technological relevance of surface plasmons, alternatively also denoted as surface plasmon polaritons (SPP), also steadily increases. Plasmonic sensors are widely applied in everyday life in the form of nanobiosensors[6] in. e.g. household pregnancy tests. Plasmon-related effects enable Raman spectroscopy to probe single molecules.[7] Plasmonic circuitry[2, 3] is paramount for the ongoing miniaturization of electronic devices as classic electronics approach fundamental physical limits in miniaturization due to reaching length scales on which quantum effects arise. The discovery of the effect of extraordinary optical transmission (EOT) through sub-wavelength hole arrays in thin metal films by Ebbesen et al.[8] drew a lot of attention to this field. Although this effect is still not yet completely understood, it is accepted that SPPs play an important role in the light transmission characteristics. Light impinging on the hole array generates SPPs on the metal film which can propagate indirectly through the film by inducing SPPs within the slits and re-emit light on the other side of the metal film. Therefore the transmission coefficient normalized to the hole area may even exceed unity. A vast number of studies were reported on this EOT effect, however, the majority only investigated the transmission as a whole by applying light-optical techniques. To gain a deeper insight into the particular processes involved in EOT, the various aspects have to be considered separately.

In the present work, the excitation and coupling of SPPs across slit arrays was investigated. Instead of using light-optical techniques, scanning transmission electron microscopy (STEM) was applied in combination with electron energy loss spectroscopy (EELS). The high spatial resolution in STEM allows positioning the electron beam in a specific slit of the nanostructure with nanometer precision. The beam electrons excite SPPs in this particular slit. The energy loss associated with the SPP excitation can be measured by EELS. In addition to the SPP excitation, a resonant cavity

mode is generated in the slit as a result of hybridization of the two. The initial basic structure analyzed in this work is a single nanostructured slit of size 180 x 900 nm. A double-slit system consisting of two of these slits is the starting point for further investigations because strong enhancement of the cavity modes occurs. An important slit parameter is the slit length which was varied between 400 nm and 2.5 μm. The effect of length variation on the cavity mode energy is studied. Together with two-dimensional intensity profiles of the cavity modes, the dispersion relation of the hybridized cavity modes is determined. The coupling is determined by the metal bar width between the slits which was varied systematically from 100 nm to double the slit length in this work. The cavity mode enhancement is studied with respect to the distance between slits. Symmetric and anti-symmetrically coupled modes in the two slits are detected depending on the inter-slit distance. The coupling effects are also studied in slit systems consisting of up to 60 slits. In addition to next-neighbor coupling, collective oscillations of the array as a whole are hinted.

In chapter two, a brief summary of the theoretical background on plasmons and the resonances emerging in slits in a metal film is given. A short description of the employed electron microscopy techniques follows. Chapter three focuses on the experimental acquisition and processing methods. The experimental results and their discussion are presented in Chapter four. The effects of changing the slit size, inter-slit separation, and number of slits on the coupling of SPP are studied in separate sub-sections. Chapter five will summarize the experimental results and their implications briefly.

2 Fundamentals

This chapter describes theoretical background of plasmonic excitations and resonant cavities which is essential understand the physical processes that govern the experimental findings presented in the following chapters. First, various types of plasmons are discussed, i.e. volume and surface plasmons and as a particular case the emergence of surface plasmon polaritons. The description of the resonances occurring in cavities in a thin metal film follows.

The second part of this chapter contains the description of the employed experimental methods and devices, i.e. STEM and EELS. For the latter one, a short overview of the different acquisition and data processing methods will be given.

2.1 Plasmonic Excitations

The following paragraphs will only briefly describe the physical processes involved in plasmonic oscillations and will follow the derivation of Egerton[9] and Maier.[10] The interested reader is referred to these textbooks for a deeper understanding of the matter.

2.1.1 Volume Plasmons

In a metal, the electrons in the valence band essentially behave like free particles that are not bound to the ion-core lattice. An effective mass *m* will be attributed to the electron to phenomenologically incorporate the minor effects associated by the ion-core lattice. The electrons are driven by an external oscillating electric field and hence also oscillate. This oscillation is damped by collisions and is incorporated via a damping constant γ which is related to the relaxation time τ of the electron plasma via $\gamma = 1 / \tau$. This relaxation time is typically in the order of 10^{-14} s at room temperature.[10]

The movement of an electron at position **x** in the plasma can be described by a simple equation of motion

$$m\ddot{\mathbf{x}} + m\gamma\dot{\mathbf{x}} = -e\mathbf{E}\,, \tag{2.1}$$

where e is the electron charge. If the applied electric field has a harmonic time dependence of $\mathbf{E}(t) = E_0 \exp(i\omega t)$, a solution of (2.1) will be of the form:

$$\mathbf{x}(t) = \frac{e}{m(\omega^2 + i\gamma\omega)}\mathbf{E}(t). \tag{2.2}$$

The displacement **x** will result in a polarization $\mathbf{P} = -e\, n_e\, \mathbf{x} = \varepsilon_0\, \chi\, \mathbf{E}$ where n_e is the number of electrons per unit volume and χ is the electronic susceptibility. The resulting relative permittivity or dielectric function of the electron plasma follows from (2.2) as

$$\varepsilon(\omega) = \varepsilon_1 + i\varepsilon_2 = 1 + \chi = 1 - \frac{\omega_p^2}{\omega^2 + i\gamma\omega}, \tag{2.3}$$

where $\omega_p = [n_e\, e^2 / (e_0\, m)]^{1/2}$ is the plasma frequency of the free electron gas. (2.3) can be discussed with respect to the ratio of the angular frequency ω and the damping frequency γ, although as of now limited to the case where $\omega < \omega_p$. For frequencies near ω_p, the damping becomes negligible and (2.3) reduces to

$$\varepsilon(\omega) = 1 - \frac{\omega_p^2}{\omega^2}. \tag{2.4}$$

Equation (2.4) is the dielectric function of the undamped free electron plasma as given from the Drude model of the free electron gas. However, in the case of noble metals, significant alterations to the Drude model occur because of interband transitions which will add to the imaginary part of the dielectric function. On the other hand, for very low frequencies, where $\omega << \gamma$, the imaginary part of (2.3) will be dominant. Therefore, the metal is mainly absorbing in this frequency regime.

To discuss the frequency regime where $\omega > \omega_p$, the electromagnetic wave equation has to be considered. Combining the two curl equations of Maxwell's equations without external factors, i.e. $\nabla \times \mathbf{E} = -\partial\mathbf{B}/\partial t$ and $\nabla \times \mathbf{H} = \partial\mathbf{D}/\partial t$, the wave equation is

$$\nabla \times \nabla \times \mathrm{E} = -\mu_0 \frac{\partial^2 D}{\partial t^2} \tag{2.5}$$

$$\mathbf{k}(\mathbf{k} \cdot \mathbf{E}) - k^2 \mathbf{E} = -\varepsilon(k, \omega) \frac{\omega^2}{c^2} \mathbf{E} \tag{2.6}$$

in the time and the Fourier domain where **k** is the wave vector. (2.6) yields the dispersion relation for transversal waves (where $\mathbf{k} \cdot \mathbf{E} = 0$):

$$k^2 = \varepsilon(\mathbf{k}, \omega) \frac{\omega^2}{c^2}. \tag{2.7}$$

Inserting the dielectric function of (2.4), the dispersion relation becomes

$$\omega^2 = \omega_p^2 + k^2 c^2. \tag{2.8}$$

It follows that transverse electromagnetic waves cannot occur for $\omega < \omega_p$ but are allowed for $\omega > \omega_p$. The case $\omega = \omega_p$ is quite interesting as in the case of negligible damping, the dielectric function

(2.4) $\varepsilon(\omega) = 0$ and hence the electronic susceptibility $\chi = \varepsilon(\omega) - 1$ becomes -1. This yields to $\mathbf{E} = -\mathbf{P}/\varepsilon_0$, i.e. the electric field becomes a pure depolarization field. Inserting $\varepsilon(\omega) = 0$ in (2.6) leads to $\mathbf{k}\,(\mathbf{k} \cdot \mathbf{E}) = k^2 \cdot \mathbf{E}$ which is trivially fulfilled if $k = 0$ or if $\mathbf{k} \parallel \mathbf{E}$, i.e. for a longitudinal wave. Therefore, the excitation at $\omega = \omega_p$ corresponds to a collective longitudinal wave of the electron plasma. In a macroscopic picture, this collective excitation can be described as following:

If all electrons in a slab of metal are displaced by **s**, a surface charge density of $\sigma = \pm n_e\, e\, s$ at the slab boundaries normal to the displacement **s** arises. A homogeneous electric field of strength $E = n_e\, e\, s / \varepsilon_0$ emerges in the slab and leads to a restoring force $\mathbf{F} = -e \cdot \mathbf{E}$ acting on the displaced electrons. The resulting equation of motion for all electrons is

$$n_e m \ddot{\mathbf{s}} = -\frac{n_e^2 e^2 \mathbf{s}}{\varepsilon_0} \tag{2.9}$$

$$\ddot{\mathbf{s}} + \omega_p^2 \mathbf{s} = 0 \tag{2.10}$$

Therefore, the plasma frequency is the natural frequency of free oscillations of the electron plasma. The quanta of these oscillations are quasi-particles called plasmons or rather in this case volume plasmons in order to distinguish them from other possible excitations of the electron plasma like surface plasmons and surface plasmon polaritons which will be discussed in the next paragraph.

2.1.2 Surface Plasmons and Surface Plasmon Polaritons

Electromagnetic excitations propagating at the interface of a dielectric and a metal are called surface plasmons (SP) or surface plasmon polaritons (SPP). These excitations rely on the interaction of the electric field inside the dielectric and oscillations of the electron plasma in the metal and are evanescently confined in the directions normal to the interface. It is noted that there is no standard naming convention for these excitations which share a common dispersion relation that will be discussed in this chapter. In this work, however, surface plasmons and surface plasmon polaritons are separated by their wave vector with respect to the dispersion. For large wave vectors k, the excitation will be called a surface plasmon and for small wave vectors k a surface plasmon polariton. For the sake of simplicity, throughout the derivation of the dispersion relation, the term SPP will be solely used.

Starting point for the derivation of the dispersion relation of SPPs is again the wave equation (2.5) which simplifies to

$$\nabla^2 \mathbf{E} + k_0^2 \varepsilon \mathbf{E} = 0 \tag{2.11}$$

with $k_0 = \omega/c$ as the wave vector in vacuum and a harmonic time dependence of the electric field in the form of $\mathbf{E}(\mathbf{r},t) = \mathbf{E}(\mathbf{r})\exp(i\omega t)$. The following geometry will be used for the further derivation:

the SPP propagates along the x direction, the plane z=0 coincides with the interface and the system is invariant in the y direction leading to $\varepsilon(r) = \varepsilon(z)$. The propagating wave can now be written as $\mathbf{E}(\mathbf{r}) = \mathbf{E}(z)\exp(ik_x x)$ with k_x as the propagation constant (or wave vector). The wave equation (2.11) then reads as follows

$$\frac{\partial^2 \mathbf{E}(z)}{\partial z^2} + (k_0^2 \varepsilon - k_x^2)\mathbf{E} = 0. \tag{2.12}$$

A similar wave equation also exists for the magnetic field **H**. Both wave equations in addition to the Maxwell equations are then employed to derive the different field components at the interface. The half space $z > 0$ describes the dielectric of permittivity ε_d and $z < 0$ the metal with permittivity $\varepsilon_m(\omega)$. For transversal-magnetic (TM) polarization, the field components in the dielectric are

$$H_y(z) = A_2 \mathrm{e}^{ik_x x}\mathrm{e}^{-k_2 z}, \tag{2.13}$$

$$E_x(z) = iA_2 \frac{1}{\omega \varepsilon_0 \varepsilon_d} k_2 \mathrm{e}^{ik_x x}\mathrm{e}^{-k_2 z}, \tag{2.14}$$

$$E_z(z) = -A_1 \frac{\beta}{\omega \varepsilon_0 \varepsilon_d} \mathrm{e}^{ik_x x}\mathrm{e}^{-k_2 z}. \tag{2.15}$$

The corresponding components inside the metal are

$$H_y(z) = A_1 \mathrm{e}^{ik_x x}\mathrm{e}^{k_1 z}, \tag{2.16}$$

$$E_x(z) = -iA_1 \frac{1}{\omega \varepsilon_0 \varepsilon_d} k_1 \mathrm{e}^{ik_x x}\mathrm{e}^{k_1 z}, \tag{2.17}$$

$$E_z(z) = -A_1 \frac{\beta}{\omega \varepsilon_0 \varepsilon_d} \mathrm{e}^{ik_x x}\mathrm{e}^{k_1 z}. \tag{2.18}$$

Where $k_i = k_{z,i}$ is the wave vector component perpendicular to the interface and describes the evanescent decay into the dielectric and metal. H_y and $\varepsilon_i \cdot E_z$ must be continuous across the interface which leads to $A_1 = A_2$ and $k_2/k_1 = -\varepsilon_d/\varepsilon_m$. In addition, H_y has to fulfill the wave equation

$$\frac{\partial^2 H_y}{\partial z^2} + (k_0^2 \varepsilon - k_x^2) H_y = 0. \tag{2.19}$$

The final result is the dispersion of SPP propagating along the interface between metal and dielectric

$$k_x(\omega) = k_0 \sqrt{\frac{\varepsilon_m(\omega)\varepsilon_d}{\varepsilon_m(\omega)+\varepsilon_d}}. \tag{2.20}$$

The equations (2.13) - (2.18) can also be written for transversal-electric (TE) polarization but the continuity across the interface in this case leads to the condition $A_1 = A_2 = 0$. Therefore, SPPs only exist for TM polarization.

k_x is a complex value and can be decomposed via $k_x = k_x'(\omega) + ik_x''(\omega)$. The real part dictates the SPP wavelength as

$$\lambda_{SPP} = \frac{2\pi}{k_x'(\omega)}, \tag{2.21}$$

whereas the imaginary part is related to the propagation length in the propagation direction as

$$L_{SPP} = \frac{1}{2k_x''(\omega)}. \tag{2.22}$$

The dispersion relation of SPP at the interface between air ($\varepsilon_d = 1$) and a lossless metal that can be described by the dielectric function (2.4) inserted into (2.20) and is shown in Figure 2.1.1.

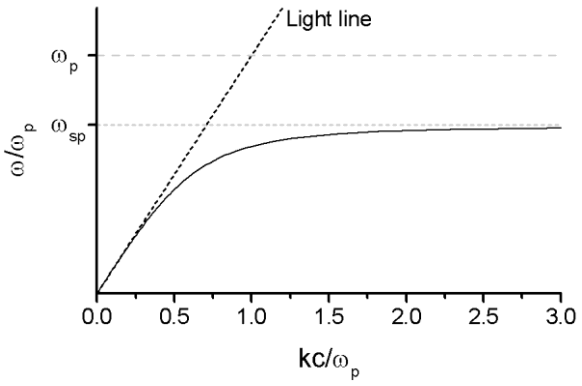

Figure 2.1.1 Calculated SPP dispersion relation for the interface of a Drude model metal (with dielectric function (2.4)) and air ($\varepsilon_d = 1$). The black dotted line represents the light line, the grey dotted line the surface plasmon frequency and the grey dashed line the plasma frequency.

For small values of the wave vector k, the dispersion relation closely follows the light line. In this wave vector regime, the excitation is therefore mostly polaritonic and therefore this branch of the dispersion relation corresponds to surface plasmon polaritons. For large k values however, the dispersion relation deviates more and more from the light line and approaches the fixed surface plasmon frequency at

$$\omega_{sp} = \frac{\omega_p}{\sqrt{1+\varepsilon_d}}. \tag{2.23}$$

In this branch of the dispersion relation, the excitation is characterized as a pure surface plasmon. The dispersion relation is, however, always on the right side of the light line and hence SPPs

cannot couple to light. This is of course expected as no bound surface state would exist if they could directly couple to light. The excitation of SPP with light therefore always needs additional momentum in order to fulfill the momentum conservation. A periodic lattice can provide this momentum via the reciprocal lattice vector, for example. Another possibility is the coupling via a prism.[11, 12] In this case, a prism is attached to the metal film. Inside the prism, the light line will be shifted towards the right in the dispersion relation of Figure 2.1.1. Then the dispersion relation intersects the light line and SPPs can be excited.

2.2 Resonant Cavities in a Thin Metal Film

A single slit in a thin metal film is an electromagnetic resonator, similar to a slot antenna. Due to reflection of the electromagnetic fields at the slit walls, the modes within such a resonant cavity will be standing waves. A simple geometry of such a cavity is shown in Figure 2.2.1.

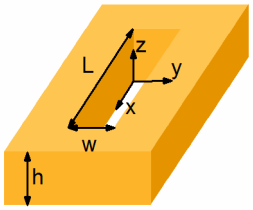

Figure 2.2.1 Geometry of a single slit in a metal film.

The cavity is a slit of size L x w in a perfectly conducting metal film with height h. The cavity is filled by a dielectric, in the simplest case air. So in principle, the cavity is a rectangular wave-guide of length h. In free space, a solution of the wave equation (2.5) will be of the form:

$$\mathbf{E}(\mathbf{r}, t) = \mathbf{E_0} e^{i(\omega t - \mathbf{kr})}. \tag{2.24}$$

Inside the cavity, the electric field must fulfill the boundary condition at the interfaces between metal and dielectric, i.e. the transversal component of the electric field must vanish at x = 0 and x = L as well as at y = 0 and y = w.[13] As standing waves are expected within in the cavity, the spatial dependence of the two components of the electric field in the film plane can be described by trigonometric functions. In the z-direction, the field is not constricted by the film and hence will remain a general solution similar to (2.24). The fields can then be written as:

$$E_x = E_{x,0} \cos k_x x \sin k_y y \, e^{i(\omega t - k_z z)} \tag{2.25}$$

$$\mathrm{E}_y = \mathrm{E}_{y,0}\, sin\, k_x x\, cos\, k_y y\, \mathrm{e}^{i(\omega t - k_z z)} \tag{2.26}$$

$$\mathrm{E}_z = -i\mathrm{E}_{z,0}\, sin\, k_x x\, sin\, k_y y\, \mathrm{e}^{i(\omega t - k_z z)}. \tag{2.27}$$

The condition that E_x vanishes at y = 0 is trivially fulfilled for a sine function. For E_x to vanish at y = L, k_y has to fulfill the condition $k_y = \pi\, n_y / L$ with n_y as an integer value which also denominates the mode order. The similar conditions apply for k_x, i.e. $k_x = \pi\, n_x / w$. Given these constraints on k_x and k_y, the E_z field also vanishes at the cavity walls and hence no constraints are imposed on k_z. Fulfilling the wave equation (2.5) as well as the Maxwell equations (in this case $\nabla \cdot \mathbf{E} = 0$) leads to a dispersion relation in the form of:

$$k_x^2 + k_y^2 + k_z^2 = \tfrac{\omega^2}{c^2}. \tag{2.28}$$

For the wave guide to support traveling waves, k_z has to be real and hence $k_z^2 \geq 0$. Therefore a minimum frequency for a propagating wave exists and is called the cut-off wavelength of the wave guide defined by the dispersion relation (2.28) as:

$$\omega_c = \pi c \sqrt{\frac{n_x^2}{w^2} + \frac{n_y^2}{L^2}}. \tag{2.29}$$

On the other hand, the wave guide may also support oscillations below this frequency. Then however, k_z will be imaginary and hence the field component variation along z will be evanescent. For the present work, the cavity modes associated with the long slit walls of length L hybridize with the SPPs.[14] Therefore, only the wave vector component k_y is of interest. The dispersion relation (2.28) can then be used to calculate the wavelength

$$\lambda_n = \frac{2\pi}{k_y} = \frac{2L}{n} \tag{2.30}$$

as well as the energy

$$E_n = \frac{hc}{\lambda_n} = \frac{hcn}{2L} \tag{2.31}$$

of the cavity modes. For a slit length of L = 960 nm, the fundamental cavity mode (n_y = 1) will yield a wavelength of 1920 nm and an energy of 0.646 eV. Similarly, the energy of the mode associated with the slit width w can be derived and is 3.444 eV. This energy is larger than the surface plasmon energy of Au at 2.4 eV[15]. As no SPP exist above the surface plasmon energy (cf.

Figure 2.1.1) this cavity mode will not interfere with SPP and the sole focus on the cavity mode associated with the slit length L with respect to hybridization is justified

2.3 Scanning Transmission Electron Microscopy

Scanning transmission electron microscopy (STEM) is a serial image acquisition technique in which a highly focused electron beam is scanned across the specimen area of interest. The condenser system of a transmission electron microscope that normally forms a broad beam to illuminate a specimen area in transmission electron microscopy (TEM) can also be used to create a highly focused electron beam. Above the sample, two pairs of deflection coils are arranged perpendicular to each other which scan the electron beam across the area of interest. In contrast to TEM, no additional image forming lens system is necessary below the specimen in STEM. The electrons in the scanning beam can be elastically and inelastically scattered by interaction with the specimen which results in an angular distribution of the scattered electrons. The scattering angle depends on the interaction in the specimen. An angular detector located beneath the specimen discriminates the electrons by their scattering angle and thereby allows forming images containing information depending on the scattering angle.

A common detector design consists of three detector areas centered on the optical axis of the microscope. The central bright-field (BF) detector only detects unscattered electrons or electrons with small scattering angles and therefore forms a bright-field image. Electrons with intermediate scattering angles are collected by the annular dark-field (ADF) detector. The ADF detector is surrounded by the high-angle annular dark-field (HAADF) detector which only collects electrons with large scattering angles. Therefore the image intensity in HAADF STEM images strongly depends on the atomic number Z and the thickness of the sample. Based on the differential Rutherford scattering cross-section, a Z^2 dependence of the scattering angle can be assumed. This is only a rough estimate, for example, Crewe[16] proposed a $Z^{3/2}$ dependence. If the specimen thickness and density is constant in a given specimen region, the image intensity in the HAADF STEM image unambiguously corresponds to heavier elements. Therefore, HAADF STEM imaging is also referred to as Z-contrast imaging.[17]

The annular detector arrangement allows simultaneously acquiring images and performing spectroscopy. Characteristic X-rays emitted by the specimen due to interaction with the beam electrons can be detected by a detector above the sample and allows performing energy-dispersive X-ray spectroscopy. In addition, the BF detector can be retracted and the beam of unscattered and weakly scattered electrons can be analyzed in an electron energy loss spectrometer attached to the microscope. This allows extracting spectroscopic information for each scanning position of the image. For a more detailed description of STEM, the interested reader is referred to the standard textbooks, e.g. by Williams and Carter[18] or Reimer.[19]

2.4 Electron Energy Loss Spectroscopy

Electron energy loss spectroscopy (EELS) retrieves spectral information on the interaction of electrons with the specimen by analyzing the energy loss of the electrons. The electrons interact with the specimen matter by electrostatic, Coulomb forces resulting in scattering of the electrons. Their momentum is changed and they can transfer a considerable amount of energy to the specimen. The scattering can be categorized in elastic and inelastic scattering.

The former category results from interaction of the electron with an atomic nucleus which constitutes a high concentration of charge. The Coulomb interaction of the electron with the nucleus charge is the stronger the nearer the electron passes the nucleus and results in large scattering angles. This is the classic Rutherford scattering. However, as described in section 1.1, electrons with large scattering angles are collected by the HAADF detector and therefore do not contribute to the EELS spectrum. Electrons with small scattering angles can still reach the EELS spectrometer, but, as they are elastically scattered and therefore do not lose energy, they contain no information with respect to EELS.

Inelastic scattering of the beam electrons occurs when they interact with the atomic electrons in the specimen. The interaction with an inner-shell electron can result in the transition of this electron into an unoccupied, higher-energy state. Due to energy conservation, this ionization energy has to be provided by the fast beam electron. The ionization energy respectively the energy loss of the fast electron is characteristic for different elements and, hence, information on the chemical composition of the specimen can be retrieved. In combination with STEM, 2-dimensional element maps can be acquired. The ionized target atom rapidly returns to its ground state by a transition of an electron in an outer shell into the unoccupied state. The energy gained by this transition can lead to the emission of characteristic X-ray photons (used for EDXS). Alternatively it can be transferred to another atomic electron which is emitted as an Auger electron.

The interaction with outer-shell electrons can result in inter-band and intra-band transitions. In insulators and semiconductors, a valence band electron can be excited across the band gap into the conduction band. The corresponding deexcitation to the ground state may result in catholuminescence or thermal dissipation of the energy. If the final state of the transition lies above the vacuum level and enough energy is transferred to the outer-shell electron to reach the sample surface, it can be emitted as a secondary electron.

The interaction of the beam electrons with the specimen is not restricted to single-electron excitation. Collective excitations in the form of volume and surface plasmons which are described in section 2.1 can arise through the interaction with beam electrons as well. A broad overview of the various optical excitations arising in an electron microscope is given in a review paper by García de Abajo.[20]

In the following, it will be shown how the energy loss per unit length in the specimen can be related to the imaginary part of the dielectric function. The derivation is described detailed in the textbook by Egerton.[9] The electron passing through the specimen represents a time-dependent charge distribution in the form of $-e\delta(\mathbf{r} - \mathbf{v}t)$ with a corresponding electric field which induces an electric field $\mathbf{E}_{ind}$ in the specimen that acts against the electron.

The moving charge distribution of the electron generates a spatial and time-dependent electrostatic potential $\phi(\mathbf{r},t)$ that satisfies the Poisson equation

$$\varepsilon_0 \varepsilon(\boldsymbol{q}, \omega) \nabla^2 \varphi(\boldsymbol{r}, t) = e\delta(\boldsymbol{r}, t). \tag{2.32}$$

The stopping power, i.e. the energy loss per unit path, acting on the electron is identical to the force acting on the electron in the direction of motion. The force can be calculated:

$$F(\boldsymbol{r}, t) = e \cdot \frac{\partial}{\partial_z} \varphi(\boldsymbol{r}, t) = e \cdot E_z^{ind}(\boldsymbol{r}, t) \tag{2.33}$$

where E_z^{ind} is the z-component of the induced electric field. In other words, EELS is only sensitive to the electric field in the electron's direction of motion. The stopping power, i.e. the energy loss per distance, can then be calculated by Fourier transformations:

$$\frac{dE}{dz} = \frac{2\hbar^2}{\pi a_0 m_0 v^2} \iint \frac{q_\perp \omega \mathrm{Im}[-\frac{1}{\varepsilon(q,\omega)}]}{q_\perp^2 + \left(\frac{\omega}{v}\right)^2} dq_\perp d\omega \tag{2.34}$$

where the angular frequency ω is given by $E / \hbar$ and $q_\perp$ is the component of the scattering vector q. The imaginary part of $[-1/\varepsilon(q,w)]$ is the so-called energy-loss function. It provides a complete description of the material response through which the electron passes. Based on this derivation, the optical response of a medium can be assessed by EELS through Kramers-Kronig analysis[9] and allows to probe[21] the various plasmons described in section 2.1.

From the experimental point of view EELS is combined with STEM by attaching a spectrometer below the sample and the two annular detectors. The bright-field detector is retracted and the transmitted beam reaches the spectrometer. This setup is a so-called post-column filter as the spectrometer is located below the microscope column. The electron beam is dispersed with respect to the electron energy by a magnetic prism. Depending on the energy loss, the electrons are deflected differently by the magnetic prism and an EELS spectrum is formed at a plane behind the magnetic prism. The spectrum is subsequently magnified and projected on a CCD (charge-coupled device) camera which records the spectrum. The strength of the magnetic field in the prism is variable and allows changing the dispersion of the spectrometer. The stronger the magnetic field

the finer the electron beam is dispersed. The energy resolution of the spectrum is thereby enhanced as smaller energy losses can be resolved.

A special kind of spectrometers are called imaging filters which allow inserting a slit aperture in the exit plane of the prism where the spectrum is located. Depending on the width of the slit and its position with respect to the spectrum, an energy range can be selected. Only electrons with an energy loss in the selected energy range pass the energy-selecting slit. The electron optics of the spectrometer form an image containing only the electrons selected by the slit. If, for example, the selected energy range coincides with a specific core-loss of an element present in the sample, the formed image directly shows this element's distribution within the sample. This technique is called energy-filtered transmission electron microscopy (EFTEM).[22]

As mentioned above, the energy resolution of the spectrum can be improved by increasing the spectrometer dispersion. This is not the only parameter related to the energy resolution. The electron optics in the spectrometer which project the spectrum on the CCD camera are subject to aberrations and may therefore hamper the energy resolution. However, the energy spread of the electron source in the employed (scanning) transmission electron microscope has the strongest impact on energy resolution. For a typical Schottky field-emission gun, the energy spread is about 0.7 eV[18] and poses a limit on the attainable energy resolution. To overcome this limit, electron monochromators can be incorporated in the microscope column. A common electron monochromator is a Wien filter.[23, 24] It consists of the superposition of magnetic and electric fields through which the electrons propagate. The fields are perpendicular to each other and the electron beam. Their polarities are chosen so the electrostatic and magnetic forces on the electrons are in opposite directions. For a given electron energy, the field strengths can be adjusted so that the combined net force of the electrostatic and magnetic forces are zero; the electron passes through the Wien filter without any deflection. Electrons whose energies differ from this particular energy are however deflected. As a result, the electron beam is dispersed with respect to the energy similar to the magnetic prism in an EELS spectrometer. Also similar to the spectrometer, a slit aperture can be inserted perpendicular to the dispersion into the plane containing the dispersed electron beam. Thereby only electrons with a specific primary energy are allowed to pass. In this manner, the energy spread in the electron beam can be reduced and as a result, the energy resolution of EELS spectra is improved.

STEM EELS is a viable tool for the investigation of the plasmonic resonances of nanostructured materials. Early studies have reported bulk and surface plasmons,[25-28] whereas a lot of more recent studies have focused on the LSP resonances of single and coupled metallic nanoparticles.[29-34] In addition to the improved lateral resolution of STEM EELS, it offers another advantage as it can probe optically dark modes.[35] An optically dark mode occurs for example between two nanoparticles whose LSP couple anti-symmetrically. Excitation of such a system by optical means

will only couple to the symmetric mode of the two nanoparticles as the phase of the incoming electromagnetic field will be identical for both particles if their diameter is small compared to the wavelength. On the other hand, STEM EELS is 'blind'[36] to the optical hot spots[37] that are responsible for, e.g., surface enhanced Raman spectroscopy.[7] In the case of a nanoparticle dimer, the hot spot is located in the gap between the two nanoparticles and is related to the symmetrically coupled mode which results in a strong electromagnetic field in the gap. STEM EELS, however, only excites the anti-symmetrically coupled mode if the electron beam is located between the nanoparticles and thus cannot probe the hot spot. EFTEM has also been shown to resolve single nanoparticle LSP resonances[38-40] and plasmonic modes of nanoholes in metal films.[41, 42] Also more complex nanostructures like split ring resonators which play a crucial role in optical metamaterials due to their mixed capacitive and inductive response[43, 44] can be studied with STEM EELS.[45] The interested reader is referred to review papers[46-48] and references therein for a more detailed overview of metal nanoparticle plasmonics.

3 Experimental Details

STEM was performed with an aberration-corrected FEI Titan³ 80-300 operated at 300 keV (FEI, Hillsboro, Oregon, USA). It is equipped with a Wien-type filter electron monochromator which reduces the energy spread of the Schottky field-emission gun from 0.65 eV to 0.12 eV for short exposure times of 10 ms. With an optimal alignment, an energy resolution of 0.11 eV can be achieved. The attached post-column imaging filter, a GIF Tridiem 865 HR (Gatan, Pleasanton, California, USA), was used to acquire EELS spectra. It is operated with the highest available dispersion of 0.01 eV per channel. Prior to STEM EELS experiments, the Au films are plasma-cleaned by air plasma or mixed oxygen/argon plasma for 3 minutes.

3.1 EELS Acquisition Methods

Basically, two acquisition methods were employed in this work, i.e. point measurements with manual setting of the beam position for each spectrum acquisition and secondly, automated line scans. The point measurements consist of 50 single spectra that were acquired with 10 ms dwell times and a dispersion of 10 meV per channel. As the microscope and spectrometer alignments are not stable, the energy axis (i.e. the position of the ZLP) changes between individual measurements. Therefore, prior to summation, the energy axis has to be calibrated for each single spectrum. The energy calibration is applied via a self-written script in Digital Micrograph's own scripting language. Spectra acquired with this technique have, compared to spectra obtained with the integrated dwell time (500 ms) of the single measurements, improved signal-to-noise ratio due to the summation of individual spectra. Additionally, the energy resolution is improved as the drift of the spectrum on the spectrometer CCD is on a larger time scale than the measurements. Typically, it is about 110 to 120 meV. Further reduction of the dwell time only results in minor improvement of the energy resolution.

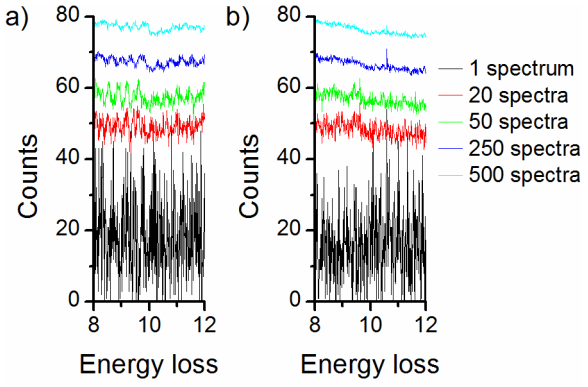

Figure 3.1.1 Comparison of summation of spectra obtained with a) standard acquisition and b) binned-gain averaging. Spectra were obtained with the specimen retracted from the microscope column and are shifted vertically to each other for better visibility.

The effects of summation of different numbers of individual spectra are shown in Figure 3.1.1a. Spectra were obtained with the specimen retracted from the microscope column. Therefore the intensity variations in the depicted energy range are only due to the dark-field signal (i.e. the signal without electron illumination) of the CCD pixels. The overall noise level is reduced for increasing numbers of summed spectra but the quality improvement of the spectra is limited. The desired result is a flat line without any intensity variations. However, even the spectrum resulting from the summation of 500 spectra shows minor bumps. These bumps may be related to the gain-to-gain variation of individual pixels, i.e. if a pixel gives a significantly different signal than its neighbors although all pixels are illuminated equally. Normally, the gain variation should be corrected by acquiring dark-field reference images for which the whole CCD camera should be equally illuminated. However, dark-field images are difficult to obtain for the particular experimental requirements, i.e. the investigation of weak plasmon signals directly adjacent to the intense zero-loss peak (ZLP) of the spectrum. Typically, a plasmon peak only adds up to about 50 counts whereas the ZLP exceeds 60,000 counts. An dark-field reference image optimized for plasmons would have to be acquired for a similar count rate. However, the automated routine of the microscope software that acquires dark-field images does not support such low count rates because the built-in count threshold to check whether the CCD is illuminated is set to high. Therefore, the routine will simply stop and will not acquire a correct dark-field reference image. As a compromise, a dark-field reference will be acquired for a higher count rate although this may lead to the observed bumps in the spectrum. Following the above line of argumentation, the gain-to-gain variation should be restricted to single pixels. However, the observed bumps stretch over a range of about 10 to 15 pixels. The explanation for this lies in the energy drift of the spectrometer system. The drift is centered on the initial zero loss peak position and varies according to a

Gaussian distribution. For large numbers of summed spectra, this predominant distribution leads to the bumps in the spectrum as single noisy pixels on the CCD camera smear out into a peak-like feature.

The so-called binned-gain averaging method proposed by Bosman and Keast[49] is a viable tool to circumvent these detrimental effects of summation over a large number of individual spectra. It consists of deliberately shifting the spectrum on the CCD camera to an even larger extent than the inherent drift of the measurement system. As the superimposed energy-shift distribution is uniform, the artifacts described in the previous section do not occur as seen in Figure 3.1.1b. The overall noise ratio is also directly related to the number of summed spectra, similar to the standard acquisition method. However, the spectra approach the desired shape, i.e. a flat line. Also the gain variation from pixel to pixel on the CCD is evened out by this method. In addition to the energy shift, the CCD camera is highly binned in the non-energy-dispersive direction which results in a significant increase of the readout speed of the CCD's electronics. Binned-gain averaging is employed with a Digital Micrograph script.

The second acquisition method is used to obtain line scans along desired specimen areas. The line scans are carried out automatically by the microscope software TIA (FEI). The beam is scanned along a user-defined line and a predefined number of spectra are acquired along this line. Typically, a measurement was performed every 2 nm. Due to software limitations, the minimal dwell time is 50 ms, i.e. significantly higher than the exposure time of the high-quality point measurements obtained with binned-gain averaging. As a result, the data quality is reduced. Especially the energy resolution is degraded due to this comparably high dwell time, because the spectrum is more severely affected by energy drift and spectrometer instabilities. Under these circumstances, the best achievable energy resolution is 150 meV. Additionally, binned-gain averaging cannot be combined with the automated line scan acquisition as the script is not supported by TIA. The line scan is repeated at least ten times at the same position to improve the signal-to-noise ratio. Energy drift and, if needed, spatial drift correction is applied prior to summation of the individual scans. Spatial drift may occur as a single line scan takes up to ten seconds to complete.

Despite these disadvantages compared to the point measurements, line scans are performed as they facilitate the visualization of the spatial distribution of the energy losses. Line scans are always represented as 2D maps where the color-coded energy-loss intensity is plotted as a function of position and energy loss as shown in Figure 3.1.2. The observed signals correspond to the first four cavity modes and the surface plasmon in a microstructured slit and are discussed in detail in Chapter 4 on page 29.

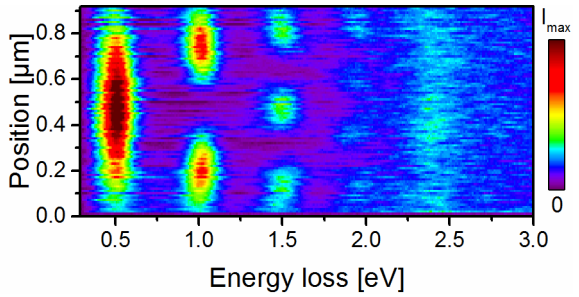

Figure 3.1.2 Color-coded EELS intensity from a line scan as a function of the energy loss and the position along the long slit axis.

Such a line scan does not only show the spatial distribution of the signals, it also allows wavelength measurements of the observed cavity modes. EELS is sensitive to the anti-nodes of the oscillating electric field in the cavity. As the distance between two anti-nodes is equal to half of the wavelength of the related oscillation, the cavity-mode wavelengths are equal to twice the distance between adjacent intensity maxima.

3.2 Data Processing with the Richardson-Lucy Algorithm

The development of sophisticated EELS spectrometers[50, 51] and electron monochromators[52] led to the improvement of energy resolution to values below 30 meV[53-56]. However, the accessible range of signals with low energy losses is still limited due to the extended tail of the ZLP which masks weak low-loss signals. Further improvement of the energy resolution is still needed to access these signals close to the ZLP. This can be realized by numerical methods which sharpen the ZLP and thereby reduce the extension of the ZLP tail. Richardson[57] and Lucy[58] both proposed an iterative scheme based on Bayes' theorem of conditional probability to restore images and generally sharpen experimental intensity distributions. The so-called Richardson-Lucy (RL) algorithm has been widely used to restore images, e.g., taken by the Hubble space telescope[59-61] or with millimeter waves. Zuo[62] was the first to apply the RL algorithm in the field of electron microscopy, namely high-resolution TEM images, electron diffraction patterns, and EELS spectra. Gloter et al.[63] systematically applied the RL algorithm to improve the energy resolution by a factor of three from 0.9 eV to 0.3 eV for analyzing ionization edges at higher energy losses. Lazar et al.[64] were able to extract signals with energy losses as low as 0.5 eV from the tail of the ZLP from EELS spectra. Recently, Bellido et al.[65] have reported the application of the RL algorithm to SPP resonances along silver nanorods and were able to extract signals as low as 0.25 eV. Rossouw and Botton reported similar SPP resonances at 0.17 eV.[66]

The RL algorithm was implemented with a self-written script in Digital Micrograph (Gatan) according to Al-Bakkar et al.[67] and can be found in appendix A (page 117). The application of the algorithm sharpens the spectral features in EELS spectra by deconvolution with the point-spread function (PSF) of the employed detector system. As this function is not known, a vacuum reference spectrum, taken without the specimen, is used as PSF.

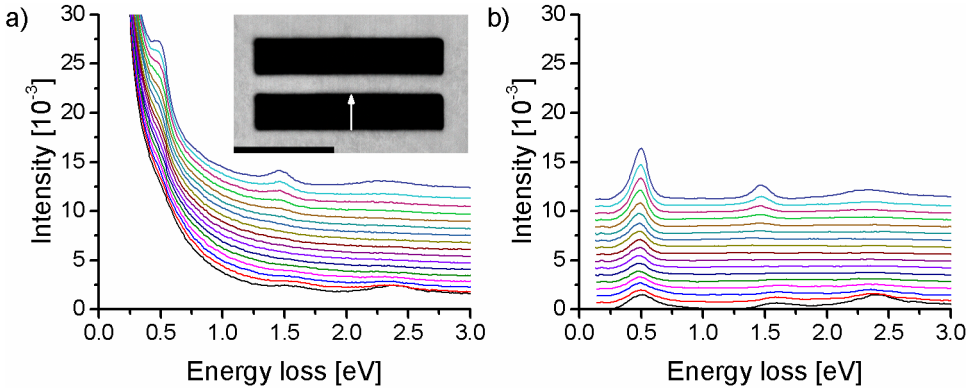

Figure 3.2.1 a) EELS spectra acquired at L/2 in a double-slit system with L = 960 nm and a metal bar width d = 100 nm. The inset shows an HAADF image of the slit system with a white arrow indicating the line along which the spectra were taken. b) The spectra from a) after 7 iterations with the RL algorithm and subsequent background subtraction.

Figure 3.2.1 shows EELS spectra of a transversal scan performed across one slit in a double-slit system with a slit length L = 960 nm. The spectra were acquired along a line at L/2 as indicated by the white arrow in the HAADF STEM image of the double-slit system (inset of Figure 3.2.1a). To illustrate the difficulties encountered when low-energy signals are to be extracted, raw spectra and spectra after processing with the RL algorithm and background subtraction are shown in Figure 3.2.1a,b. Close to the outer wall of the two-slit system, the raw EELS spectrum (black line in Figure 3.2.1a) only shows the Au surface plasmon at E = 2.4 eV and a weak signal at about 1.5 eV. Moving across the slit, another signal at 0.5 eV emerges and the intensity of the 1.5 eV signal increases substantially. The signals at E = 0.5 eV and 1.5 eV are related to the fundamental mode ω_1 and third harmonic ω_3 of cavity standing waves which are excited along the 960 nm slit length. Considering the raw spectra (Figure 3.2.1a), the signal at 0.5 eV is only visible close to the central metal bar and cannot be recognized in the tail of the ZLP close to the outer slit wall. Background fitting with an exponential function does not reliably recover this weak signal. Subtraction of a scaled reference spectrum obtained without specimen can give reasonable results under favorable circumstances if the FWHM of the reference spectrum exactly agrees with the one of the spectrum to be evaluated. Figure 3.2.1b shows the same spectra after seven iterations with the RL algorithm

and subsequent background subtraction with a bi-exponential function which clearly reveal the 0.5 eV signal and its intensity increase towards the central metal bar.

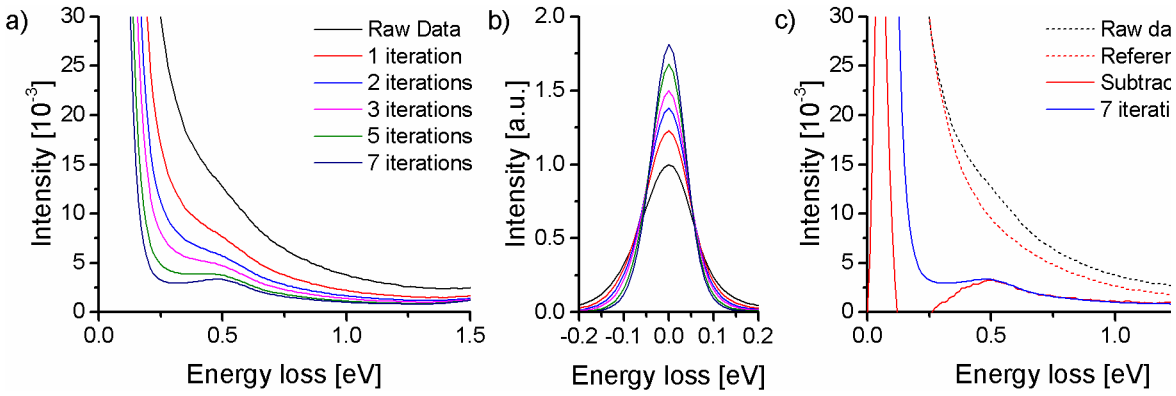

Figure 3.2.2 Effect of sharpening with up to 7 iterations on a) the spectrum acquired at the outer wall (cf. Figure 3.2.1a), b) on the ZLP and c) detailed analysis of the spectra depicted in a). Shown are the raw spectrum (black dashed line), a vacuum reference spectrum (red dashed line), the spectrum after seven iterations with the RL algorithm (solid blue line) and the raw data after reference subtraction (solid red line).

In the following we will focus on testing the performance of the RL algorithm which is essential to extend the detectability of weak low-energy signals and the extraction of quantitative intensity information. Signal processing and iteration numbers n_i with the RL algorithm need to be carefully tested with respect to quantification of the signal intensity. Figure 3.2.2a shows the evolution of a raw spectrum (black line in Figure 3.2.2a) taken at 20 nm distance to the outer slit wall for an increasing number n_i of iterative applications of the RL algorithm. The raw spectrum only shows a weak shoulder at $\Delta E = 0.5$ eV that evolves into a discernible signal already for small n. For more than five iterations, the resolution improvement (observable as a shift of the tail of the ZLP to the left) clearly detaches the ZLP from the SPP signal. Figure 3.2.2b shows the evolution of the ZLP with increasing n_i. The ZLP is sharpened under conservation of the total number of counts which leads to the reduction of the FWHM of the ZLP from typically 0.11 eV to 0.07 eV and a corresponding height increase. For $n_i > 5$ the ZLP becomes edgy due to the sampling with 0.01 eV per channel, which poses a limit to the achievable enhancement of the energy resolution in this case. The influence of the RL algorithm on the spectrum is reduced for increasing energy losses. For $\Delta E > 1.5$ eV these few iterations barely change the spectrum apart from lowering the intensity compared to the raw spectrum. For a small number of iterations, the RL algorithm mainly reduces the FWHM and tail of the ZLP. It is crucial that sharpened data is not again normalized with respect to the ZLP height because the RL algorithm conserves the total number of counts in the spectrum. Normalization with respect to the ZLP height after sharpening would lead to reduced signal intensities in the processed spectrum. Figure 3.2.2c compares spectra after processing with

the RL algorithm (n_i = 7, blue line) and after subtraction of a vacuum reference spectrum (solid red line). Beyond 0.5 eV, the RL-processed spectrum almost coincides with the reference-subtracted spectrum but there are differences at lower energy losses. As the FWHM of the reference spectrum is even slightly broader than the spectrum recorded from the slit structure, a dip in intensity for energy losses below 0.5 eV occurs. Quantification of signal intensity after reference subtraction may give an artificially reduced intensity of the 0.5 eV signal. On the other hand, it is not yet obvious from these considerations whether the correct spectrum is retrieved after seven iterations.

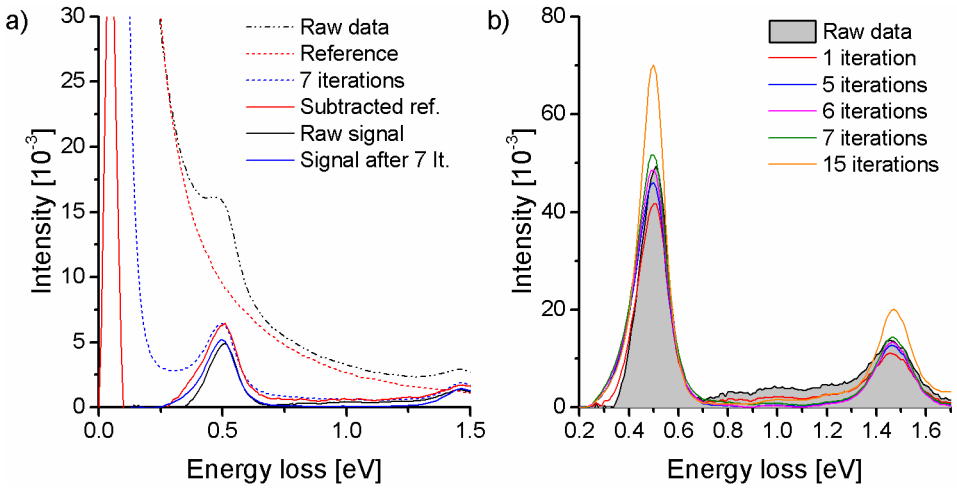

Figure 3.2.3 a) Comparison of different processing methods of a spectrum taken at 10 nm distance from the metal bar (see legend for spectra denotations). b) Background-subtracted spectra after up to 15 iterations of the RL algorithm.

Figure 3.2.3a shows the effect of the RL algorithm on a spectrum acquired at 10 nm distance from the central metal bar of the two-slit system (top-most spectrum in Figure 3.2.1a). Here, the intensity of the 0.5 eV signal is comparatively high in the raw spectrum (black dashed line) which allows to check whether the processed data yields the correct signal intensity. Figure 3.2.3a also contains a reference spectrum (red dashed line) and the raw spectrum after seven iterations of the RL algorithm (blue dashed line). The real intensity is given here by the background-subtracted raw spectrum (solid black line) due to the high signal intensity. This spectrum agrees well with the RL-processed data (solid blue line) after background subtraction. The intensity of the reference-subtracted spectrum (solid red line) is slightly higher. This is related to the FWHM of the ZLP of the reference spectrum slightly differing from the one of the raw spectrum. To investigate the effect of the iteration number with respect to quantification of the signal intensity, up to 15 iterations of the RL algorithm were applied to the raw spectrum in Figure 3.2.3a. Figure 3.2.3b shows the resulting signal intensities at energy losses of about 0.5 eV after background subtraction. The signal for the unsharpened spectrum (raw data) is highlighted (grey filling) for better visibility and comparison with the RL-processed data. Reduced signal intensity is observed

for a small number of iterations ($n_i \leq 3$). The signal intensity increases with n_i and agrees well with the peak intensity of the raw data for $5 \leq n_i \leq 7$. Larger n_i further increase the peak height due to peak sharpening. A small number of iterations only had a strong effect on the ZLP tail (cf. Figure 3.2.2a) which leads to an improved visibility of low-energy signals without altering them significantly. The same observation is made for the third harmonic of the cavity mode (cf. Figure 3.2.3b). Finally, it is noted that the optimum number of iterations may differ depending on the acquisition conditions and has to be individually determined. However, the number of iterations cannot be increased indefinitely as artifacts may be introduced by such a numerical.

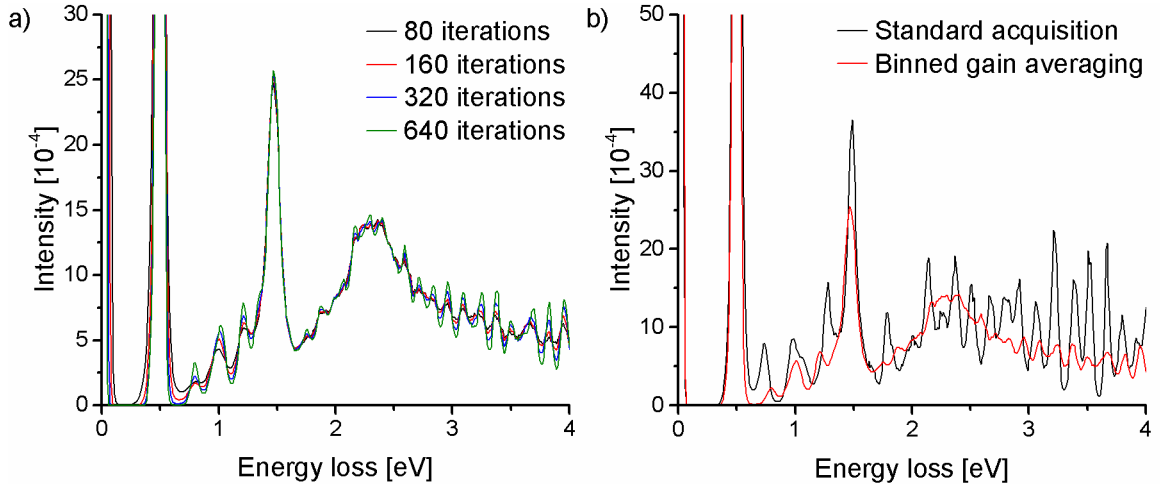

Figure 3.2.4 a) Effect of very large iteration numbers on a spectrum (top-most spectrum of Figure 3.2.1a). b) Noise-amplification suppression by employing binned gain averaging.

Figure 3.2.4a shows how a very large number of iterations (n_i up to 640) detrimentally affects the data. The spectrum used for this test is a spectrum taken close to the metal bar of a double-slit system (top-most spectrum of Figure 3.2.1a). Oscillatory noise with a period of about 0.25 eV is superimposed on the data for nearly the whole spectral range. Only where strong peaks occur in the raw data (i.e. ω_1, ω_3 and the surface plasmon at 2.4 eV), artifacts are not prominently introduced. These artifacts appear because the algorithm mistakes noise as features and sharpens them. The regions in which no physical signals are present are prone to this noise amplification. There, the spectrum and the vacuum reference (which is used as the point-spread function) both consist only of noise and even slight differences between them are interpreted as signals and are amplified. In addition, as the deconvolution translates to a division in Fourier space[67] very low count rates may result in large intensities after numerous iterations.

High iteration numbers are not the only limitation to the application of the algorithm. For an infinite iteration number, the ZLP should be a delta peak function. As stated in the above section, such high iteration numbers are not reasonable due to noise amplification. However, even then, the

ZLP still has a FWHM of several meV. Therefore, a limit exists for the lowest energy that can be analyzed with the RL algorithm.

This low-energy limit strongly depends on the quality of the spectrometer alignment. As an example, spectra from two double-slit systems with L = 2530 and L = 2590 nm are compared in Figure 3.2.5a. The fundamental cavity mode which lies at 0.2 eV is only observed in the double-slit system of L = 2590 nm whereas not even a shoulder appears for L = 2530 nm.

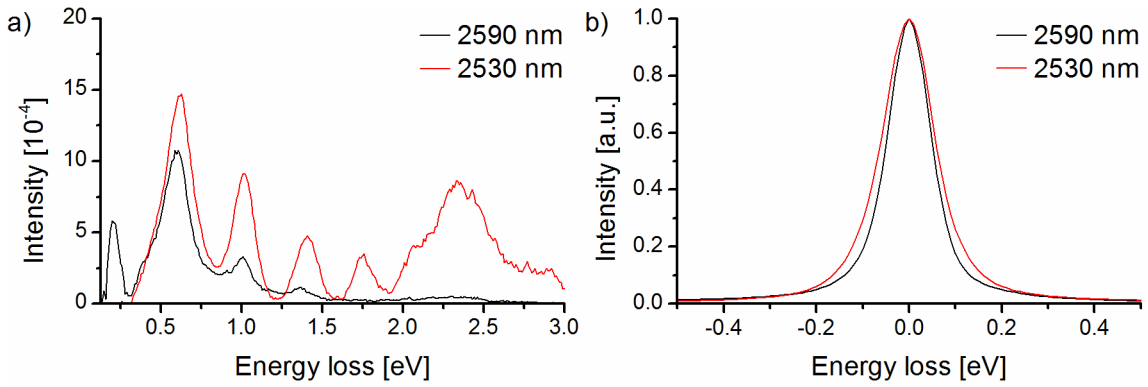

Figure 3.2.5 Comparison of two measurements in double-slit systems with L = 2590 and 2530 nm. a) After full processing with n_i = 7 and bi-exponential background subtraction and b) prior to any processing.

Figure 3.2.5b shows both ZLPs and reveals why the fundamental can only be observed in one of the measurements: The full width at half maximum (FWHM), measured by fitting a Lorentzian peak to the zero-loss peak, is 0.123 eV for the spectra of the slit with L = 2530 nm and 0.101 eV for the slit with L = 2590 nm. Our lowest measured energy of 0.2 eV with the RL algorithm lies at lower energy compared to the values of 0.7 and 0.25 eV reported by Aguiar et al.[68] and Bellido et al.[65]. It is however noted, that with better microscopes, lower energies can be assessed even without sharpening by the RL algorithm. For example, Rossouw and Botton[66] reported the fundamental SPP resonance of a 2070 nm long silver nanowire at 0.17 eV. Cutting edge microscopes push the low-energy limit even lower[56] and allow assessing the energy regime of phonon scattering by EELS[69]. If data obtained from such microscopes would be processed with the RL algorithm, the energy range available to STEM EELS could even be extended down to 10 meV.[65]

3.3 Intensity and Energy Determination

The acquired raw data from the spectrometer, i.e. the individual spectra obtained in a point measurement or in a line scan, is calibrated with respect to the energy axis (i.e. the ZLP peak position). Thereby, energy drift, microscope instabilities and the intentionally superimposed

energy shifts by the binned-gain averaging method are corrected. Single spectra may be removed by hand if their quality is greatly deteriorated by microscope instabilities, e.g. if the ZLP is split and the energy calibration cannot be carried out accurately. After the energy calibration, the individual spectra are summed up. In case of line scans, the spectra from different line scans that correspond to the same spatial position are summed up individually. Then the spectra are normalized with respect to the height of the ZLP, i.e. the intensity of the ZLP in the spectra is unity. In a line scan, this is done for each position of the line scan separately. The same procedure is applied to the recorded vacuum spectra. For each measurement series, numerous vacuum spectra are acquired and the best one is then used for further processing with the RL algorithm. It is essential that the vacuum reference spectrum is as smooth as possible in the energy range of interest between 0.2 and 2.4 eV to avoid the generation of artifacts. For example, a small dip in the vacuum spectrum in this energy range could lead to an artificial peak in the processed spectra.

The next processing step is the application of the RL algorithm. Typically, seven iterations are applied because the processed data is then of comparable intensity to the unsharpened data (cf. Figure 3.2.3b). The processed data is not again normalized as the RL algorithm conserves the total intensity.

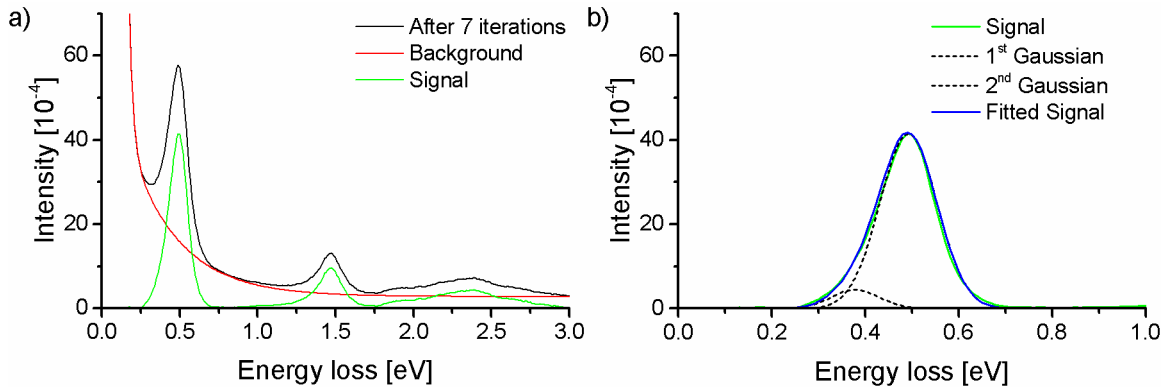

Figure 3.3.1 a) A bi-exponential background (red line) fitted to the processed spectrum (black line) is subtracted to yield the signal (green line). b) The signal from a) is fitted by the sum of two Gaussian functions to determine the energy position and the intensity (area) of ω_1. The spectrum is taken in a double-slit system with L = 960 nm and d = 100 nm at L/2 at 20 nm distance to the inner wall.

Figure 3.3.1 shows the subsequent processing steps. In Figure 3.3.1a, a bi-exponential function (red line) is fitted to the tail of the ZLP of the processed data (black line). The fitting function necessarily consists of two exponential terms because a single exponent cannot reproduce the steep slope of the falling ZLP tail and the slowly decreasing extended tail (for energy losses exceeding 0.5 eV). The bi-exponential function is subtracted from the processed spectrum and yields the signal (green line in Figure 3.3.1a) containing ω_1, ω_3 and the surface plasmon.

The resulting signal is fitted by two Gaussian functions to determine the energy position and the intensity (area) of the ω_1 peak. Two Gaussian functions are necessary because the peak is not symmetrical. The energy position of ω_1 is determined by the center of the large Gaussian function whereas the intensity is determined by the sum of the two Gaussian functions.

The energy position can be measured with an accuracy of 2 meV by the Gaussian fit. The energy calibration was performed with respect to the position of the ZLP given by the pixel with maximum intensity. The error of this calibration is at best the dispersion of the spectrometer which is 10 meV per channel and therefore the error in energy in all measurements is assumed as 10 meV. Acquiring the spectra with a higher dispersion may reduce this error; however, 10 meV is the highest available dispersion of the employed spectrometer.

The error in the intensity (area) is difficult to access. The two Gaussian functions can fit the peak area with very high accuracy. The Gaussian fit is able reproduce the experimental data with a high accuracy of about $0.2 \cdot 10^{-4}$ which is determined by the difference between the summed area of the Gaussian function and the integrated intensity of the peak. However, the true error will be definitely larger because the derivation of the fitted signal is also subject to errors. These errors are difficult to estimate but are however assumed to be in the range of $0.5 \cdot 10^{-4}$. This error can be easily visualized in this particular case as this is roughly the area of the small Gaussian function. The area of this small Gaussian seems to be far larger as the peak height is about $5 \cdot 10^{-4}$. However, the FWHM of the peak is only ~0.12 eV and therefore the resulting peak area is in the range of $0.5 \cdot 10^{-4}$.

3.4 Numerical Simulations

The simulations presented in this work were performed by C. Mattysek in the group of K. Busch (Humboldt University, Berlin). Numerical simulations are carried out using the Discontinuous Galerkin Time Domain (DGTD) method[44, 70, 71] with the extensions that are necessary to perform EELS simulations.[70] The only difference is that a pure scattered field formalism was applied, which gives direct access to the field induced by the electron. The permittivity of the gold film is approximated by a single Drude and three Lorentz terms, which gives a reasonable approximation to the data measured by Johnson and Christy[72] over the entire energy range.

The gold film is finite with a size of at least 3x3 μm^2 to reduce artifacts from the edges. Except for a small feature around 0.4 eV, which, however, is well below the fundamental resonance (in the case for slits with L = 960 nm for which the simulations are performed), the spectrum is entirely free of artifacts. The film is surrounded by air and perfectly matched layers to reduce reflections from the boundary of the computational domain. Third-order elements are used with element sizes down to 10 nm to accurately resolve the incident field of the electron. The simulated spectra are

convoluted with a Gaussian function of 100 meV full width at half maximum, accounting for the finite experimental energy resolution and the corresponding spectral broadening.

3.5 Sample Preparation

3.5.1 Au Film Preparation

The Au films were prepared by evaporation of 200 nm Au onto mica substrates by physical vapor deposition in a Lesker PVD 75 (Kurt J. Lesker company, Jefferson Hills, Pennsylvania, USA). The prepared films were subsequently floated off onto TEM grids. The Au film adheres strongly to the mica surface and thus floating off was hampered. To facilitate the floating-off process, the mica substrates are treated with tensides prior to the Au deposition. The 200 nm thick films only weakly adhere to the TEM grids and have to be treated with care as the film easily detaches from the grid. The weak adhesion could probably stem from internal stress which leads to wrinkling of the film. Consequently, the area of support is reduced compared to a flat film and hence the film could easily detach from the grid even by careful handling of the specimen. Especially the vacuum tweezers used to insert the specimen into the TEM holder are problematic and destroyed various specimens. To ease handling of the specimens and circumvent their destruction during mounting in the TEM holder, folding grids were employed to hold the 200 nm thick films firmly in place.

3.5.2 Nanostructure milling

The various slit systems, i.e. single slits, double-slit systems with varying slit length L and inter-slit distance d and slit arrays consisting of up to 60 slits, that were examined in this work, were prepared by focused ion beam (FIB) milling in an FEI Dual Beam STRATA 400S. Ga^+-ions with energy of 30 keV are used. As the nominal pattern sizes entered in the FIB software were not equal to the actual size of the milled nanostructures, a series of test cuts had to be performed to determine the optimal parameters to ensure the milled nanostructures have the correct desired sizes. In addition, specimen drift in the FIB system during the nanostructure milling can lead to imperfect shapes of the slits, especially of the slit corners. Therefore, the milling time was reduced to the minimum value while still achieving complete perforation of the metal film. However, this can introduce artifacts in the form of small bumps protruding into the slit. The cutting speed is also affected by the orientation of the grains in the Au film. If a grain, that takes longer to cut through, is located in the slit, such bumps may occur. Additional artifacts related to the varying cutting speed with respect to local variation of the film morphology are bent or destroyed metal bars which separate the slits. Metal bars between slits which were milled faster than the surrounding slits bend during milling. Depending on the extent of the bending, the metal bars can be milled

away as well which proved especially difficult in the case of larger arrays due to the increased number of metal bars.

4 Nanostructured Slits in a Au Film

4.1 Previous Work

Since the discovery of extraordinary optical transmission (EOT) through periodic sub-wavelength slit arrays in a thin metal film by Ebbesen et al.,[8] a lot of studies[73-75] have reproduced the effect and focused on investigating the physical processes responsible for EOT. According to Bethe's theory of transmission through small apertures in a metal film,[76] the transmission drops with $(r/\lambda)^4$ and hence for a sub-wavelength aperture ($r << \lambda$), the net transmission rapidly approaches zero. The results of Ebbesen et al.,[8] however, show significant transmission. An intuitive picture to describe the effect is to relate the transmission to the hole area: the transmission through the array of sub-wavelength slits is higher compared to the transmission through a single, large aperture whose size is identical to the summed area of the small holes. Normalized to the hole area, the transmission coefficient may even exceed unity.

The enhanced transmission is related to SPPs generated on the film surface.[1, 77-80] Light cannot directly couple to SPPs as their dispersion relation always lies below the light line (cf. Figure 2.1.1). The periodicity of an array in a metal film, however, leads to a lattice momentum **G** that can mediate coupling to the SPPs by momentum matching of $\mathbf{k}_{SPP} = \mathbf{k}_{Photon} + \mathbf{G}$. **G** is the reciprocal lattice vector given by $\mathbf{G} = 2\pi/a$ with the lattice period a. The SPPs generated at the film surface are able to excite SPPs in the apertures which in turn can generate SPPs at the other film surface. These SPP can emit light by the above-mentioned momentum matching condition. The re-emission of light by SPPs causes the EOT phenomenon. Because EOT is mediated by SPPs excited in the individual apertures in the array, the exact shape of these apertures has a strong influence on SPP generation.[81] SPPs can also be excited at discontinuities on the film surface, i.e. for diffraction at the nanoapertures themselves[10, 82] and therefore even single apertures can exhibit EOT.[83-85]

However, the majority of studies on EOT focuses on the transmission efficiency as a whole and therefore cannot distinguish the three main processes involved in EOT. These are the excitation of SPPs on the film surface, the generation and propagation of SPPs in the nanoapertures and the re-emission of light on the other film surface. Especially the interaction of SPPs in the apertures comprising the array cannot be separately studied if only the transmission as a whole is investigated. STEM EELS is therefore a predestined experimental method to probe SPPs in the nanoapertures. The high spatial resolution enables the excitation of SPPs in single holes which poses an advantage to light-optical methods which illuminate numerous nanoapertures at once. The focused electron beam can couple to both far-field and near-field components[28, 86] of the electromagnetic field and thus is able to efficiently probe the SPP characteristics in a nanoaperture.

The electron beam is positioned inside the slit to eliminate direct scattering processes with the metal film. SPPs are then excited by the electromagnetic field of the passing electron. The induced electromagnetic field of the SPP acts back on the electron and causes it to lose energy.

In the following section, several studies that focus on SPPs in nanoapertures and their interaction will be discussed in detail. Alaverdyan et al.[87] have studied nanohole chains milled in a 20 nm thin Au film on a SiO_2 substrate by inverted dark-field microscopy. The specimen was illuminated by white light from a 100 W source with an angle of incidence larger than the collection angle of the microscope objective. This ensures that only light scattered by the specimen will be collected by the spectrometer attached to the microscope. In addition, a polarizer/slit system allows performing measurements with varying polarization and direction of illumination (i.e. the incident wave vector k). As proof of principle, they measured two perpendicular chains of nanoholes with different orientation of k. Only if the k was perpendicular to a nanohole chain, it gave a strong spectral response whereas the other chain did not. The case of k perpendicular to the nanohole chain corresponds to the situation where all holes are excited in phase.

They have investigated chains of two nanoholes (diameter of 70 nm) with varying nanohole separation (d = 30 to 390 nm). The illuminating wave vector k was perpendicular to the chain. Significant spectral variation was observed if the incident polarization was parallel to the nanohole chain whereas in the case of perpendicular polarization only minor effects occurred. For small inter-hole distances, the resonance peak was blue-shifted compared to an isolated nanohole. An increase in the hole separation lead to a gradual red-shift and intensity enhancement, which reached a factor of ten for d = 150 nm. The red-shift persisted for further increasing the separation although the intensity decreased until the peak almost vanished for d = 300 nm. In addition, for d > 240 nm, a second peak emerged at higher energy. This second peak was also shifted to the red for further increasing hole separation. A nanohole chain consisting of 8 holes showed similar spectral behavior although shifted by about 30 nm to the blue. They attributed this spectral shift to a difference in the nanohole diameter that results in a shifted resonance peak.

They were able to reproduce their experimental findings by coupled-charge simulations. The resonance of a single hole is a localized surface plasmon of dipole character. The incident optic field induces a dipole moment along the polarization of the incident field. In the case of small distances d between nanoholes, the interaction of the holes is governed by electrostatically coupled dipoles. Depending on the polarization in reference to the axis connecting the dipoles, two resonance frequencies that are shifted from the single hole resonance emerge. In their experiments, strong spectral shifts compared to the single hole emerged for chains of two nanoholes.

However for increasing distances between holes, the role of the electrostatic coupling diminishes and the coupling between holes will be governed by SPP waves propagating between the holes (at least in the case of a metal film). As the emission of SPPs is preferentially along the direction of

the induced dipole moment,[88] the spectral effects of the SPP-mediated coupling are only significant if the nanohole chain is illuminated with a polarization parallel to the chain axis. If the nanohole separation is a half-integral multiple of the SPP wavelength, the charges induced by the illuminating light and the oscillating SPPs will interfere constructively and lead to an increase of the scattering intensity. However if the nanohole separation is an integer multiple of the SPP wavelength, the interference is destructive and the scattering intensity decreases.

The dependence of the peak intensity (normalized per hole) on the number of nanoholes was also investigated. The hole separation was set to d = 150 nm and the polarization was parallel to the chain as this gave the strongest enhancement. In case of in-phase illumination (k perpendicular to the chain), a strong effect of the increasing number of holes on the intensity enhancement was observed whereas the intensity decreased for out of phase illumination. The strongest enhancement was observed for a chain of three nanoholes. However, the intensity reached a plateau of equal intensity for five and eighteen slits which was slightly lower compared to the three-hole system and may indicate the influence of edge effects.

Ögüt et al.[89] studied a single slit of size 1107 nm x 210 nm in a sub-electron sub-angstrom microscope[90] (SESAM, Zeiss, Oberkochen, Germany) operated at 200 keV and equipped with a Omega-type electrostatic monochromator and an in-column MANDOLINE[55] filter. The obtained EFTEM series showed intensity distributions of Fabry-Perot-like standing waves at energies of 1.0, 1.4, and 1.8 eV. These energies correspond to the orders n = 2, 3, and 4 of a standing wave in the slit. They could not resolve the fundamental mode as it is too close to the ZLP and thus cannot be distinguished from it. Simulations performed with by the finite element method (FEM) also show matching cavity modes although at lower energies, i.e. 1.0, 1.19 and 1.62 eV. Additionally, the simulation revealed weaker signals at energies of 1.25, 1.58 and 1.88 eV that also correspond to the mode orders two to four. They explained the emergence of symmetric and anti-symmetric modes for the different Fabry-Perot-like standing waves by an energy-level scheme. A single wall (i.e. a slit with infinite width) supports a standing wave. If the slit width is reduced to such an extent that the standing waves on both slit walls interact, hybridization of both standing waves occurs. A ‘binding’ (anti-symmetric) mode with reduced energy results from opposite charges on the two slit walls and a strong electric field in the slit, whereas an ‘anti-binding’ (symmetric) mode with higher energy consists of same charges on either slit wall and a weak electric field in the slit. Moreover, even with a high experimental energy resolution of 0.2 eV, the symmetric and anti-symmetric modes are difficult to distinguish.

They also studied a double-slit system consisting of slits of size 180 x 1070 nm separated by a metal bar 130 nm in width. They were able to observe Fabry-Perot-like standing waves along the long slit walls, similar to the single slit. Simulations performed for this slit structure showed two energies and field distributions for each one of the mode orders n = 2-4. Both slits in the double

slit had opposite charges on both slit walls and therefore correspond to the anti-symmetric, lower-energy mode of the single slit. The corresponding symmetric mode did not occur in the double slit simulation. However, the anti-symmetric mode of the single slit hybridized in the double slit. Two modes emerged depending on the charge and electric field distribution in the slits. The low-energy mode had equal charges on the metal bar separating the slits and hence resulted in anti-symmetric electric fields in both slits. The higher-energy mode on the other hand had odd charges on the metal bar resulting in symmetric electric fields in both slits. They explained these observations in the simulation with another energy-level scheme for the cases of a single wall, two walls (i.e. single slit) and four walls (i.e. a double slit). The SPPs supported on the single wall hybridizes into an anti-symmetric, denoted α, and a symmetric, denoted α', mode in the case of the single slit. In a double slit, four walls may interact and hence four modes should be observed. The simulations however showed that only the anti-symmetric α mode splits into two modes in the double slit, denoted by α* and α**. The α* mode is shifted to lower energy and corresponds to anti-symmetric electric fields in both slits. The α** mode is shifted towards higher energy and corresponds to symmetric electric fields in both slits.

Carmeli et al.[14] studied single slits milled in a thin Au film of 200 nm thickness by STEM EELS in an FEI Titan (Hillsboro, Oregon, USA) operated at 300 keV and equipped with an electron monochromator. The investigated slits all had a length of 4500 nm and widths of 600, 900, and 1200 nm. Measurements were performed starting at the center of the slits and step-wise approach of the short slit side. At small distances to the slit walls, they were able to resolve low-energy peaks corresponding to standing waves at the short slit sides. The fundamental modes had energies of 0.5, 0.65, and 1.0 eV for the slit widths of 1200, 900, and 600 nm. In addition to the fundamental modes they also were able to resolve higher energy multiples corresponding to higher order modes of the standing waves. The measurements in the slit of 1200 nm width can be compared to the measurements of Ögüt et al.[89] as their slit was of similar size. Interestingly, Carmeli et al.[14] reported an energy of 1.5 eV for the third harmonic whereas Ögüt et al.[89] measured 1.4 eV. However, keeping in mind the large slit length of 4500 nm, this energy difference can be readily explained by the energy-level scheme. With such a large distance between the slit walls, no interaction amongst them is feasible and hence Carmeli et al.[14] examined the case of a single wall with unperturbed energy. They also compared two single slits with 900 nm length and widths of 180 and 4500 nm. The excitation position was fixed near the 900 nm long slit wall. The fundamental energy of the narrow slit was 0.5 eV in contrast to 0.65 eV for the wide slit. This observation supports the above-mentioned assumption that the lower than expected energy in case of the narrow slits stems from the interaction of SPPs on both slit walls.

Prangsma et al.[91] studied rectangular holes in a 200 nm thin Au film on a Si substrate via scanning electron microscopy in conjunction with a catholuminescence detector. The light generated in the

specimen by the electron beam excitation is collected with a parabolic mirror above the specimen. A small hole in the mirror allows the electron beam to reach the specimen. The collected light is coupled to a spectrometer which allows acquiring a spectrum at each scanning position of the electron beam. They investigated a single hole 100 x 260 nm in size and observed signals close to all four walls of the slit. The peak at the short slit wall was weaker compared to the peak at the long slit wall. Both peaks also varied spectrally. The spectrum obtained near the short wall peaked at a wavelength of 560 nm whereas the long wall showed a peak at 680 nm. The latter one is related to the fundamental cavity mode of the 260 nm long slit. They further studied single holes with a wide variety of sizes ranging from 100 to 500 nm in both directions. An increase in slit length resulted in a red-shift of the peak measured close to the long slit wall. The observed wavelengths were always larger than the expected nominal wavelength for a resonant cavity of identical sizes. Interestingly, however, the wavelength of the fundamental cavity mode also shifted depending on the slit width. The narrower a slit was, the stronger the fundamental cavity mode shifted to the red. This is related to the hybridization of the SPPs on both slit walls, similar to the line of argumentation for the different slit sizes measured by Carmeli et al.[14] For increasing slit width, the interaction of both walls diminishes and hence the hybridization in symmetric and anti-symmetric modes (cf. Ögüt et al.[89]) is weaker.

In addition to the various single holes, Prangsma et al.[91] investigated arrays consisting of three slits with varying inter-slit distance. The slits were 100 x 260 nm in size and the inter-slit distances were fixed at d = 240, 300, and 350 nm. For each structure, spectra were acquired near both walls of one of the outer slits and near one wall of the central slit. In summary, half of the array was analyzed. For all measurement positions, the wavelength of the fundamental peak shifted to the red for increasing the inter-slit distance. The average wavelengths obtained were 610, 635, and 665 nm or increasing the inter-slit distance from 240 to 350 nm. Compared to the single slit measurement of the same slit size, the peaks for all inter-slit distances are blue-shifted (and thereby may correspond to the α^{**} mode Ögüt et al.[89] have found in a double-slit system). This could be related to the coupling between the individual slits inside the array in dependence on the slit separation. Intensity variations were also observed inside the array system and were independent on the particular inter-slit distance. The intensity near the outer wall of the first slit was weak and consecutively rose near the inner wall of the first slit and the next wall in the central slit.

4.2 Hybridized Surface Plasmon Polariton Cavity Modes in a Single Slit

4.2.1 Experimental Results

A single slit constitutes the basic structure for the various nanostructures that were analyzed within this work. As such it is of great importance to examine and describe its behavior prior to any additional measurements. Figure 4.2.1 shows a single slit with a size of 980 nm x 200 nm. Measurements were performed by starting at the center of the slit with respect to the long slit axis and approaching the long slit wall in steps of 10 nm (cf. white arrow in Figure 4.2.1).

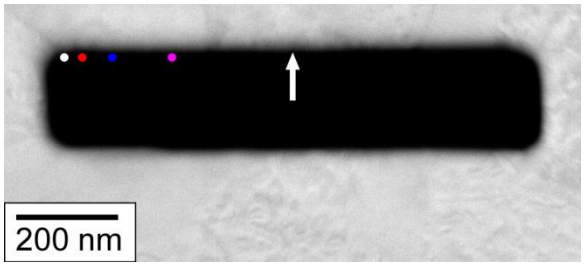

Figure 4.2.1 HAADF STEM image of a 980 nm x 200 nm slit. The white arrow and the colored dots mark the measurement positions of the spectra shown in Figures 4.2.2 and 4.2.3.

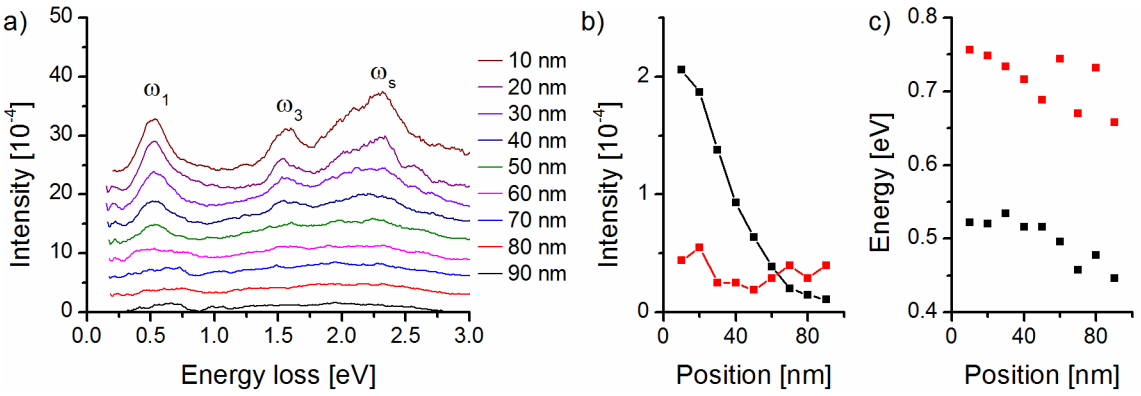

Figure 4.2.2 a) EELS spectra taken along the white arrow in Figure 4.2.1, b) and c) corresponding integrated intensity and peak energies of the cavity mode as a function of the distance to the slit wall. The data with red symbols denotes the fundamental mode, the black symbols the high-energy shoulder of the fundamental mode.

The corresponding EELS measurements are shown in Figure 4.2.2a. For the measurement in the center of the slit (black line), specific signals are barely observed. Upon approaching the slit wall, distinct signals at ~ 0.5, ~ 1.6, and ~ 2.4 eV emerge. The first two signals correspond to the fundamental mode, denoted by ω_1, and third harmonic ω_3 of a cavity mode extending along the long slit axis. The signal at 2.4 eV can be assigned to the surface plasmon energy of the Au film,[15] denoted by ω_S. The measured energy of ω_S is slightly lower compared to the reported 2.48 eV, however, Schlüter[15] has reported a value of 2.37 eV for a thin carbon contamination of 5 nm on the Au film. The intensity of the fundamental mode decreases with increasing distance to the slit wall and shows peak broadening. Especially for the larger distances, a small shoulder appears at the high-energy side. The integrated intensities and peak energies of the fundamental mode and its shoulder are plotted depending on the distance to the slit wall in Figure 4.2.2b and c. The data was extracted by fitting two Gaussian peaks to the spectra. The intensity of the fundamental mode decays nearly exponentially whereas the small shoulder barely shows any intensity variation. Additionally to the enhancement, spectral shifts are observed. The fundamental energy is 0.52 eV close the wall and shifts slightly towards lower energies near the slit center. The small shoulder shows a similar behavior although with a higher energy of 0.76 eV at the wall. The third harmonic shows an energy shift as well, albeit less significant compared to the fundamental. Its first measurable energy is 1.54 eV at 40 nm distance to the slit wall. Close to the slit walls, a slight blue-shift to 1.58 eV is observed. The surface plasmon is also first observed at 40 nm distance in the shape of a very broad peak roughly centered at 2.2 eV. At 10 and 20 nm distance it is enhanced asymmetrically with the maximum located at 2.32 eV.

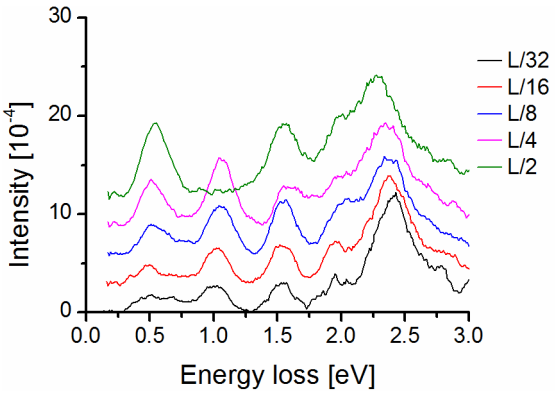

Figure 4.2.3 EELS spectra taken close to the slit wall at the positions marked by colored dots in Figure 4.2.1.

In addition to the transversal scan, spectra were taken at 10 nm distance to the slit wall along the long slit axis as shown by the colored dots in Figure 4.2.1. The measurement positions were taken at specific slit length ratios to compare the results with the expected Fabry-Perot-like behavior of the cavity modes. The resulting spectra are shown in Figure 4.2.3. As the measurements were

taken close to the slit wall, the Au surface plasmon is observed in all spectra with high intensity. When the electron beam is positioned exactly at the center of the long axis (green line), only odd modes with n = 1 and 3 are observed in the spectrum at 0.54 and ~ 1.55 eV. Even modes have nodes at this position and do not appear in the spectrum. When the position is shifted to a fourth of the slit length (L/4), the first even mode with n = 2 at 1.06 eV is observed as well as the n = 1 and 3 modes albeit the latter ones show reduced intensity as the measurement position at L/4 does not exactly coincide with the respective antinode positions of these modes. At L/8, the second even mode of order n = 4 is clearly observed in the spectrum at 2.0 eV. For the two smallest distances to the short slit wall, the modes with n = 1 to 4 are all observed in the spectra with nearly identical intensities. The only exception is the fundamental whose intensity is increasingly reduced close the slit wall. Interestingly, the fourth harmonic is - albeit weakly - observable even in the spectra recorded at L/2 and L/4 where it should have zero intensity as these positions coincide with the nodes of this mode.

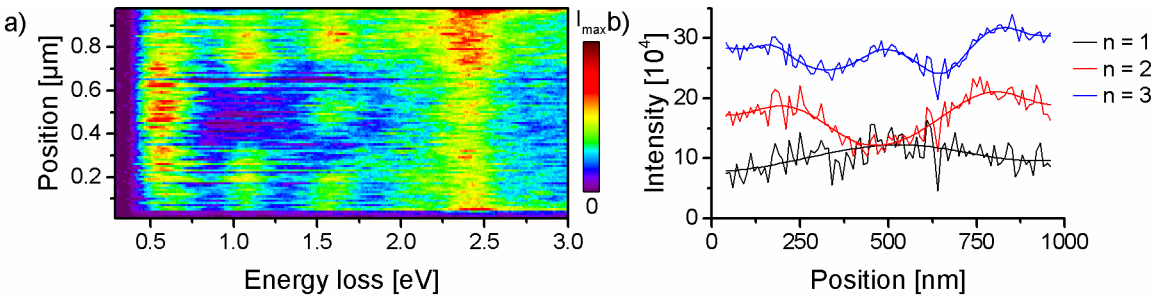

Figure 4.2.4 a) Color-coded EELS intensities along a line scan at 10 nm distance to the long wall in a single slit and b) resulting intensity profiles of the cavity modes of orders 1 to 3 (raw and FFT-smoothed data).

In addition to the measurements at specific points inside the single slit, a line scan was performed at 10 nm distance to the slit wall. The resulting color-coded intensity is presented as a function of energy loss and position in a 2D color map in Figure 4.2.4a. It shows the expected Fabry-Perot-like behavior, i.e., the number of maxima in the color map per mode order is equal to the mode order. Intensity profiles were extracted from this line scan to analyze the mode distributions in the nanostructured slit (Figure 4.2.4b). The profiles were extracted at the respective energies of the modes of orders 1 to 3 with an energy window of 100 meV (equal to a ten pixel integration window) in order to improve the signal-to-noise ratio in the data. Additionally, the resulting profiles were smoothed by a FFT fit. The distances between maxima in the intensity plots shown in Figure 4.2.4b allow the calculation of the wavelengths of the respective modes. The wavelengths were determined by measuring the distance between two adjacent intensity extremes. The resulting wavelengths are compared to the nominal wavelengths given by equation (2.30) in

Table 4.2.1. The wavelength of the fundamental mode cannot not be measured because is exhibits only one maximum.

n	λ_{exp}	λ_{nom}	Deviation of λ_{exp}
1	-	1960 nm	-
2	1250 nm	980 nm	+ 27.6 %
3	715 nm	653 nm	+ 9.5 %

Table 4.2.1 Wavelengths of the cavity modes inside a single slit of size 980 x 200 nm.

The measured wavelengths are larger than the nominal ones. The deviation decreases with increasing mode order.

4.2.2 Discussion

The wavelength and energy of the cavity modes is dictated by equations (2.30) and (2.31). For a slit length of L = 980 nm, the fundamental mode ω_1 should have a wavelength of 1960 nm which corresponds to the energy of E_1 = 0.65 eV. However, the energy of the fundamental mode in the experiments is only 0.52 eV and, additionally, there is a weak shoulder observed at 0.76 eV as shown in Figure 4.2.2a. These two peaks correspond directly to the two possible excitations of a single slit proposed by Ögüt et al.[89] due to the hybridization of SPPs supported by the two long slit walls. The hybridization leads to a symmetric (S) and anti-symmetric (AS) mode with blue- and red-shifted energy. The existence of the blue-shifted mode was only revealed in numerical simulations and could not be resolved in their measurements due to its low intensity.

With STEM EELS the AS and weak S modes could be detected. For measurements close to the slit walls we can confirm the differences in intensity that Ögüt et al.[89] were able to derive in their simulations. In the center of the slit, however, both modes have similar intensity as shown in Figure 4.2.2b. Only one of the modes is enhanced in the near-field region close to the slit wall due to hybridization with SPPs on the walls.[14] This could be related to the different electric field distributions for the two modes.[89] In case of the AS mode, the electric fields of the SPPS on opposite slit walls are of different sign and, hence, the net electric field along the transversal direction of the slit is strong. For the S mode on the other hand, the electric fields of the SPPs are of identical sign on opposite slit walls and do not yield a strong net electric field inside the slit. As the cavity modes interact strongly with SPPs on the slit walls,[14] the differences in intensity of both modes may be related to such an effect.

Both modes shift to lower energy for increasing distance to the slit wall and, at the center of the slit, they occur at 0.45 and 0.66 eV. The S mode has shifted to the expected nominal energy of 0.65 eV in the single slit. The splitting of the modes is attributed to the interaction of both slit walls. Following the above argumentation for the intensity enhancement of both modes in relation to the net electric field inside the slit, the shifts in energy may be related to the same effect. The repelling electric fields in case of the S mode may lead to a damped interaction of both slit walls and hence result in the occurrence of the unperturbed, nominal energy of the resonant cavity.

According this line of argumentation, there should also be a significant intensity difference between both modes in the center of the slit which is not observed in the experiments. A possible explanation may be that the enhancement observed in the near-field region[14] is somehow dependent on the net electric field and is therefore only present in the case of the antisymmetric mode. In addition, the question arises whether the excitation by STEM EELS or by EFTEM will result in similar field strengths. This cannot be certified, but it would be surprising if these differences in strength are depending on the particular excited mode. If they are one the other hand a mere offset factor, the relative strengths in fields will not differ and the line of argumentation in the previous paragraph will hold.

The point measurements at different positions corresponding to various ratios of the slit length L (Figure 4.2.3) show Fabry-Perot-like behavior expected for a resonant cavity. Similar Fabry-Perot-like standing SPP waves were also detected in nanorods[66, 92-94], coupled nanorods[95] and other nanostructures with high aspect ratio.[96, 97] The higher harmonics are only strongly observed in the spectra if the measurement position coincides with an antinode of the respective mode order. However, there are small spectral variations along the longitudinal scan. Approaching the short slit wall, all harmonics experience a slight red-shift (cf. Figure 4.2.3 and Figure 4.2.4). In case of the fundamental mode and the second harmonic, the red-shifts are barely discernible in Figure 4.2.4 but can be extracted from the spectra of Figure 4.2.3. A red-shift corresponds to an enlargement in wavelength and therefore indicates that the SPPs intrude into the metal film. The red-shift increases with decreasing distance to the short slit wall, i.e. the wavelength elongation is largest close to these walls. Additionally, the data from the line scan shows increasing deviations from the nominal wavelength with decreasing mode order (Table 4.2.1). This indicates that only the antinodes closest to the slit walls are affected. In case of the second harmonic, only two antinodes are observed and used for the experimental determination of the wavelength. It should therefore experience the largest deviation. It is instructive to evaluate the profile of the third harmonic in detail. If node and antinode positions are extracted, more data points for wavelength measurements are available as the distances between a node and the adjacent antinode is $\lambda/4$. The extracted $\lambda/4$ values correspond to wavelengths of 824, 656, 564, and 856 nm (compared to λ_{nom}= 653 nm), demonstrating that the wavelength is larger close to the short slit walls than in the center of the slit.

Prangsma et al. also have observed a wavelength elongation in single slits in a 200 nm thick Au film. The slit they analyzed was of size 100 x 260 nm which results in an expected wavelength of 520 nm for the fundamental cavity mode of the long slit wall. However in their measurements they have found the signal of the fundamental cavity mode at wavelength of ~ 680 nm, corresponding to a wavelength elongation of 31%.

Wavelength variation was also reported for SPP modes of metal nanowires.[92, 93] According to Babinet's principle, a slit in a thin metal film and a metal nanowire are complementary and therefore show complementary behavior. The electric and magnetic fields in the systems are interchanged which leads to a phase shift of $\pi/2$ between nanowires and slits. The phase-shift between the electric and magnetic fields in the resonant cavity is a result of the different boundary conditions of these fields at the film surface.[13] Therefore the fundamental mode of the nanowire has two intensity maxima at the edges of the wire whereas the fundamental mode in a slit only has one intensity maximum in the center of the slit. Interestingly, the wavelength variation of the nanowires is also complementary to the slits as the wavelength is decreasing near the edges of the nanowire. Also this wavelength variation is strongest for the lower order modes and is decreasing with increasing mode order.

4.3 Tuning of Hybridized Surface Plasmon Polariton Cavity Modes

4.3.1 Experimental Results

Nanostructured slits with varying slit length L were prepared in order to analyze the effect of different slit lengths on the SPP cavity modes. The intensities of the cavity modes are weak in a single slit and, therefore, double-slit systems were prepared. Coupling to a neighboring slit significantly enhances the intensity close to the metal bar separating the two slits. This enhancement will be described in detail in Chapter 4.4 (page 50).

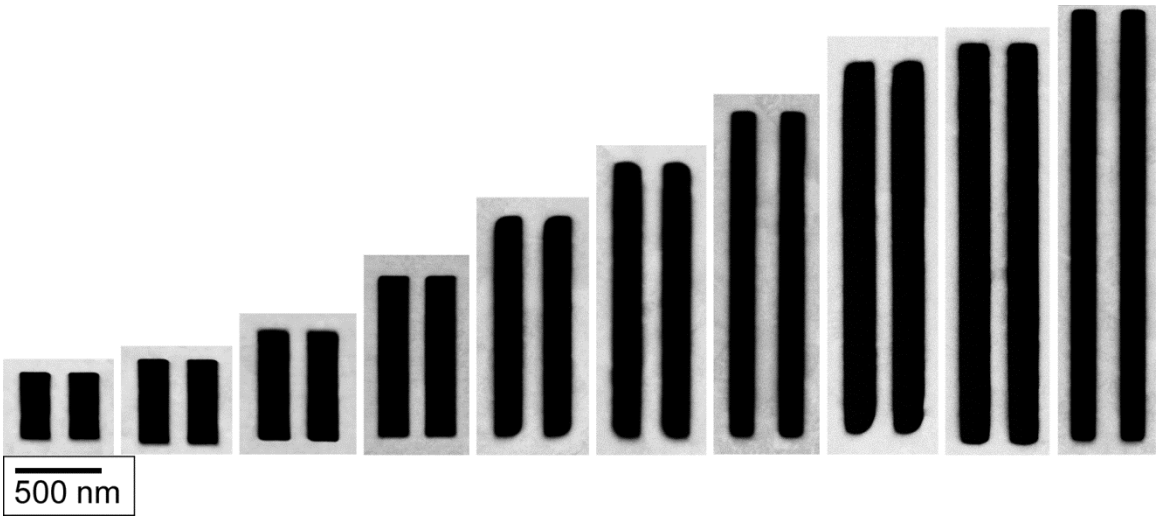

Figure 4.3.1 HAADF STEM images of the analyzed double-slit systems with varying lengths L of 400, 530, 645, 960, 1300, 1620, 1900, 2180, 2340, and 2530 nm (from left to right) and a common metal bar width of d = 100 nm.

Figure 4.3.1 shows HAADF STEM images of all prepared double-slit systems with different slit lengths L of 400, 530, 645, 960, 1300, 1620, 1900, 2180, 2340, and 2530 nm. The distance between slits is determined by the width of the central metal bar d between the slits. All shown slit systems have d = 100 nm.

Similar to the single slit, EELS measurements were performed in all of the double-slit systems. The beam was positioned in the center of the slit (with respect to the long slit direction) at 10 nm distance to the central bar separating the two slits. The resulting spectra are shown in Figure 4.3.2. The top spectrum was acquired in the shortest slit (L = 400 nm). The slit length increases for the spectra shown below with the bottom spectrum taken in the double-slit system with L = 2530 nm. A steady red-shift from 1.05 eV (L = 400 nm) to 0.24 eV (L = 2530 nm) of the fundamental mode is observed for increasing slit lengths L. In addition, the number of observable higher order cavity

modes increases. For example, only the fundamental and the Au surface plasmon is observed for L = 400 nm, whereas even the eleventh harmonic is detectable in the double-slit system with L = 2520 nm. Only odd harmonics are observed for symmetry reasons. The higher harmonics also shift to lower energies with increasing slit length, similar to the fundamental mode. Due to suboptimal measurement conditions, some of the shown spectra were treated with more than the standard seven iterations of the RL algorithm. This concerns the spectra from double-slit systems with L = 1620 nm (15 iterations), L = 1900 nm and L = 2530 nm (both 20 iterations). It is noted, that even after 20 iterations, the fundamental mode in the longest double-slit system could not be resolved in this measurement series.

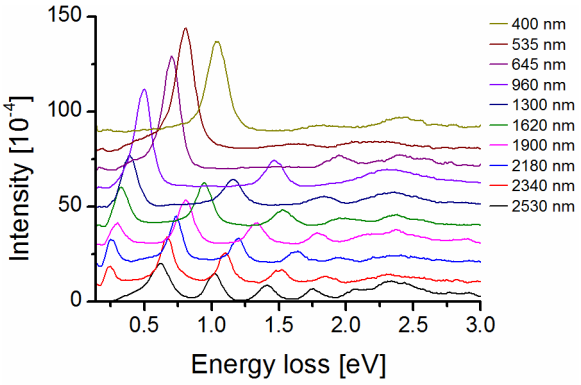

Figure 4.3.2 Spectra acquired at 10 nm distance to the central metal bar in double-slit systems with varying slit length L. Spectra are vertically shifted.

The double-slit system with L = 2340 nm is analyzed in more detail in Figure 4.3.3. This slit length was chosen because the double-slit system with L = 2530 nm is challenging to examine. This is due to the small energy of the fundamental which could only be resolved if all alignments are perfect, which was discussed in chapter 3.2 (page 18). The corresponding black spectrum in Figure 4.3.2 for example does not show the fundamental mode. The measurement positions were chosen to be ratios of the slit length, similar to the measurements presented in Figure 4.2.3 for a single slit.

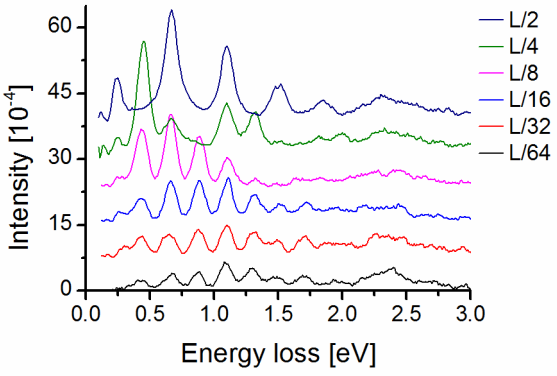

Figure 4.3.3 Spectra taken at specific positions corresponding to ratios of the slit length L = 2340 nm at 10 nm distance to the metal bar.

The spectrum taken at the center of the slit (L/2) only shows odd modes for symmetry reasons. The first five odd modes, i.e. n = 1, 3, 5, 7, and 9 are observed. The eleventh harmonic coincides with the Au surface plasmon at ~ 2.4 eV. If the beam is positioned at L/4, the second harmonic is strongly excited as well as the fifth and sixth harmonics. At L/8, the fourth harmonic is also observed in the spectra. Further approaching the short slit wall leads to all harmonics being excited with similar intensities for the modes of order 2-6. Higher order modes remain weak. The fundamental mode decreases in intensity and is not observed in the spectra taken at L/64. Point measurements at these specific ratios of the slit length were also obtained in all double-slit systems to accurately measure the energies of the individual harmonics.

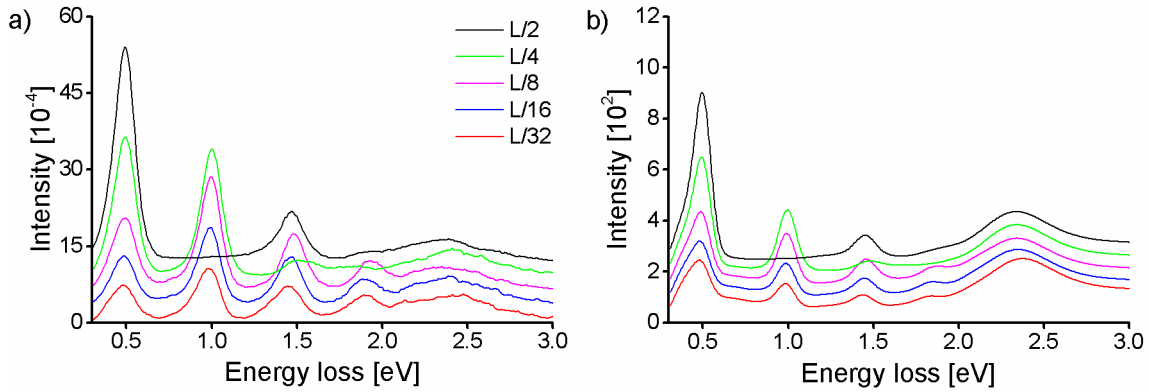

Figure 4.3.4 a) Experimental and b) simulated spectra obtained at various positions in a double slit with L = 960 nm and d = 100 nm.

To confirm the observed behavior of the cavity modes for various excitation positions along the long slit wall, additional simulations were performed. Experimental spectra and simulations for the double-slit system with L = 960 nm and d = 100 nm are presented in Figure 4.3.4. The

measurement positions coincide with specific rations of the slit length L. The simulations agree well with the experimental data (Figure 4.3.4a) and reproduce small observed spectral variations. Upon approaching the short slit wall, all cavity modes experience a small red-shift which is observable in the graphs for the third and fourth harmonics. Interestingly, the third harmonic shows a small blue shift if the measurement position is shifted from the center of the slit to L/8, which is also found in the corresponding simulation.

Figure 4.3.5 shows EELS intensities obtained from line-scans at 10 nm distance to the central metal bar for the following slit lengths: a) L = 400 nm, b) L = 530 nm, c) L = 645 nm, d) L = 960 nm, e) L = 1300 nm, f) L = 1620 nm, g) L = 1900 nm, h) L = 2180 nm, i) L = 2340 nm, and j) L = 2530 nm. The color scales are different for each line-scan. Hence, direct comparison of intensities is not possible for the different slit lengths. All double-slit systems show Fabry-Perot-like behavior of the excited cavity modes. With increasing slit length, the fundamental mode shifts towards lower energy as already shown in the spectra presented in Figure 4.3.2. The fundamental mode is barely observed in some of the line-scans because this data was acquired early during the thesis work when the experimental parameters were not yet optimized. The double slit-system with L = 2530 nm (Figure 4.3.5j) in an exception, as the fundamental energy is too low to be accurately measured with the employed microscope. It seems to be slightly excited in the center of the slit but seems to merge with the 2^{nd} harmonic with increasing distance from the slit center before it vanishes. The maximum observed mode order also increases with the slit length. In the double-slit system with L = 400 nm, only the fundamental mode and the second harmonic are excited, whereas even the 11^{th} harmonic is detected for L = 2530 nm. Spectral shifts for particular harmonics, especially for the 2^{nd} and 3^{rd} harmonic, are observed in the shorter double-slit systems for L = 400 nm up to L = 1900 nm. A slight red-shift is observed when the short slit wall is approached. The Au surface plasmon at 2.4 eV is present in all line-scans.

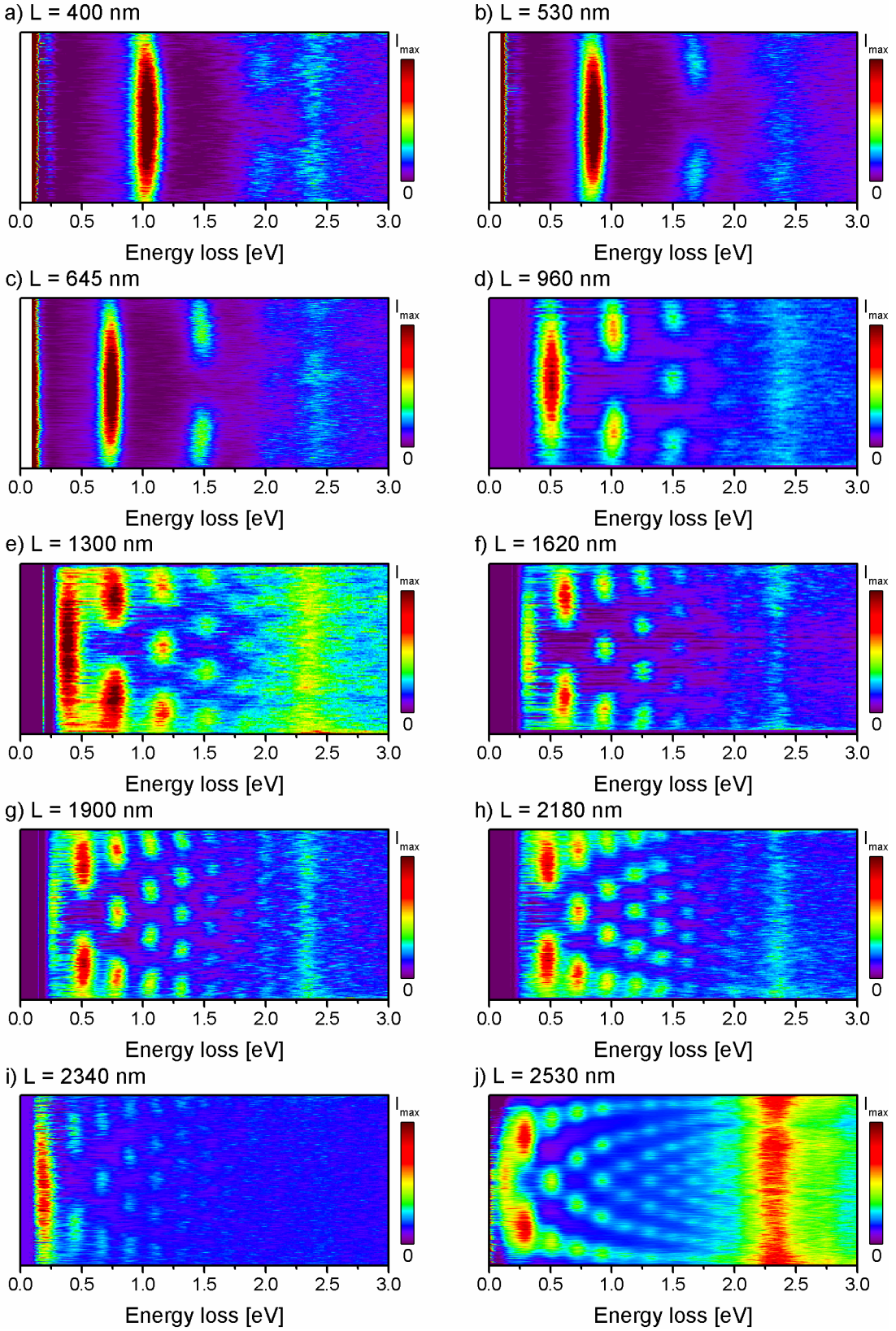

Figure 4.3.5 Color-coded EELS intensity along line scans obtained at 10 nm distance to the metal bar for all analyzed double-slit systems with slit lengths of a) L = 400, b) L = 530, c) L = 645, d) L = 960, e) L = 1300, f) L = 1620, g) L = 1900, h) L = 2180, i) L = 2340, and j) L = 2530 nm. Color scales are different for all scans. The vertical axis is set to cover the full slit length.

To compare all double-slit systems, spectra similar to the ones presented in Figure 4.3.3 were acquired to measure the energies of the individual harmonics. The results are depicted in Figure 4.3.6a. As already observed in the line scans, an increase in the slit length leads to reduced fundamental energy and higher mode orders are excited. Cavity modes were not detected for energies exceeding 2.2 eV as the Au surface plasmon dominates the loss intensity in this part of the spectrum. The figure also includes 2nd-order polynomial fits of the presented data. Linear fits were not suitable to describe the data (with the exception of the slit lengths L = 400 and L = 530 nm) because the higher harmonics have energies that are too low for a linear relationship of the harmonic's energy and mode order. Figure 4.3.6b shows the fundamental energy E_1 versus the slit length L. A steady decrease of the fundamental energy is observed for increasing slit length. The fundamental energy is plotted against the reciprocal slit length in Figure 4.3.6c. A linear fit matches the experimental data with large confidence (i.e. corrected $R^2 = 0.998$). The fundamental energy of a double-slit system is then given by:

$$E_1(L) = 0.08\ eV + 0.393\ eV\ \mu m \cdot \frac{1}{L} \tag{4.1}$$

for a slit length L in micrometers.

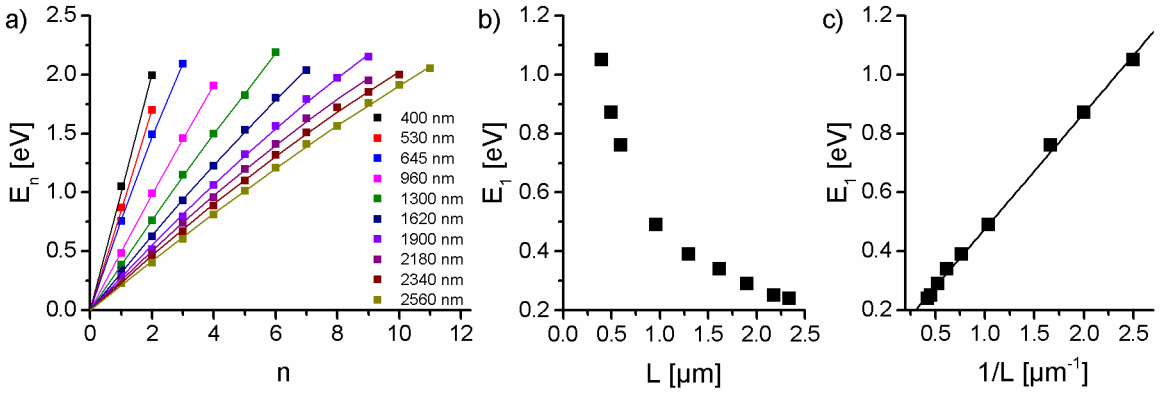

Figure 4.3.6 a) Energies of the harmonics in the double-slit systems plotted versus the mode order with 2nd-order polynomial fits of the experimental data. b) Fundamental energy E_1 plotted versus slit length L and c) reciprocal slit length 1/L. c) includes a linear fit to the data.

The cavity-mode wavelengths can be derived from Figure 4.3.5. Intensity profiles of the individual harmonics were taken at the respective energies with energy windows of 100 meV. Representative intensity profiles are exemplarily shown for L = 2530 nm in Figure 4.3.7. Up to the order of n = 9, all intensity profiles clearly show the expected number of intensity maxima. In the profile of n = 10, the maxima are not well resolved with signal intensities barely exceeding the noise level. To measure the positions of the maxima with improved accuracy, the profiles were smoothed by FFT filtering. The results are shown in Table 4.3.1 for all slit lengths up to the 6th harmonic and in Table 4.3.2 for the harmonics of orders seven to ten. Both tables also show the percent deviation of

the observed experimental wavelengths with respect to the nominal wavelengths which are given by $2\,L / n$. The fundamental wavelength is missing because it cannot be measured from experimental profiles. The distances between all extremes in the individual profiles were averaged for each mode order. Some profiles also show variation of the wavelength across the slit length but not consistently for all profiles and wavelengths. The wavelength of the 2nd harmonic exceeds the nominal wavelength in all double-slit systems with the average deviation being 14%. The wavelengths of the 3rd and 4th harmonics are also slightly larger than the nominal wavelengths with the average deviation of 6% and 5%. For all higher harmonics, the deviations decrease with increasing mode order and are – within the error margin – equal to the nominal wavelengths. The errors are not discussed in detail but it is obvious from the deteriorating signal-to-noise ratio that they tend to increase with increasing mode order.

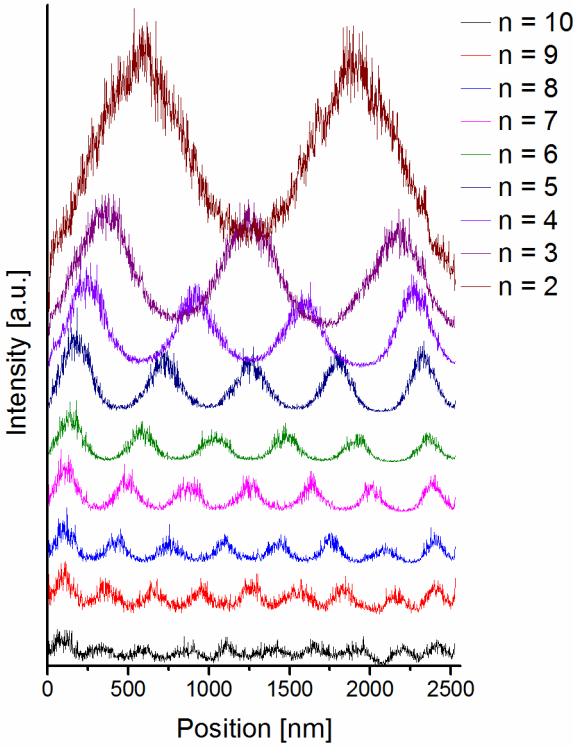

Figure 4.3.7 Extracted intensity profiles for the 2nd to 10th harmonic for the 2530 nm long slit (cf. Figure 4.3.5j) which were used to determine the mode wavelengths. The energy window for the extraction of the profiles was set to 100 meV.

L	n = 2		n = 3		n = 4		n = 5		n = 6	
400 nm	456 nm	14%								
530 nm	636 nm	20%								
645 nm	748 nm	16%	428 nm	0%						
960 nm	1100 nm	15%	680 nm	6%	480 nm	0%				
1300 nm	1520 nm	17%	950 nm	10%	693 nm	7%	545 nm	5%	424 nm	-2%
1620 nm	1940 nm	20%	1190 nm	10%	853 nm	5%	650 nm	0%	544 nm	1%
1900 nm	2220 nm	17%	1390 nm	10%	1007 nm	6%	800 nm	5%	656 nm	4%
2180 nm	2280 nm	5%	1530 nm	5%	1133 nm	4%	880 nm	1%	736 nm	1%
2340 nm	2720 nm	16%	1630 nm	4%	1220 nm	4%	965 nm	3%	796 nm	2%
2530 nm	2640 nm	3%	1810 nm	6%	1352 nm	6%	1076 nm	5%	890 nm	4%
Average	14%		6%		5%		3%		2%	

Table 4.3.1 Measured cavity-mode wavelengths to the 6^{th} harmonic in all double-slit systems. In addition, the percent deviations of the experimental wavelengths compared to the nominal ones, given by 2 L / n, are shown. The bottom-most line shows the average deviations.

L	n = 7		n = 8		n = 9		n = 10	
1900 nm	553 nm	2%	463 nm	-3%				
2180 nm	610 nm	-2%	523 nm	-4%	468 nm	-3%		
2340 nm	673 nm	1%	580 nm	-1%	515 nm	-1%	456 nm	-3%
2530 nm	758 nm	4%	658 nm	3%	575 nm	1%	515 nm	1%
Average	1%		-1%		-1%		-1%	

Table 4.3.2 Measured cavity-mode wavelengths of the 7^{th} up to the 10^{th} harmonic in double-slit systems with lengths between 1900 nm and 2530 nm. In addition, the percent deviations of the experimental wavelengths compared to the nominal ones, given by 2 L / n, are shown. The bottom-most line shows the average deviations.

The dispersion relation of the hybridized SSP cavity modes can be calculated from the measured wavelengths and energies. The wavelengths have to be converted to wave numbers with the relation $k = 2\pi / \lambda$ with the wavelength λ of the respective mode. Additionally, the light line is also calculated by $E(k) = h\,c\,k / 2\pi$ with the wave number k, Planck's constant h and the velocity of light c. The resulting dispersion relation is shown in Figure 4.3.8. The fundamental mode is omitted because its wavelength could not be experimentally determined. For small wave numbers $k < 4\ \mu m^{-1}$, the SPP dispersion closely follows the light line. For increasing wave numbers, the deviation from the light line is steadily increasing. The dispersion relation always remains on the right-hand side of the light line. As no SPP cavity modes were observed at energies exceeding 2.1

eV due to superposition with the surface plasmon, the behavior of the dispersion relation at larger wave numbers cannot be evaluated.

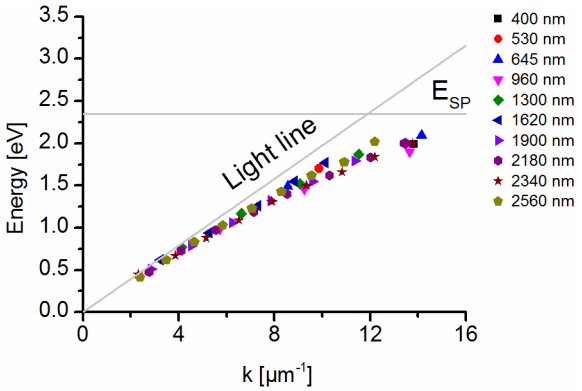

Figure 4.3.8 Calculated dispersion relation of the hybridized SPP cavity modes. The light line and the surface plasmon energy are also shown.

4.3.2 Discussion

The dependence of the slit length and the energy of the fundamental mode is the expected behavior of a resonant cavity. If the cavity length is increased, the wavelengths of the supported modes are also increased and hence the energy is reduced. This is not only the case for slits but is also observed for nanowires.[66, 93, 94] The graph in Figure 4.3.6c confirms the expected behavior as it shows a linear relationship of the fundamental energy and the reciprocal slit length. With the knowledge of the energy dependence, the analyzed slit structures represent an excellent test specimen to evaluate the performance of the employed spectrometer system. For example the lowest measurable energy can be determined by preparing a set of double-slit systems with increasing length. The fundamental mode of a 2070 nm long silver nanowire was reported at 0.17 eV.[66] The energy resolution may also be tested as the energetic separation of the individual harmonics of the cavity mode is also decreasing. The line scan shown in Figure 4.3.5j of a slit with length L = 2530 nm already shows these resolution effects as the fundamental mode and the second harmonic are difficult to separate. However, the fundamental lies at very low energy and therefore cannot be resolved accurately to the close proximity to the ZLP tail. The reduction in energy also leads to the observation of harmonics with higher mode orders as the spectral separation of the individual modes is also decreased. However, the upper limit for detection of higher harmonics is the surface plasmon energy at ~ 2.4 eV which can be explained by the dispersion relation shown in Figure 4.3.8. At first, the experimentally derived dispersion relation is in accordance to the expected one for SPPs (cf. Figure 2.1.1), i.e. for small wavenumbers it closely follows the light line but starts to deviate from it for increasing wavenumbers. It also

asymptotically approaches the energy of the surface plasmon for large wavenumbers. Therefore, no cavity modes with energy higher than the surface plasmon energy are observed as the cavity modes emerge due to SPPs supported by the slit walls. As no SPPs exist at energies above the surface plasmon energy, no cavity modes exist as well.

Similar to the single slit, spectral variations also occur along the slit length. As evident from the point measurements in Figure 4.3.3 and Figure 4.3.4 as well as the line scans in Figure 4.3.5, the higher harmonics experience a red-shift for measurements close to the short slit walls. These shifts also appear in the simulations and are even of the same magnitude. As for the single slit, this also affects the wavelengths of the individual modes. According to Table 4.3.1 and Table 4.3.2, the wavelengths deviate from the nominal ones and the deviation is decreasing for increasing mode order. Following the argumentation for the single slit in section 4.2.2, this is related to the intrusion of the SPP modes into the metal. The data for this effect was quite sparse for the single slit as only the 2^{nd} and 3^{rd} harmonic could be evaluated in a slit of length L = 960 nm. The longer slits analyzed in this subchapter allow to confirm the effects observed in the single slit, as due to the increased slit length, more harmonics are available for wavelength measurements. Significant deviations from the nominal wavelength are observed for up to the 4^{th} harmonic. For modes with $n \geq 5$, the deviations become smaller than the measurement errors. The errors also increase slightly with increasing mode order as the intensity of the higher harmonics is steadily decreasing whereas the noise in the extracted profiles does not change significantly.

In conclusion, cavity modes with mode orders of up to 4 experience wavelength elongation as the SPPs extend into the metal film near the short slit walls. In case of harmonics with higher mode orders, the wavelength elongation only occurs in the direct vicinity of the short slit walls and therefore the average wavelength of these modes will not deviate from the expected, nominal wavelengths. Red-shifts of the higher harmonics also only occur in close proximity to the short wall and hence support the assumption that the extension of the SPPs into the metal film only affects the cavity modes in direct vicinity of the short slit walls.

4.4 Coupling between Slits in Double-Slit Systems

4.4.1 Experimental Results

As already outlined in the previous section, the intensity of the hybridized cavity modes is largely enhanced upon introduction of a neighboring slit. This will be discussed in more detail in this section. If a second slit is introduced, a new experimental parameter becomes available, the inter-slit distance, which is determined by the width of the metal bar d separating the two slits in the Au film. It is not to be confused with the pitch value denoting the center-to-center distance of the slits.

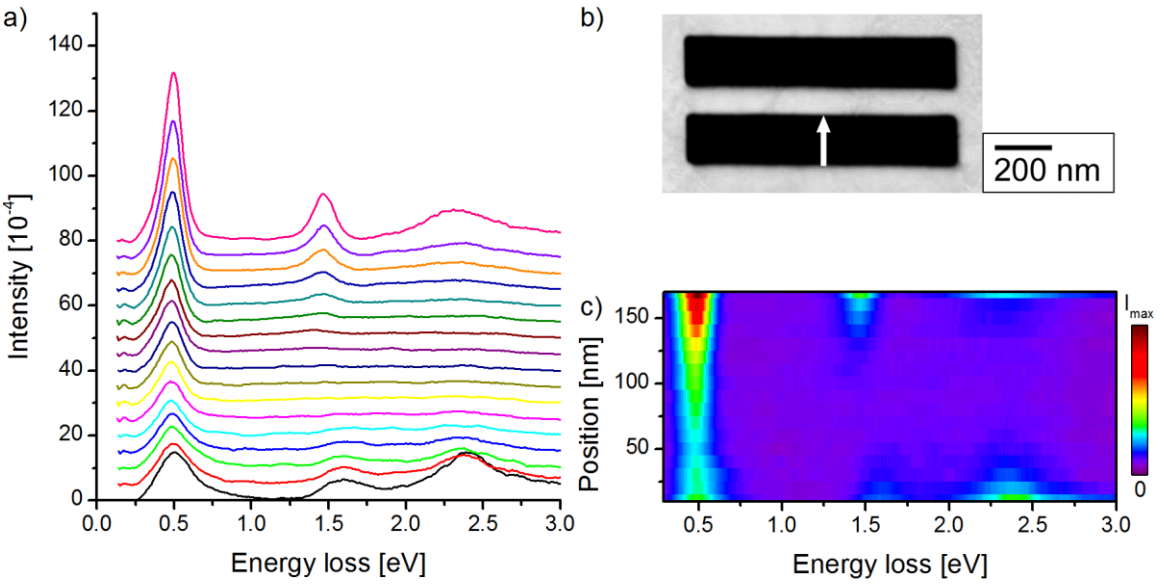

Figure 4.4.1 a) Spectra acquired in a double-slit system with L = 960 nm and d = 105 nm along the white arrow in the HAADF STEM image (b). The spatial distance between the spectra in a) is 10 nm. c) Color-coded EELS intensity map of the spectra from a).

Figure 4.4.1a shows spectra acquired in a double-slit system with L = 960 nm and d = 105 nm along the white arrow in the HAADF STEM image (Figure 4.4.1b). The spectra are also presented in a color-coded map in Figure 4.4.1c. At the outer wall (black spectrum at the bottom of Figure 4.4.1a), the fundamental ω_1, third harmonic ω_3, and the Au surface plasmon are observed. The intensity of the fundamental mode slightly decreases up to a distance of 50 nm from the outer wall and then begins to steadily increase as the inner wall is approached. ω_3 also weakens in intensity and is not observable in the spectra at distances between 50 nm to 110 nm from the outer wall. It increases in intensity close to the inner wall, however with a reduced enhancement compared to ω_1. Strikingly, it also undergoes a significant red-shift from 1.6 eV to 1.47 eV compared to the outer wall. The intensity behavior of the Au surface plasmon is similar to ω_3. However, in contrast

to the two SPP-related signals it is characterized by a lower intensity at the inner wall compared to the outer wall. To evaluate the above-mentioned behavior in greater detail, the exact energy positions and intensities in the spectra have to be analyzed. The third harmonic will not be discussed in such detail as its behavior cannot be similarly evaluated like the fundamental mode as it only shows intensity very close to the metal bar and, especially at the outer wall, it merges with the rising edge of the surface plasmon at 2.4 eV; rendering an exact analysis difficult.

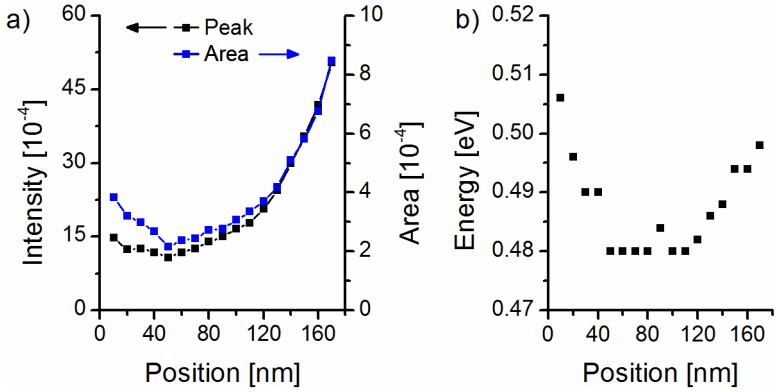

Figure 4.4.2 a) Peak and integrated intensity and b) energy of the fundamental cavity mode extracted from the EELS measurements in Figure 4.4.1 as a function of the distance to the outer slit wall.

Figure 4.4.2 shows the evolution of the fundamental cavity mode for the EELS measurements in the double-slit system with L = 960 nm. The ω_1 peak was fitted by a Gaussian function. The intensity presented in Figure 4.4.2a was measured either by the absolute peak height or the integrated area of the fitted Gaussian function. Both measurement methods yield different results close to the outer wall: the peak intensity is smaller than the integrated one. However, the peaks of ω_1 in the spectra of Figure 4.4.1a are broader close to the outer wall. Additionally, there is a small shoulder on the right-hand side of the peak which causes the increased integrated intensity close to the outer wall. Close to the inner wall, the intensity of ω_1 is identical for both measuring methods. The enhancement factors, which describe the intensity increase between the inner and outer walls, are 3.4 and 2.21 for the peak height and integrated intensities. The energy profile presented in Figure 4.4.2b shows variations of the energy E_1 of the fundamental mode across the slit. Starting from 0.51 eV it drops to 0.48 eV in the center of the slit and rises to 0.5 eV close to the inner wall. These shifts are, however, quite weak.

In addition to the experiments, simulations were performed for some of the slit structures. Figure 4.4.3 shows experimental spectra (Figure 4.4.3a) as well as simulations (Figure 4.4.3b) from a single and double slit with L = 960 nm. The electron beam was positioned at 20 nm distance from the respective walls. Qualitatively, experiments and simulations agree well with respect to the observed intensity and spectral variations. However, the simulations of the single slit result in a

small peak at 1.3 eV that is not observed in the experimental spectra. Also, the higher energy shoulder adjacent to the fundamental mode is more pronounced. It is noted that the simulated spectra of the single slit in Figure 4.4.3b was calculated for a distance of only 10 nm to the slit wall which causes the high intensity of the whole spectrum.

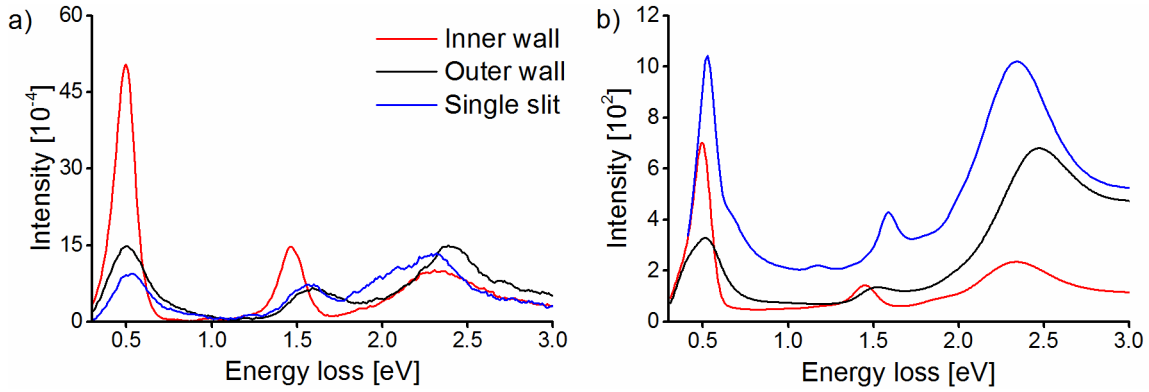

Figure 4.4.3 a) Experimental and b) simulated spectra from a single slit and a double slit with a length L = 960 nm and d = 100 nm. Measurements were performed at 20 nm distances from the respective walls.

Given this basic coupling behavior of two slits with a small metal bar width of d = 100 nm, it is now possible to check how a variation of the bar width affects the coupling behavior. For the case of the nominal slit length L = 960 nm, double-slit systems with the following bar widths were prepared: d = 270 nm, d = 680 nm, d = 880 nm, and d = 1800 nm.

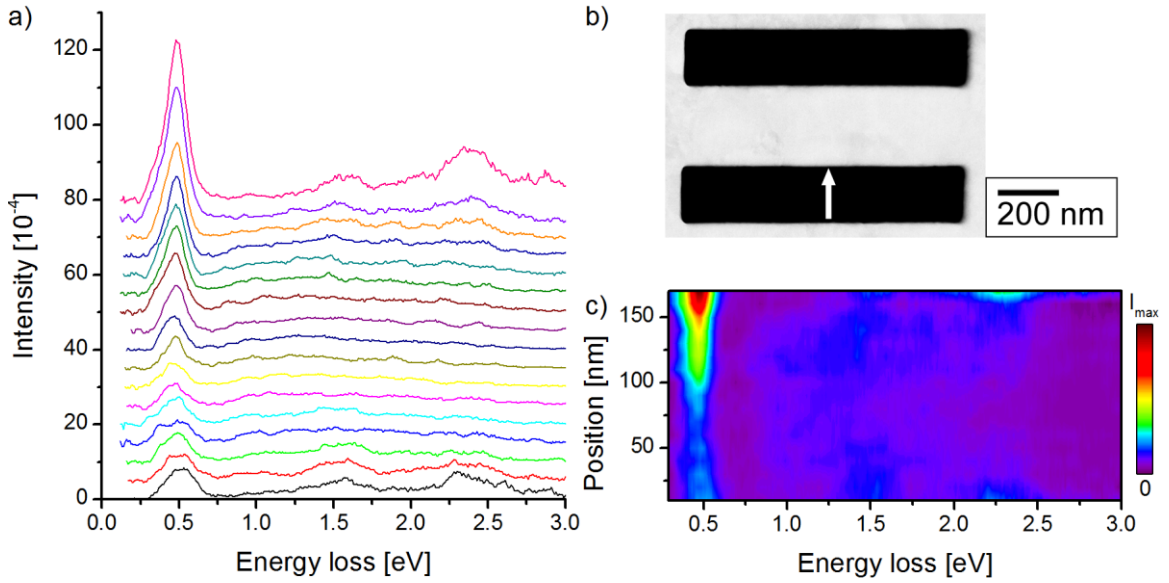

Figure 4.4.4 a) Spectra acquired in a double-slit system with L = 930 nm and d = 270 nm along the white arrow in the HAADF STEM image (b). The spatial distance between the spectra in a) is 10 nm. c) Color-coded EELS intensity map of the spectra from a).

Figure 4.4.4 shows measurements in a double slit system with L = 930 nm and d = 270 nm. In general, the presented data is not as clear as the one from the scan with a narrower metal bar. The spectra and the color-coded EELS intensity map are noisier. The evolution of the fundamental peak in the spectra shown in Figure 4.4.4a is similar to the measurements with a bar width of 100 nm, i.e., there is a decay of intensity if the distance to the outer wall is increasing. At about 70 nm distance to the outer wall, the intensity reaches its lowest value and then increases again upon approaching the inner wall. The behavior of ω_3 however is different than for the shorter bar width. No enhancement is observed if the inner wall is approached, rather, the intensity decays almost in the same manner in the vicinity of both walls. At distances larger than 30 nm, a peak is not observed in the spectra. Also, no spectral shift is found if measurements at both walls are compared. The intensity of the surface plasmon peak decays rapidly and vanishes for distances exceeding 30 nm from the wall. However, a slight enhancement is observed near the inner wall which is in contrast to the measurements with a bar width of only 100 nm.

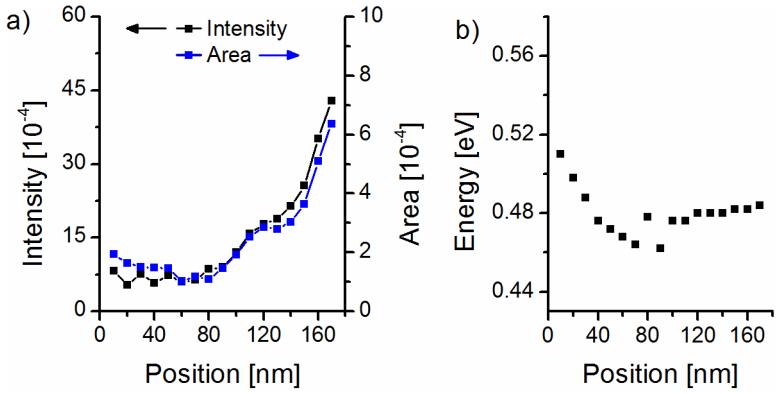

Figure 4.4.5 Peak and integrated intensity (a) as well as the energy (b) of the fundamental cavity mode of the scan from Figure 4.4.4

A more detailed analysis of the evolution of the fundamental mode is shown in Figure 4.4.5. The fundamental was fitted by a Gaussian function and the peak height and area of this fit were measured. The peak height shows little variation up to a distance of 70 nm to the outer wall. The integrated intensity on the other hand decreases for increasing distances and reaches its minimum also at 70 nm. Further increasing the distance shows a similar behavior for both measurement methods. There is a slight line narrowing of the fundamental peak for up to a distance of 70 nm which explains the minor differences in the profiles shown in Figure 4.4.5a. The enhancement factors are 5.22 and 3.28 for the peak-height and integrated intensities. They are higher than for a metal bar width of 100 nm. However this is caused by a significantly lower intensity at the outer wall. The intensities at the inner wall are also slightly reduced. Figure 4.4.5b plots E_1 as a function

of the distance to the outer slit. Starting at 0.51 eV, it drops to 0.46 eV at a distance of 70 nm from the outer wall. It rises to 0.48 eV when the inner wall is approached. Compared to the measurements in the slit with a narrower metal bar, there are some differences. The energy reaches its lowest value farther away from the outer wall and the stays almost constant at 0.48 eV, whereas for d = 100 nm it rises again to 0.5 eV.

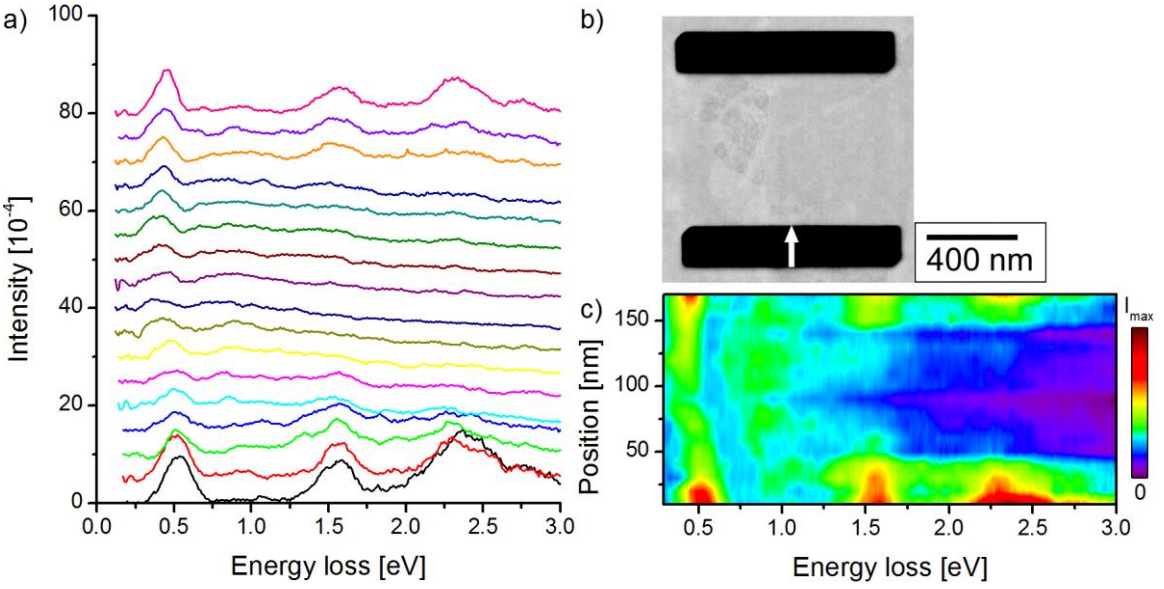

Figure 4.4.6 a) Spectra acquired in a double-slit system with L = 980 nm and d = 680 nm along the white arrow in the HAADF STEM image (b). The spatial distance between the spectra in a) is 10 nm. c) Color-coded EELS intensity map of the spectra from a).

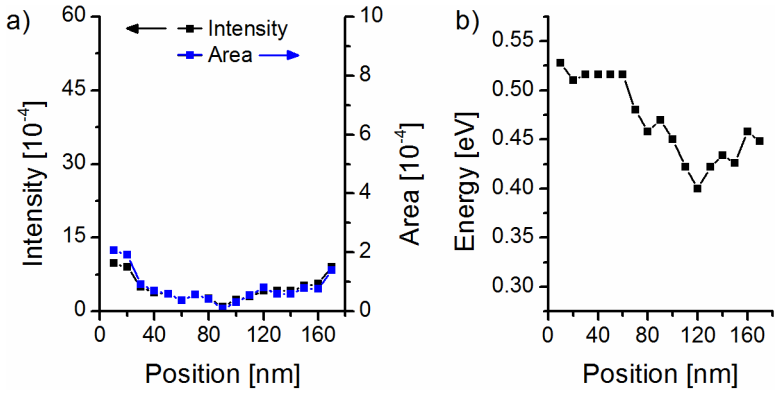

Figure 4.4.7 Peak and integrated intensity (a) as well as the energy (b) of the fundamental cavity mode of the scan from Figure 4.4.6.

Measurements in a double-slit system with L = 980 nm and d = 680 nm are presented in Figure 4.4.6 and Figure 4.4.7 in analogy to the double-slit systems with smaller d values. ω_1 is barely

visible in the center of the slit. Its intensity behaves similarly as in a single slit: it shows a symmetrical behavior with respect to the slit dimensions (cf. Figure 4.4.7a). However, spectrally, there are differences. For distances from the outer wall up to 80 nm, it gradually shifts from 0.53 eV to 0.42 eV (cf. Figure 4.4.7b). The energy is then nearly constant and only slightly shifts to 0.45 eV near the inner wall. Regarding the 3rd harmonic and the surface plasmon, both have increased intensity near the outer wall and do not undergo spectral variation (cf. Figure 4.4.6a,c). Both their intensities decrease for distances up to 60 nm from the outer wall and vanish inside the slit. Starting from 30 nm distance to the inner wall, they are observable in the spectra again. Additionally, as observed in the color-coded map in subfigure c, there seems to be a very broad and rather weak signal at higher energies compared to the fundamental. Its spectral variation closely follows the fundamental mode. The energy of the fundamental close to the outer wall is identical to the single slit energy but rapidly drops when the center of the slit is approached. The minimum value of 0.4 eV is reached at a distance of 120 nm to the outer wall (60 nm to the inner wall). The energy rises slightly to 0.45 eV near the inner wall.

The integrated intensity and energy profiles of ω_1 in the double-slit systems with L = 960 nm and d = 100, d = 270 nm, and d = 680 nm can be directly compared to the same profiles of the single slit to clarify the effects of coupling with a neighboring slit. Figure 4.4.8a shows the integrated intensity as a function of the distance to the outer slit wall. The intensity at the single slit wall is about $2.0 \cdot 10^{-4}$. It steadily decreases and nearly vanishes in the center. The double-slit system with d = 270 nm has roughly the same intensity at the outer wall and decreases when the slit center is approached. However, the minimum intensity is still larger than the one in the single slit and is slightly shifted towards the outer wall (i.e. at 70 nm). The double-slit system with d = 100 nm significantly differs from the other two as the intensity is always larger by about $2.0 \cdot 10^{-4}$. Its minimum intensity is shifted even more towards the outer wall (50 nm). The intensity profile for d = 680 nm is almost identical to the single slit, although the intensity near the inner wall is slightly reduced.

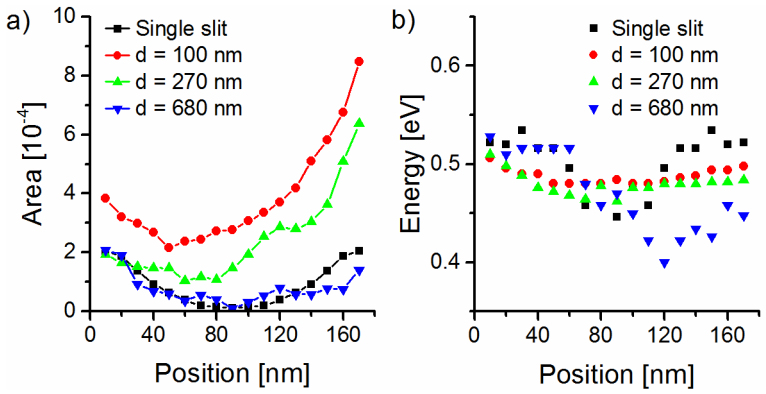

Figure 4.4.8 Comparison of the a) integrated intensity and b) energy of the fundamental cavity mode in double-slit systems (d = 100, d = 270 nm, and d = 680 nm) to a single slit as a function of the distance from the outer wall. The slit length is L = 960 nm for all slit structures. The profile of the single slit was mirrored at the center.

The energy profiles are shown in Figure 4.4.8b. The single slit's fundamental energy is 0.53 eV at the slit wall and roughly remains constant for distances up to 50 nm where it starts to be shifted towards lower energies at the center of the slit (~ 0.48 eV). In the double-slit systems with d = 100 nm and d = 270 nm, the energy is 0.51 eV near the outer wall and then further decreases towards the center. In the case of d = 100 nm, the energy slightly rises to 0.5 eV at the inner wall whereas it remains at 0.48 eV for the outer double-slit systems. The energy profile of ω_1 for d = 680 nm closely resembles the single slit for distances up to 100 nm from the outer wall. However, close to the inner wall, the energy is significantly lower compared to the single slit (~0.45 eV).

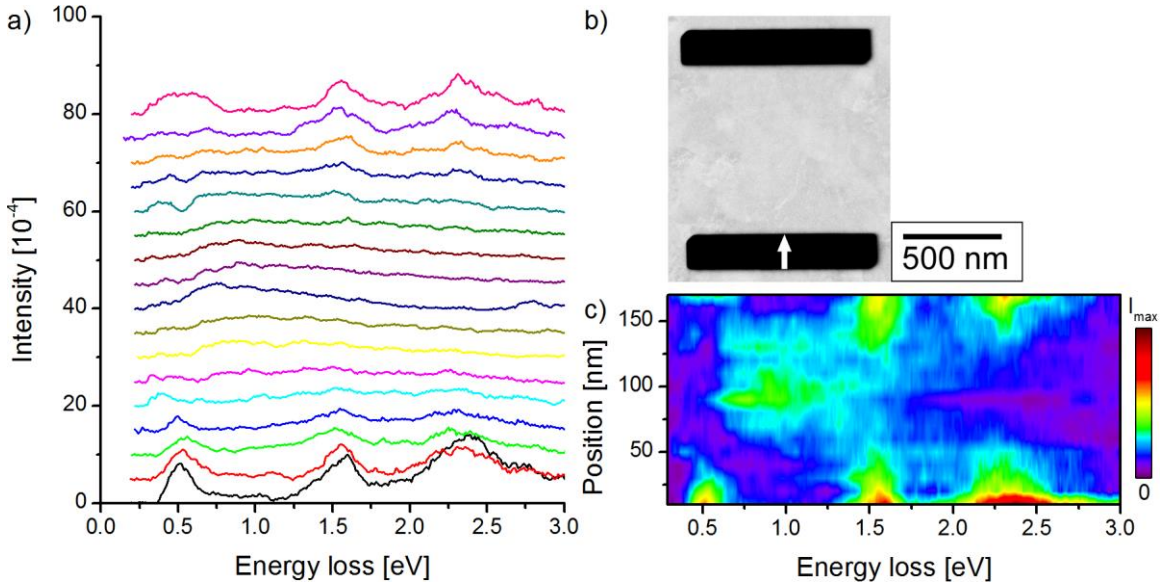

Figure 4.4.9 a) Spectra acquired in a double-slit system with L = 970 nm and d = 880 nm along the white arrow in the HAADF STEM image (b). The spatial distance between the spectra in a) is 10 nm. c) Color-coded EELS intensity map of the spectra from a).

A double-slit system with L = 970 nm and d = 880 was also analyzed. The results are shown in Figure 4.4.9. The intensity of all peaks in the spectra is further reduced compared to the data from the double-slit system with d = 680 nm. Only the spectra with distances equal or smaller than 40 nm from the walls can be analyzed. At the outer wall, the fundamental's intensity is comparable to the single slit and is located at an energy loss of 0.51 eV. For increasing the distance to the wall, the intensity rapidly drops and the peak energy slightly shifts to 0.5 eV. Only at the smallest distance to the inner wall, the fundamental can be observed clearly. However, it is a very broad peak centered at 0.5 eV. For larger distances to the inner wall, the fundamental appears to be split in two very faint signals at about 0.4 and 0.7 eV (cf. dark blue spectrum in Figure 4.4.9a). The 3rd harmonic and the surface plasmon peak show a similar behavior compared to the double-slit system with d = 680 nm.

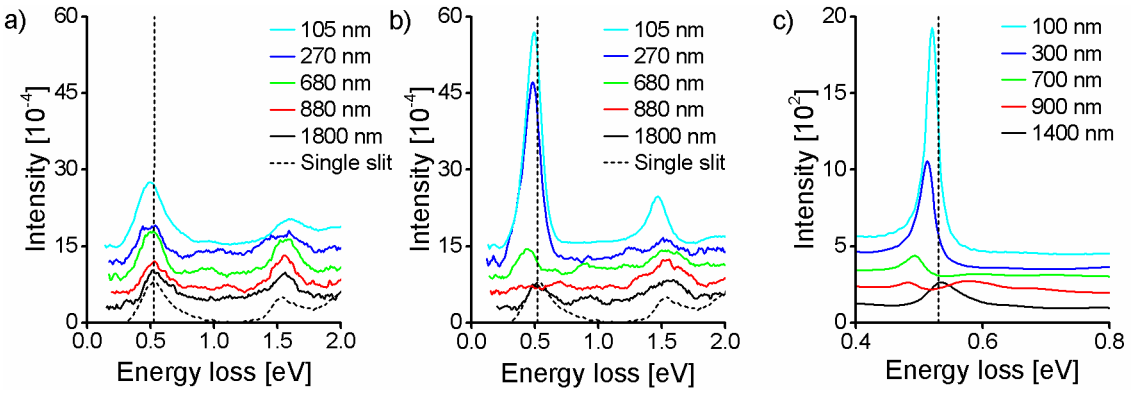

Figure 4.4.10 a) Spectra taken at 20 nm distance to the outer wall at L/2 in double-slit systems with varying inter-slit distance and inside a single slit. The fundamental energy in a single slit is marked with a vertical dashed line. b) Corresponding spectra acquired at 20 nm distance to the inner wall. c) Simulations corresponding to b).

To obtain a comprehensive overview of the effects of varying the inter-slit distance in double-slit systems, spectra taken at 20 nm to the outer and inner walls are compared in Figure 4.4.10. In addition to the data described above, measurements from a double-slit system with d = 1800 nm are included as well as data from a single slit for reference (dashed black line). E_1 of the single slit is marked by a vertical dashed line. Figure 4.4.10a shows spectra taken near the outer wall. Comparing the double-slit spectra with the single slit, barely any differences are observed. The fundamental is slightly enhanced in intensity for the shortest inter-slit distance of 105 nm. At 880 nm distance, the intensity is reduced marginally. Only minor spectral changes are observed for the fundamental. At 105 and 270 nm distance, it is shifted slightly to lower energy. For the other inter-slit distances, the spectral position of the fundamental is identical to the single slit. Spectra taken at the outer wall thus are quite similar to the single slit.

However, close to the inner wall (Figure 4.4.10b), the inter-slit distance has a huge effect on the individual spectra. For distances up to 680 nm, the fundamental mode shifts towards lower energy. At 880 nm inter-slit distance, it nearly vanishes. Only a weak, broad peak remains with a maximum at about 0.4 eV which is thus at even lower energy compared to the spectrum taken at 680 nm. However, for the largest distance of 1800 nm, it is again almost identical to the single-slit spectrum, although slightly reduced in intensity. In this case the influence of the neighboring slit seems to have vanished. Remarkably, the red spectrum (d = 880 nm) also shows an additional weak peak at a higher energy at 0.7 eV. Upon closer inspection, the spectrum taken inside the double-slit system with d = 680 nm also shows a weak peak at 0.9 eV. The behavior could be summarized as follows: ω_1 decreases in intensity and shifts to lower energy up to d = 880 nm. At a distance of 880 nm, a second, higher-energy mode appears. The single slit energy is reached at the largest distance of d = 1800 nm. Figure 4.4.10c (note the different scaling on the energy loss axis)

shows simulated spectra for an electron trajectory similar to Figure 4.4.10b. The simulations qualitatively agree well with the measurements although the observed energy shifts are reduced compared to the experimental data.

To obtain more data on the spectral shift and the intensity of ω_1, double-slit systems with systematically varied inter-slit distances and different slit lengths were prepared. As the fundamental lies close to the ZLP and is thus difficult to evaluate, especially at low intensities, the slit length was reduced. According to section 4.3 this results in an increased fundamental energy and facilitates the data analysis. However, another specimen series was investigated with longer slits to confirm the generality of the results. The following specimen series were prepared: double-slits with L = 535 nm and inter-slit distances d ranging from 90 to 1120 nm, double-slit systems with L = 645 nm and d = 110 to 1340 nm, and double-slit systems with L = 1330 nm and d = 90 to 2730 nm. The experiments on these specimens were performed by a master student, Stefan Fritz, who was supervised in the course of this thesis.

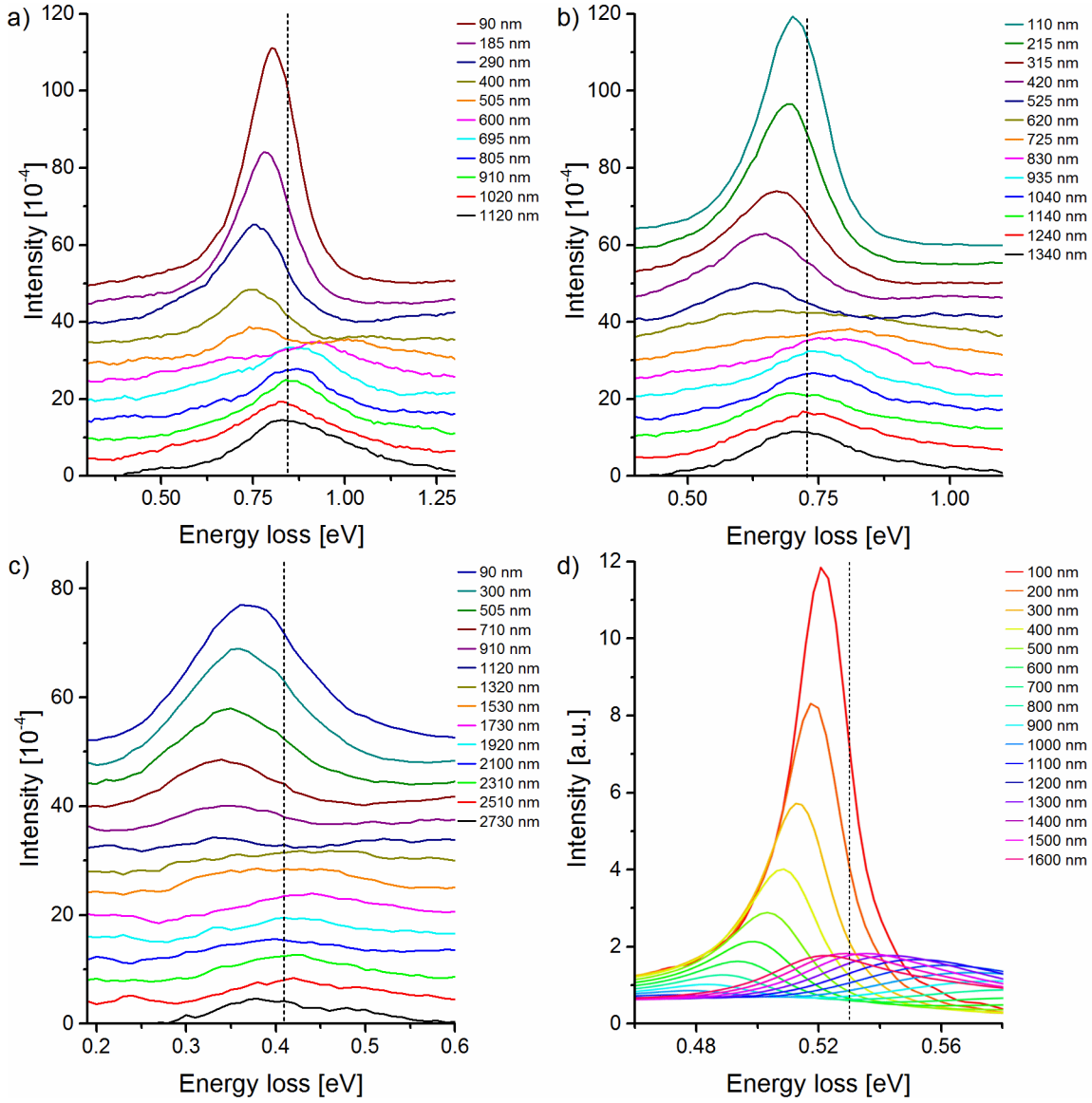

Figure 4.4.11 Spectra taken at 10 nm distance and L/2 to the inner wall in double-slit systems with lengths a) L = 535 nm, b) L = 645 nm, c) L = 1330 nm, and d) L = 960 nm (simulated) with different inter-slit distances d. The spectral position corresponding to the energy of the fundamental mode in single slits of the same length is marked with a vertical dashed line.

The results of these measurement series are shown in Figure 4.4.11. Each subfigure consists of spectra taken at 10 nm distance to the inner wall in double-slit systems with lengths of a) L = 535 nm, b) L = 645 nm, and c) L = 1330 nm. Simulated spectra for L = 960 nm are presented in Figure 4.4.11d. As a reference, the corresponding single slit energies (0.84, 0.73, 0.41, and 0.53 eV) are marked with vertical dashed lines. The inter-slit distance is increased roughly in 100 nm steps starting from the shortest distance of about 100 nm up to twice the slit length L. For the smallest inter-slit distance d = 90 nm in Figure 4.4.11a, the fundamental mode is already

slightly red-shifted. Upon further increasing d, the fundamental continuously shifts towards lower energy. For distances exceeding 600 nm, it is no longer resolved as a peak, but is barely recognizable as a shoulder that shifts to even lower energy. In addition, a second peak at higher energy is observed for d ≥ 400 nm that consecutively shifts to lower energy and reaches the single slit energy when the inter-slit distance is equal to twice the slit length. For the case of d = 505 nm, both peaks are observed and have roughly similar intensity. Basically two modes occur in the spectra, which will be denoted in the following as red-shifted and blue-shifted mode. The former is clearly observable and dominant for d < L whereas the blue-shifted mode dominates for d > L.

Figure 4.4.11b and c show the same behavior of the modes related to the variation of d with respect to the slit length L. The numerical simulations for L = 960 nm (Figure 4.4.11c) show the same behavior albeit with smaller overall energy shifts. To discuss the behavior independent from the particular slit length, the wavelength of the fundamental mode can be introduced to normalize the spectra and intensity variations. According to section 2.2 the nominal wavelengths can be calculated by $\lambda_n = 2L / n$ with the wavelength of the fundamental (n = 1) λ_1 corresponding to 2L. In the following, the behavior of the red-shifted and blue-shifted mode will be related to the ratio d/λ_1. The subscript '1' will be omitted from now on as only the fundamental mode will be discussed. To summarize the behavior in short: for $0 < d/\lambda < 0.5$ the red-shifted mode is dominant and for $0.5 < d/\lambda < 1$ the blue-shifted mode is dominant in the spectra. In the special case of $d/\lambda = 0.5$ both modes appear and have roughly the same intensity. d/λ will be henceforth denoted as the coupling parameter.

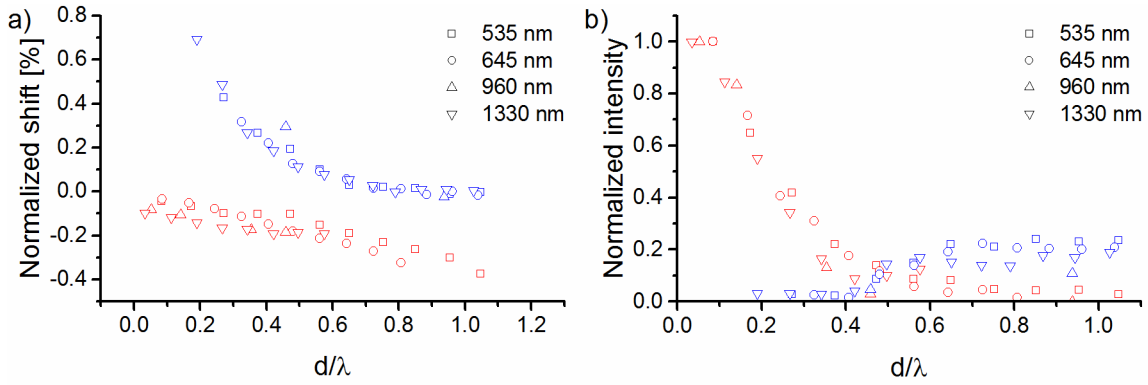

Figure 4.4.12 a) Normalized energy shifts and b) normalized intensities of the red- and blue-shifted fundamental mode as a function of d/λ for different slit lengths L as given in the legend. A normalized intensity of 0.3 roughly corresponds to the single slit.

For a comparison of the data sets of the different slit lengths, it is instructional to calculate the energy shifts normalized with respect to the single slit energy of the fundamental mode and plot them against the coupling parameter d/λ. The results are presented in Figure 4.4.12a. With

increasing d/λ, the red-shifted mode continuously shifts to lower energy. The largest shift is observed for the largest evaluated value of d/λ. For the blue-shifted mode, however, the largest shift is observed for the shortest distance between slits, i.e., where the blue-shifted mode first occurs in the spectra. Upon increasing d/λ, it also shifts towards lower energy and reaches the single-slit energy asymptotically. The smallest energy split between both modes occurs for $d/\lambda \approx 0.5$.

Figure 4.4.12b shows the normalized intensities of the red-shifted and the blue-shifted mode. The normalization was performed with respect to the highest intensity occurring in a single data set, i.e. the intensity of the red-shifted mode at the smallest inter-slit distance d. The intensity of the red-shifted mode drops rapidly for increasing d/λ. The blue-shifted mode on the other hand increases in intensity for $d/\lambda > 0.4$ and reaches its maximum at $d/\lambda = 0.7$. Further increasing the inter-slit distance does not alter its intensity. Both modes have similar intensity for $d/\lambda = 0.5$

The simulated spectra shown in Figure 4.4.11d were performed in the time domain. The extracted spectra are only a small portion of the overall data available after the computation. The electric fields, E_y and E_z related to the excited cavity modes were also recorded. In the following, the direction of the electron trajectory is defined to be the z-direction and the x-y plane lies parallel to metal film. The y-direction is oriented perpendicular to the long slit direction. Figure 4.4.13 shows the color-coded E_y amplitude in double-slit systems of a length L = 960 nm as a function of time and two inter-slit distances, namely d = 100 and 900 nm. In addition to the field in the excited slit (containing the electron trajectory), the field in the neighbor slit was also extracted from the simulation. The electron propagates along the positive z-direction (i.e. down to up) and reaches the bottom side of the film at t = 0s. The excited slit with d = 100 nm (Figure 4.4.13a and c) is discussed first. For the first few femtoseconds after the electron has passed, the field is chaotic. However, after 15 fs, an oscillating field builds up with a period of about 7.7 fs which translates to an energy of 0.54 eV. The fundamental cavity mode has a similar energy and the E_y-field should be therefore directly related to the cavity mode. In the neighbor slit (Figure 4.4.13c), a similar behavior is observed although the field amplitude is slightly smaller than in the excited slit. The cavity mode is also excited in the neighbor slit, although its phase is shifted by π as seen from the anti-symmetric behavior of E_y ("red" and "blue" E_y values in Figure 4.4.13a and c). Hence, the cavity modes in both slits are anti-symmetric for d = 100 nm.

Increasing the inter-slit distance to 900 nm significantly alters the observed behavior. The arising E_y-fields are reduced in amplitude and no clear oscillation builds up in the excited slit up to ~ 10 fs (Figure 4.4.13b) due to the chaotic behavior after the electron has passed. For times between 20 and 30 fs, the period seems shortened with respect to the double-slit system with d = 100 nm (cf. Figure 4.4.13c) which translates to a blue-shift. Upon approaching the 40 fs time the period increases which corresponds to a red-shift. This hints to two excited modes.

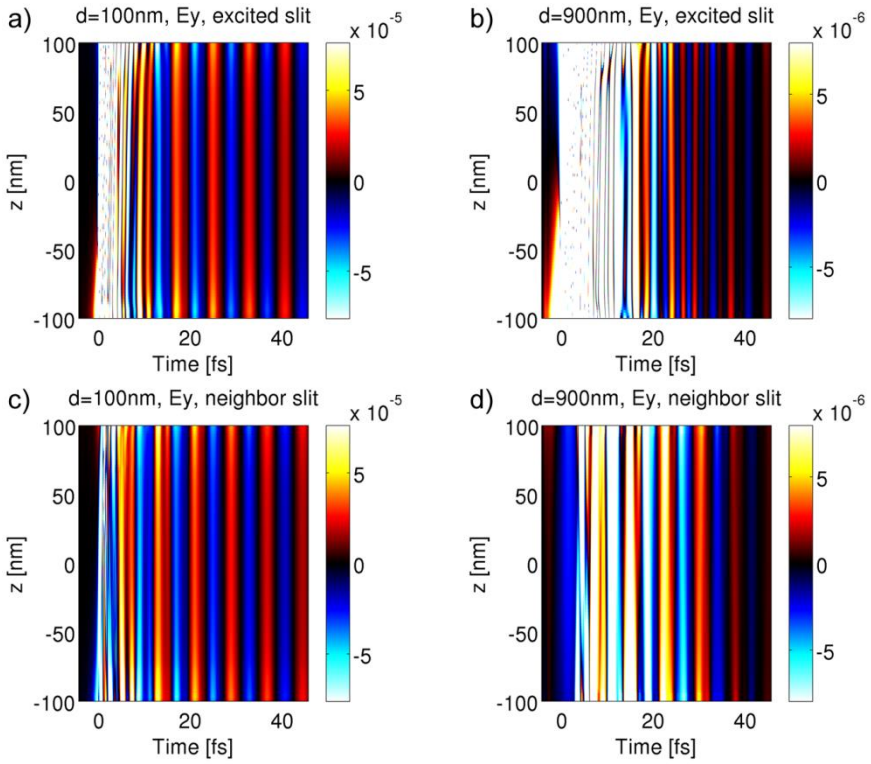

Figure 4.4.13 Color-coded simulated E_y-field amplitude in double-slits with L = 960 nm. Left panels: d = 100 nm, right panels: d = 900 nm. Upper panels: excited slit, bottom panels: neighbor slit. The electron trajectories are at 20 nm distance to the respective walls of the metal bar. The Au film thickness was assumed to be 200 nm with z = ± 100 corresponding to upper and lower film surfaces.

4.4.2 Discussion

The coupling of neighboring slits in a double-slit system has various aspects which will be discussed in separate subsections. The discussion is limited to the fundamental mode ω_1. Starting point is ω_1 inside a single slit which was shown to split up into a symmetric and anti-symmetric mode depending on the hybridization of SPP supported by opposite slit walls (SPP_{walls}; cf. section 4.2.2). The coupling of these two modes with a neighboring slit is discussed with respect to the intensity and spectral variation. The following section is focused on the nature of the SPP on both film surfaces (SPP_{film}) that mediate the coupling between slits. Specifically, their wavelength and their propagation characteristics and the related intensity variations are discussed. To complete this section, the differences between probing cavity modes with STEM EELS and EFTEM are briefly touched.

4.4.2.1 Effect of Coupling with a Neighbor Slit on the Energy and Intensity of the Fundamental Cavity Mode

Starting with the comparison to the single slit, the influence of a neighboring slit can be analyzed. In this subsection, the energy and intensity of ω_1 inside a single slit always refers to the anti-symmetric, low-energy mode of the single slit (cf. Chapter 4.2.2). It was shown in Figure 4.4.8a that the intensity of the fundamental cavity mode is always significantly higher for the double-slit system with d = 100 nm compared to the single slit, even at the outer wall. Therefore the existence of a second slit at 100 nm distance to the first one still has an influence on the outer wall of the first slit. The same is the case for d = 270 nm, although the effect is less pronounced. Nevertheless for distances exceeding 30 nm to the outer slit wall, the intensity is higher compared to the single slit. This is also applies when the point with minimum intensity is analyzed which occurs at 50 nm, 70 nm, and the center of the slit for d = 100 nm, d = 270 nm and the single slit. The largest spatial displacement is observed at d = 100 nm for which the overall intensity and its enhancement near the inner wall is strongest. The effect can be understood by the superposition of the single-slit intensity profile with the enhancement profile of the coupling to the second slit. As the enhancement is strongest for short inter-slit distances, the minimum intensity is shifted towards to the outer wall.

The intensity of ω_1 mode is not only affected by the coupling to a second slit, but there is also a slight enhancement due to the hybridization with SPPs on the slit walls, which was reported by Carmeli et al.[14] To separate the influence of the coupling to a second slit from the hybridization-related enhancement, the latter is removed. A simple way to do this is to subtract the intensity profile of the single slit from the intensity profiles in the double-slit systems. As no full transversal scan from a single slit was acquired due to the expected symmetry, the single slit profile is simply mirrored at the slit center and the symmetric profile is then subtracted (cf. Figure 4.4.8a). The result is presented in Figure 4.4.14.

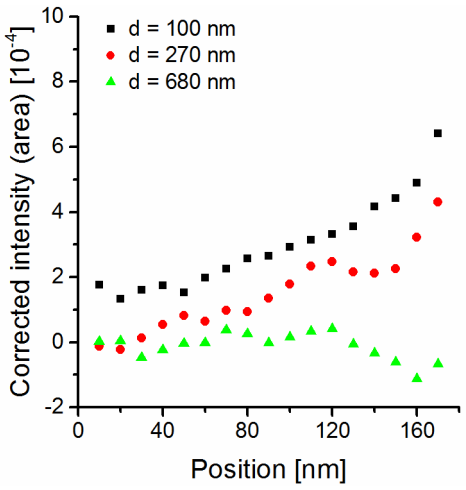

Figure 4.4.14 Intensity profiles of the enhancement due to only the influence of a neighboring slit. The hybridization-related enhancement was removed by subtracting a single-slit profile.

Clearly, the influence of the second slit is recognized even at the outer wall for of d = 100 nm. For d = 270 nm however, the onset of enhancement is shifted to 30 nm distance from the outer wall. For these two inter-slit distances, the enhancement increases almost linearly upon approaching the inner wall. Only for the last 20 nm, it deviates from this behavior which may, however, be related to imperfect beam positioning. Close to the inner wall, the intensity is rises sharply and even if the beam is only shifted by 1 nm, it will have a profound effect on the observed intensity. For d = 680 nm, intensity enhancement is not observed at all. Close to the inner wall, the intensity is even lower compared to the single slit which may indicate mode splitting already occurs at this inter-slit distance. Figure 4.4.14 only plots the red-shifted mode and hence, if a part of the intensity is transferred to the blue-shifted mode, a loss of intensity occurs for d = 680 nm. The double-slit system with d = 880 nm is not included because only spectra acquired close to the walls can be analyzed. Hence, data is not available for comparison of the intensity enhancement to the other inter-slit distances.

Not only the intensity profiles are indicators of the coupling, the energy shifts have to be considered as well (cf. Figure 4.4.8b). The fundamental energy of the single slit already shifts significantly (about 50 meV) to the red in the center of the slit. For the double slits with d = 100 nm and d = 270 nm, there is a slight shift towards lower energies in the slit center slit but less pronounced compared to the single slit. The energy at the outer wall is also already shifted by 20 meV towards lower energies. However, at d = 680 nm, differences compared to the single slit do not occur for distances up to 90 nm from the outer wall. This indicates that the effect of coupling on the energy reaches the outer wall only for small values of d. At d = 680 nm, the energy reaches its lowest value of ~0.41 eV at 120 nm distance to the outer wall. At the inner wall,

the energy of ω_1 is shifted to the red compared to the single slit. This red-shift is more pronounced for increasing inter-slit distances. The increasing red-shift of the fundamental mode is observable in all analyzed data sets, both experimental and simulated. Relating these red-shifts to a common coupling parameter to all sets, i.e. d/λ, enables the comparison of the data from different double-slit systems (cf. Figure 4.4.12a). For increasing d/λ, the fundamental mode continuously shifts towards lower energy, and its intensity nearly vanishes for $d/\lambda > 0.5$. Only for the short slit lengths of L = 535 and 645 nm it is still discernible in the spectra (not shown here, work of S. Fritz) as the fundamental energy in these slit systems is at higher energy and therefore separated further from the tail of the ZLP (cf. Figure 4.3.5a,b). In case of the longer slits, the increasing red-shift yields signals at very low energy losses which cannot be evaluated anymore. However, the red-shift is still observable for further increasing the distance between slits. In addition to the red-shift, the fundamental mode's intensity is decreasing rapidly for increasing d/λ. This decrease in intensity will be considered in detail in section 4.4.2.3.

A blue-shifted mode at emerges higher energies emerges for $d/\lambda > 0.2$ (cf. Figure 4.4.12a). The blue-shift decreases for increasing the coupling parameter d/λ. For $d/\lambda > 0.7$, the blue-shifted mode reaches the respective single-slit energy of the data set. Intensity-wise, the second mode is weak at first and starts to increase for $d/\lambda > 0.4$ (cf. Figure 4.4.12b). The intensity of the red-shifted and blue-shifted mode is nearly identical for $d/\lambda = 0.5$. With further increase of the distance between slits, the intensity of the blue-shifted mode approaches the single-slit intensity.

Such mode splitting is also observed for coupled harmonic oscillators[98] or binding atomic orbitals.[99] In these cases, two degenerate states (i.e. the two oscillators or orbitals of two atoms) lift their degeneracy by coupling to each other. This leads to a symmetric and anti-symmetric coupled mode. In the case of the coupled harmonic oscillators, either both oscillators are in phase or anti-phase. The eigenfrequencies of the two modes deviate from the unperturbed frequencies of the single oscillators. The symmetric mode has an increased frequency whereas the anti-symmetric mode has a reduced frequency. Atomic orbitals also overlap symmetrically or anti-symmetrically when coupled. The energy of the system is affected by this coupling and in the case of the anti-symmetric overlap, the energy is reduced which leads to a covalent bond between the two atoms. A symmetric overlap has increased energy and no bond forms.

The analyzed slit systems behave similarly. Without coupling between two identical slits in a double-slit system, both slits will behave like a single slit with certain energy of the fundamental cavity mode. This system is degenerate as the modes in both slits are identical. However, if coupling occurs between the slits, the degeneracy is lifted due to the formation of symmetric and anti-symmetric coupling of the cavity modes in the two slits. Looking at the simulations of the E_y-field presented in Figure 4.4.13a,c for the small metal bar width of d = 100 nm, the fields are anti-

symmetric in the two neighboring slits. The fundamental mode in this double-slit system is also shifted to lower energy (and frequency). For the case of d = 900 nm, the spectra in Figure 4.4.10 and Figure 4.4.11 and the graph in Figure 4.4.12a show that both modes are present simultaneously in the double-slit system and hence two different frequencies should occur superimposed. Figure 4.4.13b does show indeed – depending of the time frame – both higher and lower frequencies. However, distinct frequencies cannot be determined.

Ögüt et al.[89] studied double-slits in a thin Ag film and were also able to detect mode splitting in EFTEM measurements as well as in numerical simulations for the 2nd to 4th harmonics[87] (cf. section 4.1 for experimental details). The fundamental mode energy was too low to be evaluated. However, the blue-shift of the symmetric mode in case of the 2nd harmonic is only 4% and 20% for the simulated and experimental data, respectively. Compared to the experimental data acquired in this work (Figure 4.4.12), the blue-shifts observed by Ögüt et al.[89] do not match at all. It is, however, questionable if the direct comparison is reasonable because our data is derived from the fundamental mode whereas theirs is from the 2nd harmonic.

Prangsma et al.[91] have studied slits in a 200 nm thick Au film (cf. section 4.1 for experimental details). They have investigated arrays consisting of three slits of size 100 x 260 nm for varying inter-slit distances of 240, 300 and 350 nm. This translates to values of the coupling parameter d/λ of 0.46 to 0.67. In a single slit, the fundamental cavity mode was observed at a wavelength of 680 nm. Inside the arrays (measuring close to a wall in the central slit), the observed wavelengths were 610, 640, and 670 nm and are thus all blue-shifted compared to the single slit. The blue-shift steadily decreases for increasing the inter-slit distance. Following our line of argumentation, for this range of the coupling parameter, both modes should be present although the anti-symmetric, lower energy mode would be only weakly excited. This expectation is confirmed by the data of Prangsma et al.[91] because they only observe the symmetric, blue-shifted mode. Even a quantitative comparison to our data is possible as the relative blue-shifts in their experiments (10%, 6%, and 1%) for the different values of the coupling parameter are of the same order of magnitude as in our data.

Similar mode splitting in another plasmonic system was reported by Alaverdyan et al.[87] (cf. section 4.1 for experimental details). They have analyzed chains consisting of two or eight nanoholes with a diameter ~70 nm in a 20 nm thin Au film. The inter-hole distances were varied between 30 and 390 nm. For the shortest distance they observed only one peak in the scattering spectra per nanohole in the chain of two holes which steadily shifted to lower energy for increasing the distance between holes. The intensity of this peak also steadily decreased and almost vanished for the largest distances. At intermediate distances, a second mode appeared at higher energy that increased in intensity. For the largest inter-hole distance, it reached the initial energy of the scattering peak for short distances. The chain of eight nanoholes showed qualitatively the same

behavior as the two-hole system although there is a slight blue-shift of ~30 nm for all spectra. This shift may be related to the larger size of the array or slight difference in the hole diameter.

4.4.2.2 Effect of Coupling on the Symmetric Fundamental Cavity Mode in a Single Slit

The observed mode splitting and its explanation only considers one mode in the two single slits that form the double-slit system. However, according to section 4.2.1 (page 34, Figure 4.2.2b,c), there are two modes present in a single slit that stem from the hybridization of the two walls supporting SPPs. Therefore, in principle, both of these modes should be affected by the coupling to a neighboring slit and hence four modes should be observed. Ögüt et al.[89] explained the mode splitting in a single slit by an energy-level scheme of the interaction of the two slit walls. A similar level scheme was proposed for a double-slit system containing four walls. They concluded that such a system should lead to four different modes. However, their numerical simulations showed that only the anti-symmetric mode of the single slit (for which the SPP on both slit walls oscillate in anti-phase) hybridizes with the second slit. This is also the case for the experimental measurements presented in this section.

The symmetric single-slit mode is weak in the measurements (Figure 4.2.2b) and the simulations (Figure 4.4.3) and thus may be undetectable in the double-slit systems because they show a strong enhancement of the anti-symmetric single-slit mode for small metal bar widths. However, this enhancement decreases with increasing metal bar width and, the peak shifts towards lower energy (cf. Figure 4.4.12). Hence, even if the symmetric single-slit mode is weak, it should emerge in the experimental data which is not the case. The excitation of the symmetric single-slit mode could be inherently not possible in the double-slit systems.

However, at the outer wall in double-slit systems (Figure 4.4.10a), there seems to be a small shoulder on the high-energy side of the fundamental peak, in particular for inter-slit distances of 100 and 270 nm. In addition, the energy of the fundamental mode is not strongly affected by varying the inter-slit distance although a slight red shift is observed for the above mentioned distances. This small red shift could be related to the discussion concerning Figure 4.4.14 which stated that the influence of coupling to a neighboring slit reaches the outer wall for small inter-slit distances. Therefore it seems that the symmetric single-slit mode may be excited even in double-slits, but not for measurements close to the inner wall.

4.4.2.3 Wavelength of the Coupling-Mediating SPPs

The hybridized cavity mode within a slit in a double-slit system is able to launch SPPs (denoted by SPP_{film}) on the top and bottom faces of the film. The $SPPs_{film}$ mediate the coupling between the slits and are able to excite cavity modes in the neighboring slit as well (cf. simulations in Figure 4.4.13). The decrease in intensity of the cavity mode (cf. Figure 4.4.12a) is independent of the

particular slit length which is unexpected as the $SPPs_{film}$ have to propagate a larger distance on the metal film in the case of the longer slits. However, the cavity mode wavelength increases with the slit length L (cf. section 2.2) and hence, the propagation distance normalized to the wavelength of the cavity mode is identical for fixed values of d/λ. Initially, the wavelength-dependent attenuation length of the SPPs (cf. equation (2.22)) may be considered to explain these findings, although, the attenuation length far exceeds the relevant distances in the double-slit experiments.[10, 100] Therefore, the attenuation length cannot be responsible for the observed intensity variation and must be related to another aspect of the $SPPs_{film}$. The wavelength of $SPPs_{film}$ is determined by the wavelength of ω_1. Since this wavelength is dictated by the slit length (cf. Figure 4.3.6) the particular inter-slit distance in a specific double-slit system does not affect the coupling between slits at all. This fact allows then to derive a common coupling behavior for double-slit systems that only relies on the fundamental nature of the hybridization between cavity modes and SPPs. The experimentally derived dispersion relation shown in Figure 4.3.8 is another indicator of the strong intertwinement of cavity modes and SPPs.

4.4.2.4 Specifics of SPP-Mediated Coupling between Slits

The ability of STEM EELS to probe the coupling behavior between slits is striking. Under monochromated conditions the electron beam current has an upper limit in the range of 1 nA. This roughly translates to a time span of 100 ps between single electrons present in the microscope. Hence, only one electron is in the vicinity of the specimen at any given time. A 300 keV electron reaches a velocity of ~ 0.7 c where c is the velocity of light in vacuum. It passes the 200 nm thick film in less than 1 fs. However, the interaction range between electron and specimen is not strictly restricted to the film thickness. According to Carmeli et al.[14], the electron can probe the cavity modes for distances up to 450 nm from the slit walls (i.e. in the center of a 4500 x 900 nm large slit). This leads to an effective interaction range of about 1 µm which is covered by the electron in 5 fs. However, considering the simulations of Figure 4.4.13a for d = 100 nm, the cavity mode does not occur until about 10 fs have passed. For d = 900 nm (Figure 4.4.13b), the time until the cavity mode is clearly observable is even longer (20 fs). The electron has already passed the specimen long before the cavity mode even builds up but is still able to probe it. The electron is able to probe the double-slit system as a whole even before inter-slit coupling has built up. The coupling happens at an even longer time scale because for both slits to couple, first the cavity mode has be excited in the first, followed by the launching $SPPs_{film}$. These in turn will excite the cavity mode in the next slit which itself will launch $SPPs_{film}$. This strongly suggests that SPPs propagate in both directions between slits on the film surface to mediate coupling between slits.

The ability of the electron beam to probe the system as a whole before the coupled cavity modes have built up is similar to a Fabry-Perot resonator.[101] The simplest Fabry-Perot resonator is a thin

slab of matter. Upon illumination with light, the light beam will be transmitted and reflected at each interface of the slab which leads to a myriad of beams that are multiply reflected inside the medium. Depending on the width of the slab, the refractive index and the vacuum wavelength of the light, distinct phase differences occur between reflected beams. If all beams are in phase, a transmission maximum occurs due to constructive interference. These transmission maxima are also observed for short pulses of light, e.g. when there is not sufficient time for the all the reflected beams to build up and interfere constructively. There will be reflections at the two interfaces even for a short pulse of light; however, the initial pulse will pass instantly through the slab of matter. Hence, the impinging pulse of light is able to probe the transmission behavior of the slab even though the resonant condition had no time to emerge.

4.4.2.5 Implications of the Mediating-SPP propagation on the Intensity Variation

Up to this point, only coupling parameters up to $d/\lambda = 1$ were discussed. Of course the behavior for $d/\lambda > 1$ cannot be deduced from the available experimental data, but a brief outlook on the possibilities will be given. Both the intensity as well as the energy of the fundamental cavity mode are similar to the single slit for $d/\lambda = 1$ (cf. Figure 4.4.12) which indicate the lack of effective coupling between the two slits. However, this is only the case for the fundamental cavity mode: for example for d = 1800 nm (cf. Figure 4.4.10), the spectrum acquired at 10 nm distance to the inner wall does show spectral differences to the single slit at energy losses > 0.7 eV. This indicates that the two slits still interact although the effects on the fundamental mode are not present. This also applies for $d/\lambda \rightarrow 0$ as a double-slit system with an inter-slit distance of 0 is in fact a single slit. Although, actually, this single slit has double the width as the slits comprising the double-slit system. However, here the limit $d/\lambda \rightarrow 0$ is meant to be a single slit with the correct width.

The behavior is fundamentally different for $d/\lambda = 0.5$: in this case, the symmetric and anti-symmetric modes are equally excited in the double-slit system and the two energy branches in Figure 4.4.12 are at their nearest which coincides with the strongest coupling between two modes.[102] It is speculatively suggested that effective coupling of the fundamental cavity mode does not occur for $d/\lambda = 0.5 \cdot n$ with an integer number n while strong coupling is observed for $d/\lambda = 0.5 \cdot (2n+1)$. Following this line of argumentation, there should again be two modes observable for $d/\lambda = 1.5$. On the other hand, such a distance (i.e. 2.88 µm for a slit length of L = 960 nm) may be too large for SPPs to reach the neighboring slit. However, depending on film roughness, SPPs have decay lengths in the order of millimeters.[10] Only further measurements can shed light on this range of inter-slit distances and, hence, give deeper insight in the coupling behavior.

It must be emphasized, that the strongest intensity enhancement is observed for short distances between slits and not at $d/\lambda = 0.5$ where the spectral coupling is strongest. It therefore seems that

the intensity enhancement is not related to the coupling and hybridization of the cavity modes in the two slits of a double-slit system. This could be related to the hybridized nature of the cavity modes and the SPPs. The cavity modes' intensity is strongly enhanced in the near field region close to the metal wall and hence close to the SPPs supported by the walls.[14] It may be concluded that the spectral variations shown in Figure 4.4.12a stem from the hybridization of the cavity modes in the two slits whereas the intensity variations in Figure 4.4.12b are related to a direct interaction of the SPPs on either wall of the metal bar. The spectral and intensity variations may therefore be treated separately. The spectral coupling is mediated by $SPPs_{film}$ propagating on the metal film whereas the strong intensity enhancement for $d/\lambda \rightarrow 0$ results from direct interaction of the SPPs supported by the inner slit walls (*not* the film surfaces). The latter statement is discussed in the following.

The simulations in Figure 4.4.13 and the observed slight red-shift show that the cavity modes in both slits are coupled anti-symmetrically for small metal bar widths. Again, the modes in question here correspond to the anti-symmetric single-slit mode for which the SPPs on both slit walls oscillate in anti-phase.

Figure 4.4.15 schematically shows the SPPs on the slit walls and the fundamental cavity mode inside the slits. Figure 4.4.15a refers to the low-energy single-slit mode resulting from anti-symmetric SPPs on the slit walls which is indicated by the positive and negative charge accumulations on the walls. SPPs oscillating anti-symmetrically correspond to anti-symmetrical plasma oscillations which in turn result in opposite charges on the walls when a snapshot of the oscillating system could be taken. The cavity mode is indicated inside the slit and couples in the double-slit system. Figure 4.4.15b shows that when the fundamental cavity mode couples anti-symmetrically in the two slits, the charge distribution at the slit walls will be mirrored at the metal bar. This results in SPPs on either side of the metal bar that oscillate in phase (cf. also simulations by Ögüt et al.[89]). In this case, the SPPs on the inner wall in the two slits interfere constructively and thereby are enhanced in intensity which also results in increased cavity mode intensity.

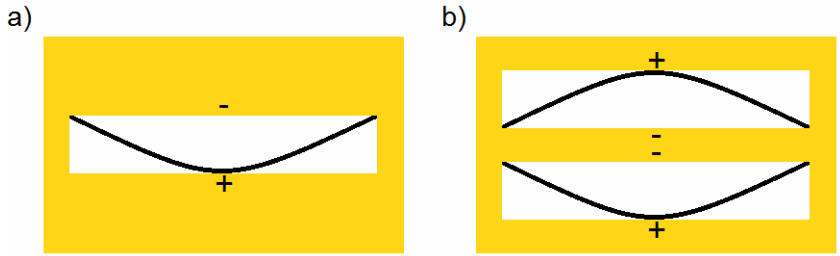

Figure 4.4.15 Schematic representation a) the low energy single-slit cavity mode resulting from anti-symmetric SPP on the walls (represented by charge symbols) and b) the mode from a) in anti-symmetric distribution in both slits leading to symmetric SPPs on both walls of the metal bar.

When spectral and intensity variations of the modes are separately considered, with the first one depending on the coupling parameter d/λ, and the latter one depending on d only, the normalized intensities in Figure 4.4.12b should differ for varying slit lengths. However, the intensity is independent of the particular metal bar width and depends only on d/λ. This could be related to the propagation geometry of the SPPs launched near the electron beam position at L/2. Figure 4.4.16 plots the electric field strength of the SPP propagation across the bottom face of the metal bar in a double-slit system with L = 960 nm and d = 100 nm. Three snapshots taken at t = 3.93 fs, t = 4.97 fs, and t = 5.45 fs were extracted from a simulated movie. At t = 0 fs, the electron passes the bottom face of the metal bar at L/2 and at 10 nm distance to the wall. The SPP is launched at the electron beam position and is propagating as a circular wave across the metal bar. The wave propagates in the half-space next to the slit and travels across the surface to the next slit.

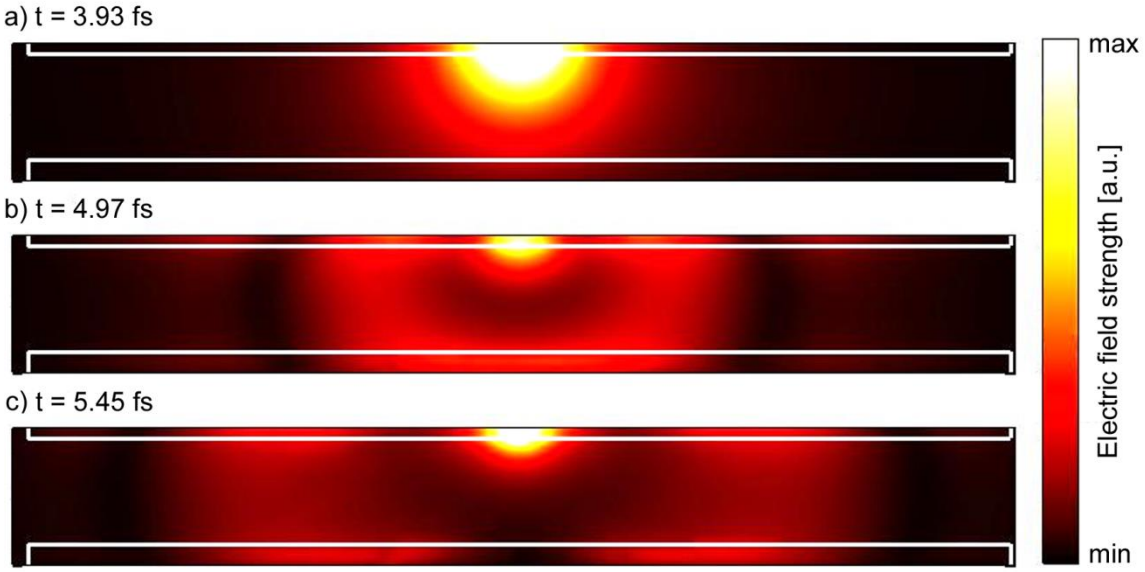

Figure 4.4.16 Snapshots of the electric field strength extracted at a) t = 3.93 fs, b) t = 4.97 fs, and c) t = 5.45 fs from a simulation movie of the SPP propagation across the bottom face of the metal bar (which the electron passes at t = 0 fs) in a double-slit system with L = 960 nm and d = 100 nm. The slit walls are indicated by white lines.

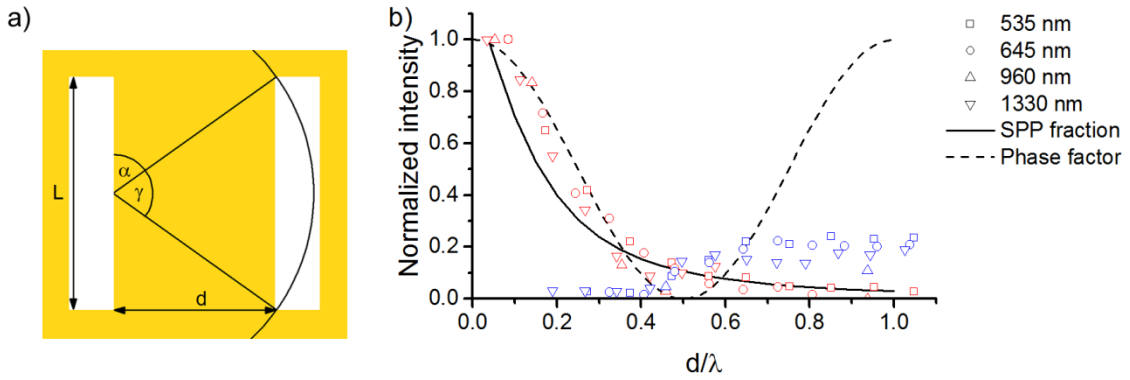

Figure 4.4.17 a) Geometry of a double-slit system. The electron beam excites the cavity mode in the left slit and launches a circular SPP at L/2 which propagates towards the right slit. Only a fraction *f* governed by the angle γ reaches the second slit. b) Calculated normalized intensity (solid black line) and normalized phase factor (dashed black line) with respect to d/λ compared to experimental data. Red and blue symbols correspond to the anti-symmetric and symmetric modes. (see also Figure 4.4.12).

As shown in Figure 4.4.17a, only a fraction of the initial wave (i.e. the sector defined by the angle γ) depending on the inter-slit distance reaches the second slit. The circular wave only covers the angle π rad because it starts at the slit wall and cannot extend into the slit. The fraction *f*

reaching the second slit is $f = (\pi - 2\alpha)/\pi = 1 - 2\alpha/\pi$ where α is derived by trivial geometry. For the coupling to take place, another SPP wave has to propagate back from the neighboring slit to the initially excited slit and hence f^2 governs the intensity loss. As the SPP wavelength depends on the slit length L, this geometric effect will be independent of the actual slit separation as the system geometry as a whole is only scaled up with increasing L. Figure 4.4.17b plots the calculated intensity loss due to this geometric effect along with the experimental data that was acquired in double-slit systems. Similar to the experimental data, the calculated intensity loss is normalized to the intensity measured for the shortest inter-slit distance corresponding to $d/\lambda = 0.038$ (i.e. a metal bar width of d = 100 nm for a slit length L = 1330 nm). The calculated intensity (solid black line in Figure 4.4.17b) is similar to the experimental data for the anti-symmetric mode (red symbols in Figure 4.4.17b), especially for $d/\lambda > 0.4$. This is contradictory to the intensity of the symmetric mode (blue symbols in Figure 4.4.17b) as the same geometry effect applies to this mode, too. However, the symmetric mode only emerges for larger inter-slit distances and reaches the single slit intensity and hence may correspond to the case where no intensity enhancement is observed due to coupling.

Another explanation for the intensity decay with respect to d/λ was reported by Walther et al.[103] Due to the propagation of the SPPs across the metal bar, the SPP reaching the neighbor slit acquires a phase difference ϕ which is given by $2\pi \cdot d/\lambda$. This phase difference results in the interference amplitude given by $1 + e^{i\Phi}$ which, intensity-wise, translates to $2 \cdot (1 + \cos \Phi)$. In other words, if the cavity modes present in either slit interfere constructively, their amplitude is doubled and hence the intensity is enhanced fourfold. Figure 4.4.17b also includes the normalized phase factor. For $d/\lambda < 0.5$, the phase factor fits the experimental data of the anti-symmetric mode (red symbols in Figure 4.4.17b) well. However, for $d/\lambda > 0.5$, the phase factor results in a strong enhancement of the intensity of ω_1, that is in contrast to the experimental data which only shows a small rise in intensity as the symmetric mode reaches the single-slit intensity.

In summary, the mentioned geometry effect and the phase factor are able to fit the experimental data of the anti-symmetric mode reasonably well although they are merely simple phenomenological models. On the other hand, both fail to fit the slightly rising intensity of the symmetric mode. This is another indication that the strong intensity variation for small d/λ is indeed separated from the spectral variation due to mode splitting. In the case of coupled harmonic oscillators[98], none of the two coupled modes is strongly enhanced compared to the other one. Rather, the intensity variation of the two frequency branches is symmetric, i.e. the intensities of both modes are equal when they are excited separately.

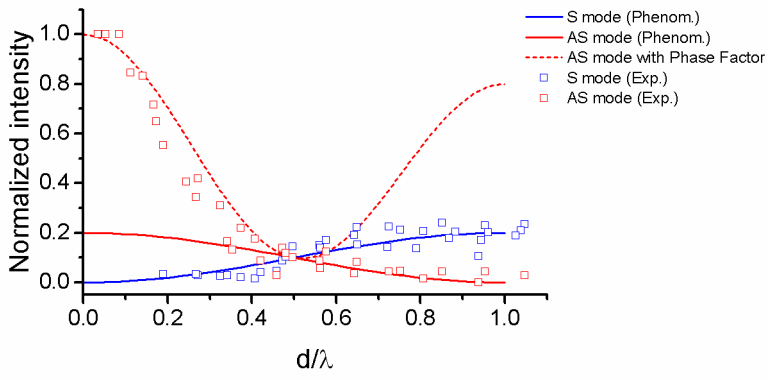

Figure 4.4.18 Phenomenological model showing the suggested mode splitting with symmetric intensity variations for the two energy branches (blue and red solid lines for symmetric and anti-symmetric modes) of Figure 4.4.12a. The red dashed line is the superposition of the anti-symmetric mode (solid red line) with a phase factor model. The experimental data of Figure 4.4.12a are shown with blue and red open squares.

Figure 4.4.18 shows a simple phenomenological model of the symmetric intensity variation of the two coupled modes calculated by sine functions. The symmetric and anti-symmetric modes are shown as blue and red solid lines. In addition, the strong enhancement of the anti-symmetric mode is incorporated by a phase factor (cf. section above, red dashed line) that is superimposed on the anti-symmetric branch. The experimental data from Figure 4.4.12b is represented by blue (symmetric mode) and red (anti-symmetric mode) open squares. The phenomenological model and the experimental data of the symmetric mode agree well for the complete range of d/λ. For $d/\lambda > 0.5$, the same also holds for the anti-symmetric mode. For $d/\lambda < 0.5$ the combination of the phenomenological model and the phase factor is able to reproduce the experiment. Although Figure 4.4.18 shows a very simple model, a combination of a strong enhancement of the AS branch for $d/\lambda < 0.5$ with a symmetric intensity distribution between the two modes for $0 < d/\lambda < 1$ agrees surprisingly well with the experimental results.

The selective enhancement of only the anti-symmetrically hybridized cavity mode can be explained by the SPPs on the slit walls on either side of the metal bar. Figure 4.4.15b suggested the SPPs on two walls of the metal bar are interfering constructively for the anti-symmetrically hybridized cavity mode. On the other hand, destructive interference of the SPPs on the two walls of the metal bar results for the symmetrically hybridized cavity mode. Hence, it is speculated that enhancement is not present in this case. However, the interaction of SPPs on the two walls of the metal bars will be severely hampered for large distances between the two slits and therefore ceases to affect the cavity mode intensity for $d/\lambda > 0.5$. Hence, a rise in intensity for the blue-shifted mode in this case is not contradictory to the above line of argumentation.

4.4.2.6 Probing Cavity Modes by STEM EELS and EFTEM

Positioning the beam close to either wall gives rise to a profound difference in the observed excitations. Near the outer wall, the probed cavity modes are similar to the single slit and only minor spectral and intensity variations are observed for increasing the inter-slit distance. Close to the inner wall, however, the beam probes the hybridized mode that stems from coupling to the neighboring slit. This fact poses a unique feature of STEM EELS compared to experimental methods that do not evaluate the system with a point-like probe, i.e. EFTEM or optical methods. EFTEM may probe all possible excitations present in a given system but is not able to relate the observed modes to particular excitation positions. For example, Ögüt et al.[89] were able to show the two modes that emerge from hybridization between two slits but it cannot be deduced from their data which mode is generated at which excitation position. EFTEM, however, gives direct access to the spatial distribution of the modes which is not possible with STEM EELS even if spectrum imaging is employed. Spectrum imaging gives access to the spatial distribution of the modes observed in the spectra but only for the particular mode that is excited at the measurement position. With respect to the data presented in this work, this means that the spatial distribution of the cavity modes coupled with the neighboring slit can be imaged (i.e. the line scans presented in Figure 4.3.5) for measurements close to the metal bar. However, the spatial distribution of the single-slit mode cannot be evaluated close to the metal bar as this mode may either not be excited at these measurement positions or may be too weak to be observed. This is the fundamental difference between STEM EELS and EFTEM measurements and at the same time, it directly shows the complementarity of the two methods. This complementarity was also shown for mapping LSP resonances in single nanoparticles.[104]

4.5 Slit Arrays

4.5.1 Experimental Results

The coupling of two closely spaced slit has a profound effect on the intensities and energies of the cavity modes. These observations motivate the investigation of slit systems with a larger number of slits. In the following section, arrays with 3, 4, 8, 20, and 60 slits were studied. All slit systems were prepared with a length of L = 960 nm and metal bar widths ranging from d = 100 nm to d = 680 nm between slits.

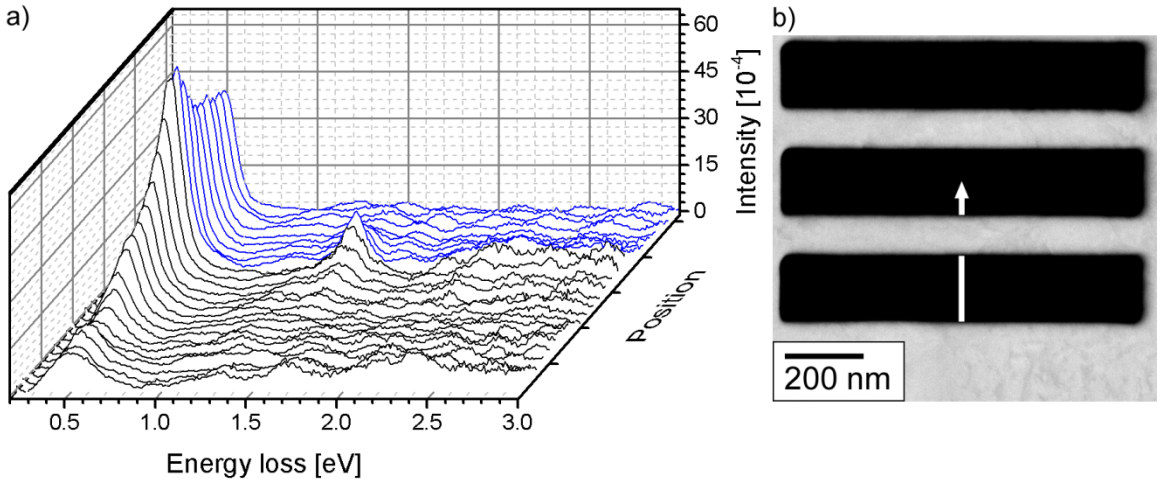

Figure 4.5.1 a) Spectra taken in a three-slit system with L = 960 nm and d = 100 nm. Blue spectra are taken in the central slit. b) HAADF STEM image with a white arrow indicating the measurement positions.

Figure 4.5.1 shows measurements taken inside a three-slit system with L = 960 nm and d = 100 nm. The spectra presented in Figure 4.5.1a were taken at L/2, beginning at the outer wall. The black spectra are from the first slit, whereas the blue ones were acquired in the central slit of the array. The line along which the spectra were acquired is marked in the HAADF STEM image Figure 4.5.1b by a white arrow. Only half the array was analyzed as symmetric behavior with respect to the beam position inside the array is expected. The intensity of the fundamental mode is low at the outer wall and increases when the inner wall of the first slit is approached. Inside the second slit, the fundamental intensity decreases slightly towards the slit center. However, it is still high compared to the spectrum taken in the center of the first slit.

To evaluate the behavior of ω_1 in the three-slit system with improved accuracy, intensity and energy profiles were extracted similar to the other investigated slit structures. The profiles are shown in Figure 4.5.2. Grey dashed lines indicate the positions of the metal bars between the two slits. The integrated intensity (Figure 4.5.2a) is small near the outer wall and decreases only slightly for distances up to 60 nm. From then on, the intensity is enhanced strongly towards the

inner wall of the first slit. Inside the second slit, the intensity drops with increasing the distance to the slit wall. However, the intensity reduction is smaller compared to the first slit.

The energy profile presented in Figure 4.5.2b is rather noisy but a red-shift of the fundamental mode from 0.5 to ~ 0.475 eV is observed for distances up to 60 nm from outer the wall followed by a shift towards higher energy (0.495 eV) at the inner wall. Inside the second slit, a slight red-shift from 0.495 eV to 0.485 eV is observed.

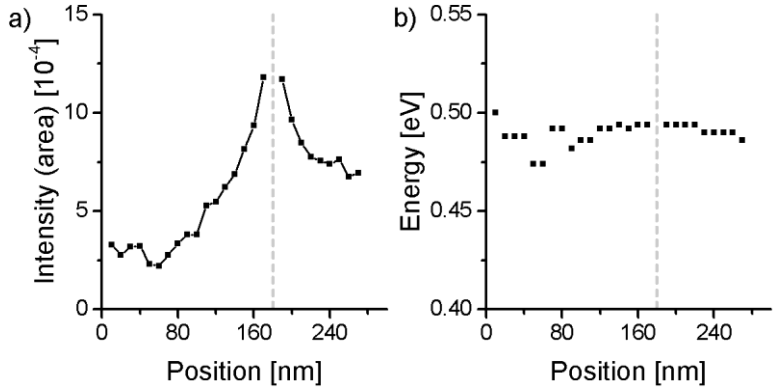

Figure 4.5.2 a) Intensity (area) and b) energy profiles of the fundamental mode as a function of the distance to the outer wall of slit 1 in the three-slit system shown in Figure 4.5.1. The grey dashed lines indicate the position of the metal bar separating the two slits.

Analogous measurements were carried out in a four-slit array and are presented in Figure 4.5.3. Only two slits of the four-slit array were scanned and the spectra are shown in Figure 4.5.3a. The outer slit's spectra are shown in black and those taken inside the inner slit in blue. The spectra were taken at L/2 along the line which is marked by an arrow in Figure 4.5.3b. The dependence of the intensity of the fundamental mode resembles that of the three-slit system: it is low at the outer wall and increases towards the inner wall of slit 1. In the second slit, the intensity decreases at the center, and rises towards the walls. The maximum intensity in the first slit is lower compared to the maximum inside the second slit.

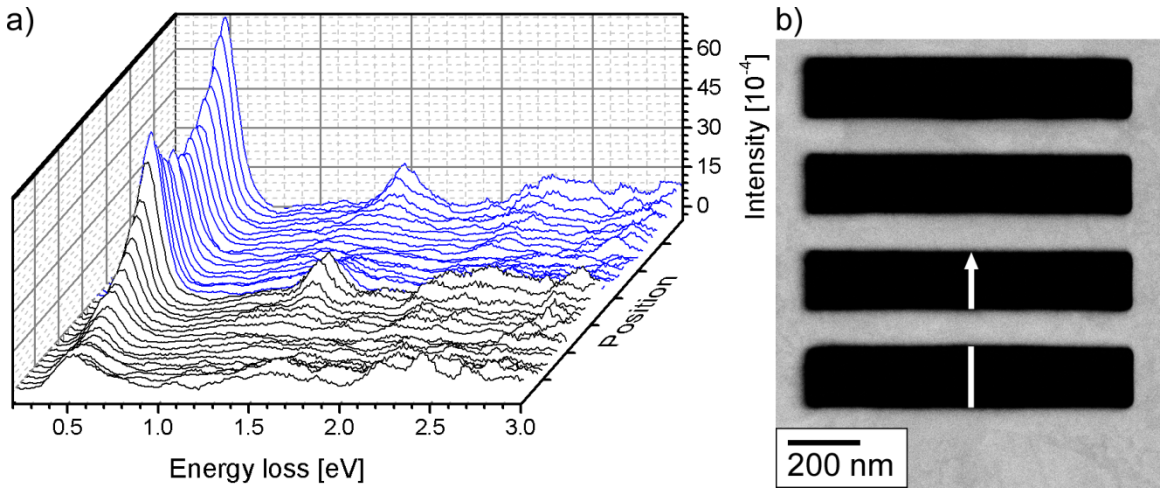

Figure 4.5.3 a) Spectra acquired inside the first two slits of a four-slit array with L = 960 nm and d = 100 nm. Measurements in the first and second slit are shown in black and blue. b) HAADF STEM image of the four-slit array with a white arrow indicating the line along which the spectra were acquired.

A clearer picture of the behavior of the fundamental mode can be gained from the extracted profiles of the integrated intensity and energy shown in Figure 4.5.4. The fundamental mode intensity (Figure 4.5.4a) is low at the outer wall and is slightly reduced for distances between 20 and 70 nm (expect an outlier at 40 nm). Further increasing the distance from the outer wall gives rise to an enhancement of the intensity. At the outer wall of the second slit, the intensity is higher compared to the maximum intensity inside the first slit. There is an intensity minimum close to the slit center. The intensity strongly rises towards the inner wall of slit 2 and exceeds the intensity obtained close to the outer wall. Also, the minimum in intensity is not at the slit center; but it is slightly shifted towards the outer wall.

The energy of ω_1 is red-shifted from 0.52 eV to 0.49 eV in the center of the slit. Near the inner wall of the first slit, is rises again to 0.5 eV. Inside the second slit, there is a slight red-shift from 0.5 eV to 0.48 eV.

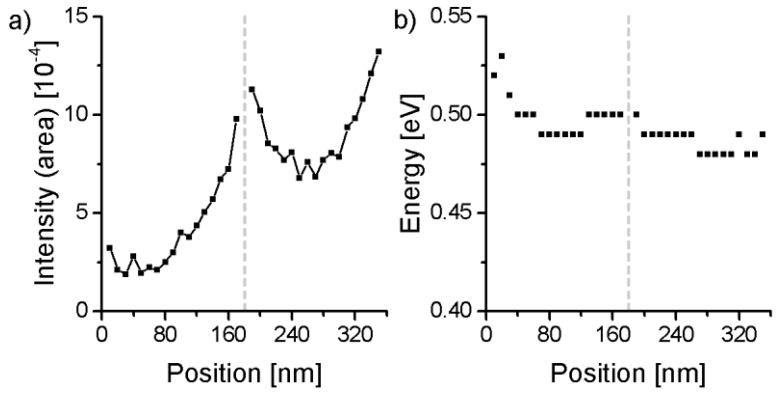

Figure 4.5.4 a) Intensity and b) energy profiles as a function of the distance to the outer wall of slit 1 extracted from the measurements inside a four-slit array. The grey dashed lines mark the metal bars separating the two slits.

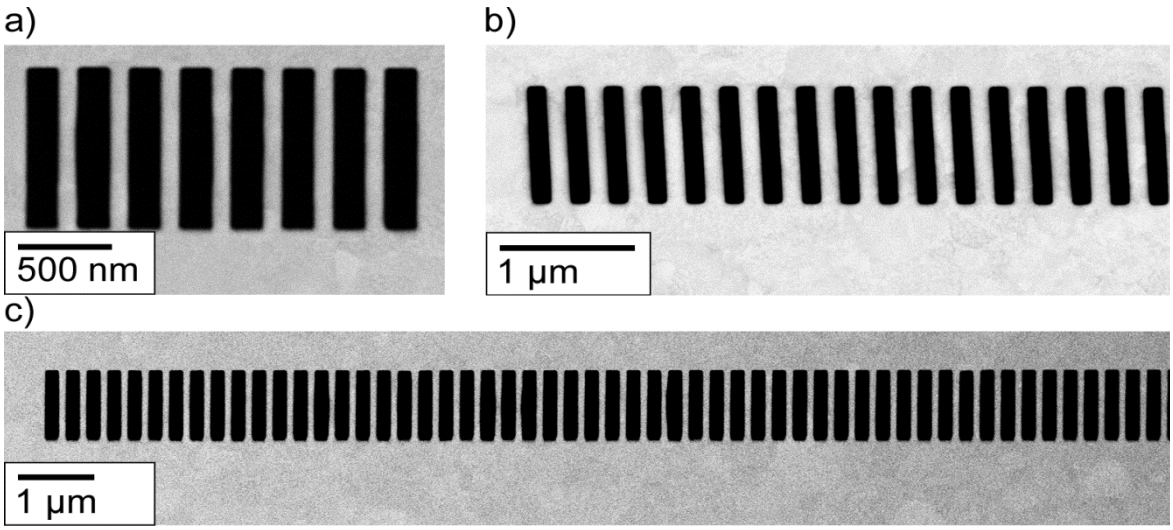

Figure 4.5.5 HAADF STEM images of arrays consisting of a) 8, b) 20, and c) 60 slits with L = 960 nm and d = 100 nm.

For the larger arrays consisting of 8, 20, and 60 slits, individual spectra will not be shown. Only the extracted intensity and energy profiles will be presented. Figure 4.5.5 shows HAADF STEM images of the three large arrays. The corresponding experimental data is presented in Figure 4.5.6. The eight-slit array was measured completely across all slits and the intensity and energy profiles are presented in Figure 4.5.6a,b. Only half of the twenty-slit array was analyzed (Figure 4.5.6c,d) and only selected slits inside the largest array consisting of sixty slits (Figure 4.5.6e,f).

Inside the eight-slit array, the intensity profile resemble that of the smaller arrays. Generally, the intensity in the inner slits shows a ‘U’-shaped profile. To discuss the intensity differences in those

slits, the minimum of the ‘U’-shaped profile is used and is referred to as the central intensity. The central intensity steadily increases in slits one to three and reaches a maximum inside slit 3. In slit 4, the central intensity is slightly reduced and is similar to the second slit. The behavior of slits five to eight appears to be symmetric with respect to the first half of the array. However, the intensity near the outer wall in slit eight is higher than the intensity at the respective wall inside the first slit. This is most likely an effect of a slight deviation of the beam distance to the slit wall, which will result in significant intensity differences due to the steep slope of enhancement in the near-field region. To circumvent this effect, the central intensity is used to evaluate the behavior inside the slit array.

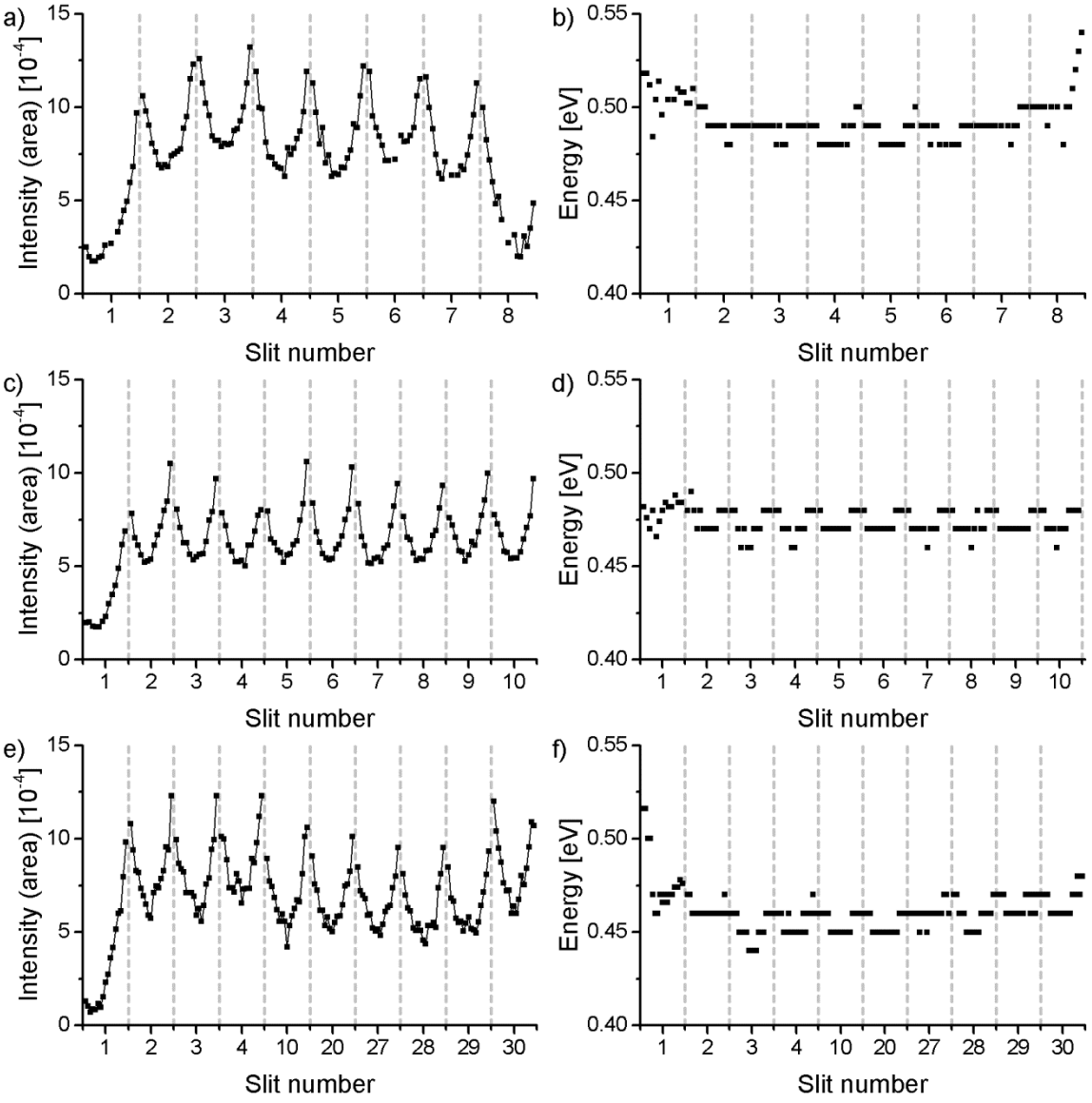

Figure 4.5.6 a), c), e) Intensity and b), d), f) energy profiles of the fundamental mode as a function of the slit number inside slit arrays consisting eight (a,b), twenty (c,d), and sixty (e,f) slits with L = 960 nm and d = 100 nm. Only half of the array and selected slits were analyzed inside the twenty and sixty-slit arrays. Grey dashed lines indicate the metal bars.

The energy of ω_1 is 0.52 eV or 0.54 eV close to the outer walls. The value of 0.54 eV inside the slit number eight may also be related to imperfect beam positioning. The energy drops in the center of the first slit and rises again near the inner wall inside the two outer slits. Inside the array, the energy is varying between 0.49 and 0.48 eV. However, the experimental energy resolution is 0.01 eV at best and therefore this observation is not significant.

The intensity profile in the twenty-slit array presented in Figure 4.5.6c has a course similar to the first slits inside the other arrays. In the inner slits of the array, the central intensity does not alter at all. The intensity is always slightly higher near the right wall inside each slit, which is probably caused by specimen drift towards the left during the measurement series. The beam may have been positioned at a smaller distance to the wall then on the left side. Inside the first slit, the energy is slightly higher compared to the rest of the array with a mean value of about 0.49 eV. In slits 2 to 10, the energy ranges from 0.47 to 0.48 eV with a few outliers at 0.46 eV. The energy is always slightly higher near the wall than in the slit center. However, it should be noted that the slit width in the twenty-slit array is only 145 nm and therefore significantly lower compared to the other arrays with slit widths of 180 nm.

In the sixty-slit array, the intensity profile in the first slit is again similar to the other arrays although the intensity at the outer wall is significantly lower. Slits two to four show the same central intensity. Inside slit number 10, the central intensity is reduced and remains at this level up to slit 29 although this is only suggested because measurements were not performed in slits 11-19 and 21-26. A slight intensity increase is observed for slit number 30. The energy profile is similar to the smaller arrays with a significant red-shift inside the first slit. Inside the array, the energy is also always slightly lower in the center of the slit. However, in contrast to the smaller arrays, the lowest observed energy has dropped to 0.44 eV.

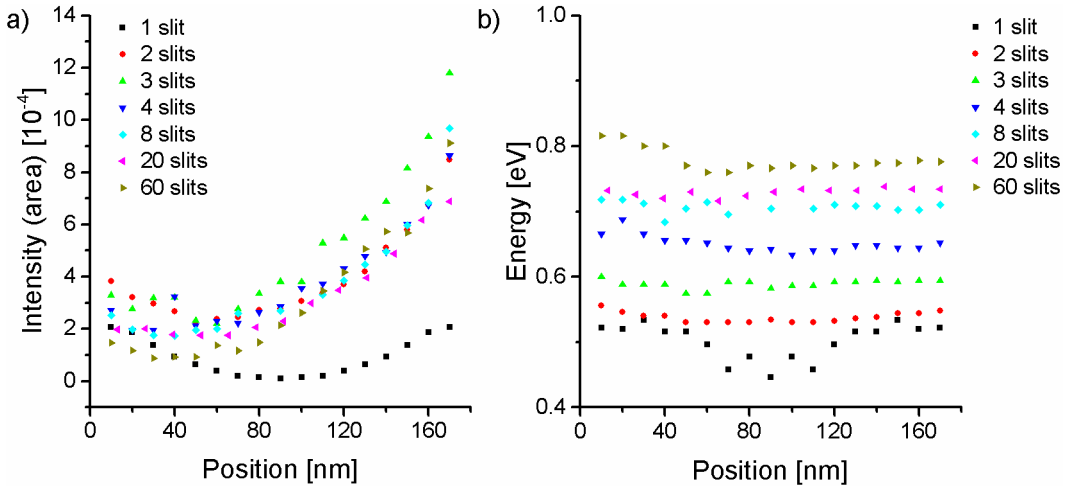

Figure 4.5.7 a) Intensity and b) energy profiles inside the first slit of various arrays with L = 960 nm and d = 100 nm. For presentation purposes, the energy profiles are shifted by 0.05 eV with respect to each other.

To compare the slit arrays, the intensity and energy profiles of the first slit are summarized in Figure 4.5.7. A single slit is also included. The basic intensity variation observable in Figure 4.5.7a for the various arrays is similar: The intensity is low at the outer wall and decreases for distances of about 50 nm to the wall, followed by an enhancement close to the inner wall. There are, however, small variations depending on the exact array size. The intensity at the outer wall is

highest for a double slit and decreases with the number of slits in an array. All intensities are normalized to the ZLP. In the largest array consisting of sixty slits, the intensity is even lower than the one inside the single slit. Close to the inner wall, the intensity variations are different than at the outer wall. In descending order, the intensity is distributed as follows: 3 slits, 8 slits, 60 slits, 4 slits, 2 slits and 20 slits. This suggests that the intensity at the inner wall of slit 1 is not directly correlated with the array size. Table 4.5.1 summarizes the obtained intensity values. The intensity minimum in slit 1 was also extracted. It does not drop as low as in the single slit in any of the arrays. With the exception of the sixty-slit array, all intensity minima of the arrays are comparable.

	Outer wall	Minimum	Inner wall
Single slit	$2.06 \cdot 10^{-4}$	$0.11 \cdot 10^{-4}$	$2.06 \cdot 10^{-4}$
2 slits	$3.83 \cdot 10^{-4}$	$2.17 \cdot 10^{-4}$	$8.48 \cdot 10^{-4}$
3 slits	$3.30 \cdot 10^{-4}$	$2.20 \cdot 10^{-4}$	$11.80 \cdot 10^{-4}$
4 slits	$2.73 \cdot 10^{-4}$	$1.96 \cdot 10^{-4}$	$8.65 \cdot 10^{-4}$
8 slits	$2.52 \cdot 10^{-4}$	$1.75 \cdot 10^{-4}$	$9.69 \cdot 10^{-4}$
20 slits	$2.27 \cdot 10^{-4}$	$1.99 \cdot 10^{-4}$	$8.39 \cdot 10^{-4}$
60 slits	$1.47 \cdot 10^{-4}$	$0.88 \cdot 10^{-4}$	$9.12 \cdot 10^{-4}$

Table 4.5.1 Intensity of the fundamental cavity mode inside the first slit in arrays with L = 960 nm and d = 100 nm. The assumed error in intensity is $0.5 \cdot 10^{-4}$.

The energy profiles shown in Figure 4.5.7b are shifted by 0.05 eV with respect to each other to improve clarity. In the single slit, the energy is reduced in the center of the slit. For arrays consisting of 2 to 4 slits the energy profiles appear almost constant although there is still a small red-shift near the center of the slit. This is also the case for 8 and 20 slits but there, the minimum in energy is slightly shifted towards the outer wall. Inside the first slit of the sixty-slit array, the energy decreases for distances up to 70 nm and then remains at this level towards the inner wall. The exact energies at both walls and the minimum in energy inside the first slits are presented in Table 4.5.2. The energy near the outer wall is identical to the single slit or slightly reduced. At the inner wall, the fundamental cavity mode energy is red-shifted with respect to the outer wall (and the single slit) with the exception of the twenty-slit array. The energy differences between the outer and inner walls are small and, with respect to the energy error of 0.01 eV, maybe insignificant. The minimum energy in the arrays decreases slightly with the array size in comparison to the single-slit value.

	Outer wall	Minimum	Inner wall
Single slit	0.52 eV	0.45 eV	0.52 eV
2 slits	0.51 eV	0.48 eV	0.50 eV
3 slits	0.50 eV	0.48 eV	0.49 eV
4 slits	0.52 eV	0.48 eV	0.50 eV
8 slits	0.52 eV	0.48 eV	0.51 eV
20 slits	0.48 eV	0.47 eV	0.49 eV
60 slits	0.52 eV	0.46 eV	0.48 eV

Table 4.5.2 Energy of the fundamental cavity mode inside the first slit in arrays with L = 960 nm and d = 100 nm. The error in energy is 0.01 eV for all measurements.

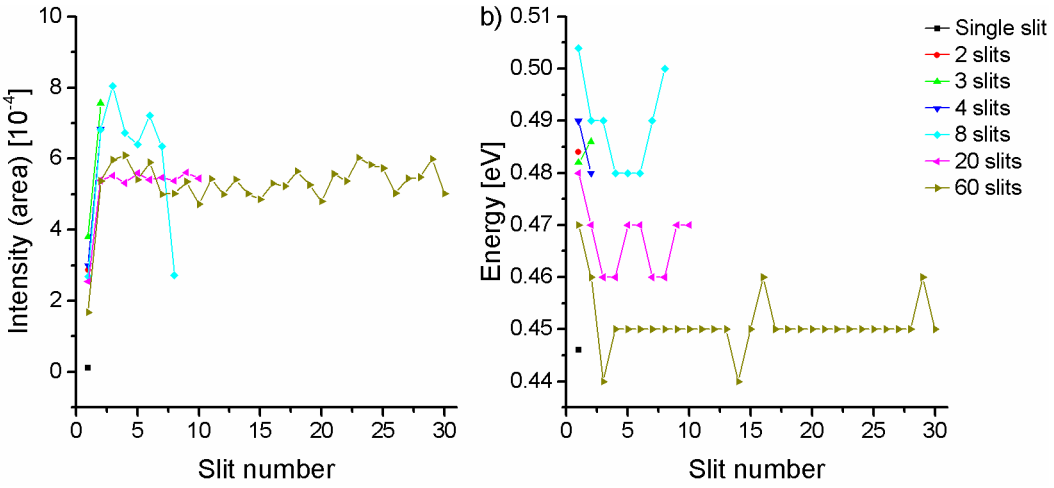

Figure 4.5.8 a) Intensity and b) energy of the fundamental mode measured at the center of the individual slits. Assumed errors: a) intensity $0.5 \cdot 10^{-4}$ and b) energy 0.01 eV.

Figure 4.5.8 shows the intensity and energy of the fundamental mode measured at the center of each slit. Here, the full half of the sixty-slit array was analyzed and is included. It should also be noted that the whole array was only measured in the case of eight slits. The single slit shows the lowest intensity in the center. Regarding the arrays, the sixty-slit system has low intensity in the first slit whereas the highest intensity is observed for the three-slit system. The remaining arrays have similar intensity inside the first slit. The eight-slit array shows the highest intensity in this data set in the third slit. Inside slits 4 and 5 of the same array, the intensity shows a small dip and increases again in the 6th slit. Towards the other end of the array, the intensity drops to the level of slit 1. The overall intensity profile is symmetric. The twenty-slit array does not show significant intensity variation inside the array apart from the initial enhancement in the first slit. The largest array shows high intensity for slits 3 and 4. For the rest of the array, the intensity distribution is quite noisy. However, when the center of the array is approached, the fundamental seems to rise

slightly in intensity. Figure 4.5.8b plots the energy variation across the slit arrays. Common to all slit arrays with more than 4 slits is the red-shift in the first 3-4 slits of the array. In the central slits of the arrays, the energy does not change significantly. However, the red-shift increases with the array size.

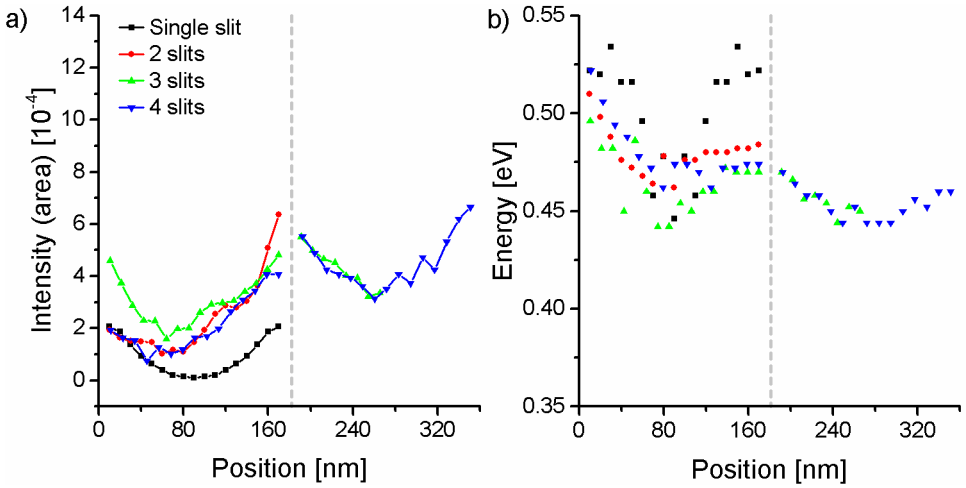

Figure 4.5.9 a) Intensity and b) energy profiles in the first two slits (if applicable) of arrays with up to four slits and an inter-slit distance of d = 270 nm. The grey dashed line indicates the metal bar.

Three- and four-slit arrays were also prepared with larger inter-slit distances of d = 270 nm and d = 680 nm. The intensities and energies of the fundamental mode for d = 270 nm are shown in Figure 4.5.9, including the single slit and a double-slit system with the same inter-slit distance. Except for the green curve (3-slit array), all data sets have similar intensity close to the outer wall. Close to the inner wall, an enhancement is observed for all arrays and the highest intensity occurs for the double-slit system. The 3-slit and 4-slit arrays have similar intensity in slit 2 and show a decrease in intensity close to the slit center. Close to the second (central) metal bar of the four-slit array, the intensity increases even further and reaches a higher value than in the vicinity of the first bar. The extracted intensity values inside the first slit are summarized in Table 4.5.3.

	Outer wall	Minimum	Inner wall
Single slit	$2.06 \cdot 10^{-4}$	$0.11 \cdot 10^{-4}$	$2.06 \cdot 10^{-4}$
2 slits	$1.94 \cdot 10^{-4}$	$1.03 \cdot 10^{-4}$	$6.37 \cdot 10^{-4}$
3 slits	$4.60 \cdot 10^{-4}$	$1.60 \cdot 10^{-4}$	$4.82 \cdot 10^{-4}$
4 slits	$1.93 \cdot 10^{-4}$	$0.76 \cdot 10^{-4}$	$4.07 \cdot 10^{-4}$

Table 4.5.3 Intensity of the fundamental cavity mode inside the first slit in arrays with L = 960 nm and d = 270 nm. Error: $0.5 \cdot 10^{-4}$

Common for all data sets is the red-shift of the fundamental mode for increasing distances to the outer wall (Figure 4.5.9b). This red-shift is less pronounced for arrays consisting of 2 and 4 slits

whereas it is identical for the single slit and the 3-slit array. Upon approaching the inner wall, a slight rise in intensity is observed for the arrays although the final energy remains significantly lower than the single slit energy. Inside the second slit, a red-shift is observed near the center of the slit and the minimum in energy is similar to the first slit.

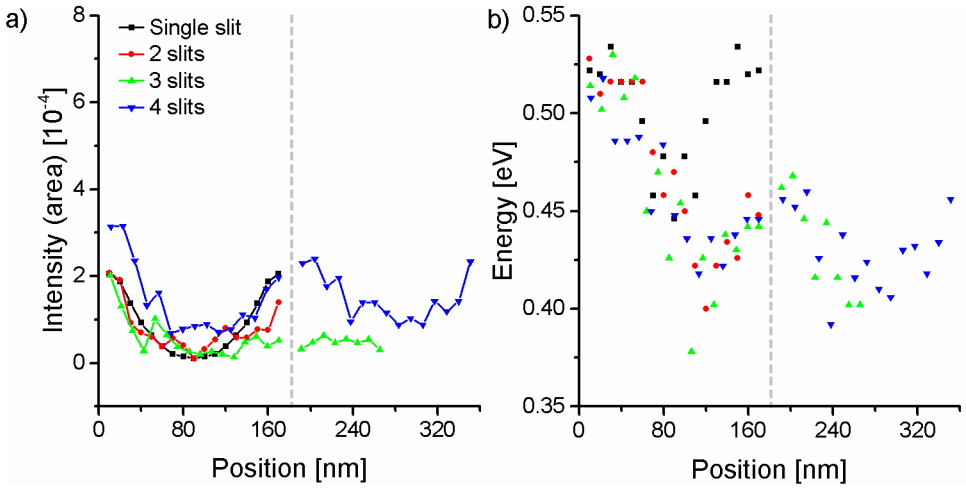

Figure 4.5.10 a) Intensity and b) energy profiles in the first two slits (if applicable) of arrays with up to four slits and d = 680 nm. The grey dashed line indicates the metal bar.

Figure 4.5.10 shows the data for the inter-slit distance d = 680 nm and arrays consisting of 1-4 slits. The intensity in the first slit shows a U-shaped profile with a higher intensity for the four-slit array at the outer wall compared to the other arrays. However, there are striking differences directly at the inner wall compared to all previous slit systems because the intensity is not enhanced at the inner wall. This is even more clearly visualized by the extracted intensity values inside the first slit which are given in Table 4.5.4.

	Outer wall	Minimum	Inner wall
Single slit	$2.06 \cdot 10^{-4}$	$0.11 \cdot 10^{-4}$	$2.06 \cdot 10^{-4}$
2 slits	$2.08 \cdot 10^{-4}$	$0.10 \cdot 10^{-4}$	$1.40 \cdot 10^{-4}$
3 slits	$2.01 \cdot 10^{-4}$	$0.14 \cdot 10^{-4}$	$0.52 \cdot 10^{-4}$
4 slits	$3.14 \cdot 10^{-4}$	$0.68 \cdot 10^{-4}$	$1.97 \cdot 10^{-4}$

Table 4.5.4 Intensity of the fundamental cavity mode inside the first slit in arrays with L = 960 nm and d = 680 nm. Error: $0.5 \cdot 10^{-4}$.

In the second slit, the intensity of the three-slit array is almost unchanged and remains at a very low level while the four-slit array it shows a slight intensity dip near the slit center.

The energy profiles in Figure 4.5.10b are in general noisy due to the low intensity of the fundamental mode. However, the following trend can be recognized: All arrays and the single slit have similar fundamental energies close to the outer wall. A red-shift occurs towards the slit

center, which it appears to be slightly displaced towards the inner wall for the arrays with multiple slits. The energy rises again towards the metal bar, although it remains significantly lower in comparison to the single slit. Inside the second slit, the fundamental is shifting to lower energy and is comparable to the minimum in energy inside the first slit.

In addition to the comparison of arrays with varying slit number and identical inter-slit distance, it is instructional to compare arrays with the same slit number and different inter-slit distances. The integrated intensity profiles extracted from arrays consisting of three slits with varying d are shown in Figure 4.5.11a. Qualitatively, the behavior is similar for the three data sets for increasing distances from the outer wall. Only the intensity at the outer wall is different. The red curve (d = 270 nm) has higher intensity compared to the black curve (d = 100 nm). The overall intensity for the green curve (d = 680) is even lower. However, there are more differences close to the inner wall: in contrast to all other slit arrays the intensity for d = 680 nm stays at a low level. Inside the second slit, the intensity profiles are almost mirrored compared to their counterparts in the first slit. Only for the shortest inter-slit distance, the intensity is not decreased to the level of the first slit. The energy shifts presented in Figure 4.5.11b are quite noisy for the two larger inter-slit distances. However, the following trends can be observed: the energy is red-shifted in the center of the slits and this red-shift increases with increasing inter-slit distance. Moreover, the energy minimum in the first slit shifts. For the intermediate slit distance, it is close to the slit center. It is shifted slightly towards the outer (inner) wall for the small (large) inter-slit distance. The energy profiles inside the second slit appear to be mirrored with respect to the metal bar between the slits.

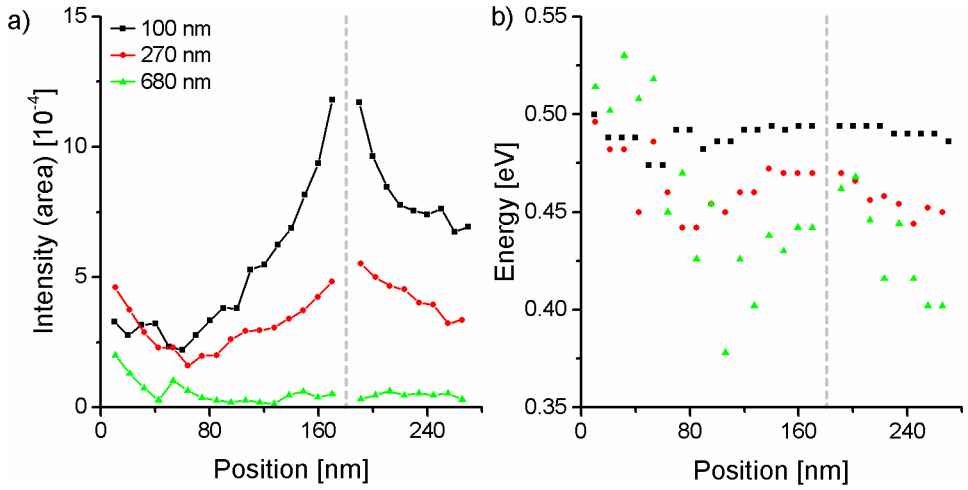

Figure 4.5.11 a) Intensity and b) energy profiles of the fundamental mode in arrays consisting of three slits with varying inter slit distance as a function of the distance to the outer wall. The grey dashed line indicates the metal bar position.

Analogous graphs for the four-slit arrays are shown in Figure 4.5.12. Here the intensity at the outer wall is smallest for the intermediate slit distance whereas the other two data sets have similar intensity. Increasing the distance from the outer wall leads to a dip in intensity until enhancement is observed near the inner wall. The enhancement is strongest for the smallest inter-slit distance. Inside the second slit, all intensities drop towards the slit center and are enhanced again near the second metal bar. The energy of the fundamental mode shown in Figure 4.5.12b shows the basic behavior of all arrays, i.e., a red-shift towards the center of the first slit and a slight increase close the inner wall of the first slit. The red-shift is increased for larger inter-slit distances. In the second slit, similar behavior is observed but with a more pronounced red-shift compared to the first slit.

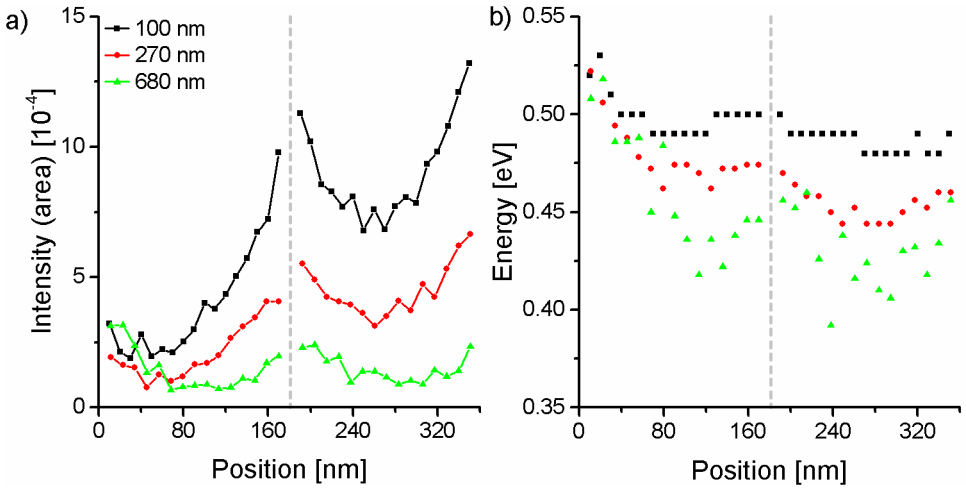

Figure 4.5.12 a) Intensity and b) energy profiles of the fundamental mode in arrays consisting of four slits with varying inter slit distance. The grey dashed line indicates the metal bar position.

4.5.2 Discussion

The basic behavior of the fundamental cavity mode intensity and energy shows the same pattern in all slit arrays. Inside the first slit, the intensity starts at a low level at the outer wall, decreases with increasing distance to the outer wall and rises again towards the inner wall. As far as the energy profile is concerned, a decrease in energy occurs towards the center of the array and a slight rise upon approaching the inner wall but not as high as on the outer wall. The detailed modulation of the intensity profile depends on the parameters of the array.

Figure 4.5.7a shows the intensity profiles inside the first slit of arrays with varying slit number and a fixed inter-slit distance of 100 nm. The basic behavior described above is directly observable. For a better understanding of the differences between the single slit and the arrays, the single slit intensity profile was subtracted and the results are shown in Figure 4.5.13a.

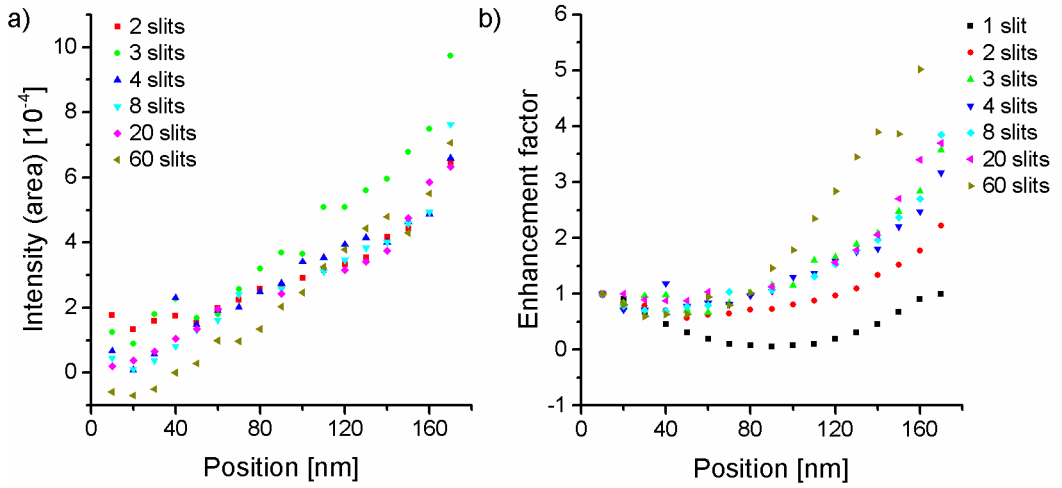

Figure 4.5.13 a) Intensity of the fundamental cavity mode corrected by subtracting the intensity obtained within a single slit as a function of the distance to the outer slit wall. b) Enhancement factor of the intensity calculated by normalizing the intensity profile to the intensity at the outer wall. All data sets refer to slit systems with d = 100 nm.

The intensity at the outer wall is directly related to the number of slits, i.e. it decreases with the slit number. For an array of sixty slits, the intensity is even reduced compared to the single slit indicating that the slit number affects the intensity even at the outer wall. This is unexpected as the coupling between slits is mediated by SPPs travelling across the metal bars connecting the slits.[103] Therefore the outer wall is expected to show a similar intensity as in the single slit. Hence, the clear effect of the slit number in an array on the outer wall intensity suggests a coupling component across the slits themselves. A hint to such a coupling component was also observed for varying the inter-slit distances (cf. Figure 4.4.10a) as the energy position of the fundamental was slightly shifted to lower energy compared to the single slit. Energy variations at the outer wall are also observed in arrays with varying slit number. Two- and three-slit arrays show a significantly reduced energy, whereas the other arrays have an energy only very slightly lower compared to the single slit. There is no clear correlation of the slit number with the resulting energy at the outer wall.

Across the first slit, a steady, almost linear intensity enhancement is observed for all array sizes (Figure 4.5.13a). However the number of slits inside an array is no longer directly related to the resulting intensity. At the inner wall, the three-slit system shows a significantly higher intensity compared to all other array sizes. But in relation to the general intensity enhancement, the effect of the exact number of slits is small. Therefore, next-neighbor coupling across the first metal bar of the array seems to be the main mechanism of enhancement. The data can also be compared to each other differently as show in Figure 4.5.13b: here, the intensity profile within each data set was normalized to its intensity close to the outer wall. In this presentation, the intensity enhancement is

related to the number of slits within an array. The single slit shows no enhancement at all between both slit walls, as expected from the symmetric profile. For the slit arrays, the enhancement factor between the inner and outer wall of the first slit increases from 2.2 up to 5 for the sixty-slit array. However this dependence on the number of slits may also be only related to the fact that normalization was performed with respect to the intensity near the outer wall, where the intensity is directly related to the number of slits. In that way, Figure 4.5.13a shows the basic enhancement due to next-neighbor coupling whereas Figure 4.5.13b shows the effects of the slit number in a more pronounced way.

Within the second and following slits inside an array, the slit intensity profiles are "U"-shaped with intensity differences at the walls of the individual slits (cf. Figure 4.5.6a,c,e). However, these intensity differences observed at the walls seem to be related to the experimental conditions. Particularly in the arrays consisting of twenty and sixty slits, the intensity at the right wall inside slits is higher than on the left wall. This is attributed to the steep slope of the intensity profile close to the walls (due to near-field hybridization with SPP[14]), where small deviations in the beam position may lead to such intensity differences. Due to the systematic intensity variation, drift may be identified as the reason. If, during measurement, the specimen slowly drifts towards the left (with respect to the array direction), the measurements on the right slit wall will have a reduced distance to the wall compared to the left wall, even if the beam position was at identical distance on both walls. This explanation is confirmed by the eight-slit array (Figure 4.5.6a) as the intensity differences only occur in slits 2 and 3 whereas slits 6 and 7 do not show them. If they were related to a physical effect in the arrays, the intensity differences should be symmetric with respect to the array center. Another possibility could be the exact shape of the milled slit. As described in section 3.5.2, the focused ion beam is scanned across the slits in a distinctive manner, e.g. left to right and up to down. Ideally, this should not result in a different milling result, however it cannot be excluded. Local changes in the texture of the Au film can also result in differences of the measured intensities. However, due to the systematic variation observed in the twenty- and sixty-slit arrays, this explanation seems very unlikely.

To evaluate the intensity of the fundamental mode in the individual slits within an array without strong effects of drift and beam positioning, the intensity at the center of the slit (i.e. the center of the "U" shape) is used as the point of reference as shown in Figure 4.5.8a. Focusing briefly on the second slit within the arrays, the highest intensity is observed for the three-slit system, the four- and eight-slit systems follow with a slightly reduced intensity. The two large arrays have significantly lower intensity. A possible explanation for the high intensity in the three-slit array could be related to edge effects of the arrays and is given in the following. Looking at the eight slit array, the intensity profile across the whole array shows a rise in intensity inside the first three slits and a dip in intensity in the array center. A similar build-up in intensity is observed for the sixty-

slit array over the first five slits: The intensity reaches its highest point in slits three and four, followed by a dip in the fifth slit indicating that the edge effect spreads over the first five slits of an array. If the slit array consists of less than ten slits (keeping both edges in mind), the initial intensity build-ups on both edges of the array are superimposed. In the eight-slit array, this superimposition is still "resolvable" and a dip in intensity in the center of the array is observed. However, the superposition leads to an increase in intensity across the whole array. Similar edge effects were predicted by Fernandez-Dominguez et al.[105] In their simulations, the per-slit transmittance in arrays of various sizes was calculated and they found edge effects across the first ~ twenty slits for arrays consisting of 100 to 300 slits. An array size of fifty slits has shown the expected enhancement when the edge effects on both array ends overlap. However, these simulations cannot be directly compared to our experiments because we evaluate a different quantity, namely the intensity of the fundamental cavity mode. It may be related to the per-slit transmission, but not necessarily. Nevertheless it confirms that edge effects may affect the experimental results in such nanostructures to a certain degree.

In the three-slit array on the other hand, the intensity build-up on both edges of the array overlap in such a manner, that the intensity inside the central slit is strongly enhanced. But the array is too small for the full extent of this edge-related intensity build-up. Similar enhancement effects in arrays of nanoholes in a Au-film were reported by Alaverdyan et al.[87] They have observed a steady build-up in scattering intensity per hole with increasing hole numbers from 1 to 3. In larger arrays consisting of 5 and 18 holes, a slight intensity drop compared to the three-hole array is observed. This could also be related to some sort of edge effect. In addition to this edge-effect, another approach to explain these intensity differences is considered in the following.

	d = 100 nm	d = 270 nm	d = 680 nm
Single slit	180 nm	180 nm	180 nm
2 slits	460 nm	630 nm	1040 nm
3 slits	740 nm	1080 nm	1900 nm
4 slits	1020 nm	1530 nm	2760 nm
8 slits	2140 nm	3330 nm	6200 nm

Table 4.5.5 Lengths of the complete arrays consisting of varying number of slits and varying inter-slit distance.

Table 4.5.5 shows the complete lengths of various arrays with different inter-slit distances. Interestingly, the length of the four- and eight-slit arrays with an inter-slit distance of 100 nm are in the same order of magnitude as the half and full wavelength of the fundamental mode. In section 4.4, the ratio of the inter-slit distance and the fundamental wavelength was identified as the main factor responsible for the observed mode splitting. Therefore, the possibility exists that there are

effects on the fundamental mode if the array length is related to the wavelength of ω_1. It is also worth noting that the calculated array lengths seem to better fit the measured, elongated wavelengths (the fundamental wavelength should be elongated by 10 to 15%, see section 4.3) than the nominal fundamental wavelength of $\lambda_1 = 2L = 1920$ nm.

In the case of the eight-slit array, the length of the array is almost identical to the expected elongated wavelength of the fundamental and coincidentally shows the highest intensity measured for any array (cf. Figure 4.5.8a). The overall length of the four-slit array on the other hand corresponds to $\lambda_1/2$ and exhibits slightly smaller intensities than what would be expected from the influence of the edge effects. Moreover, in the case of the sixty-slit array, there may be intensity variations inside the array with a period of about 7-8 slits which is similar to the fundamental wavelength. The array sizes with different inter-slit distances are also included in Table 4.5.5. The interesting case is the three-slit array with d = 270 nm as its size corresponds to $\sim \lambda_1/2$. Figure 4.5.9 shows that this array behaves differently compared to expected general behavior inside the first slit. The fundamental is much more pronounced at the outer wall compared to the single slit and the other arrays. However, close to the inner wall, its intensity is in the same range as for the other arrays. But the effect of the array size for d = 100 nm was observed for the intensity within the array and not close to the outer wall. Therefore, the high intensity at the outer wall could but does not have to be related to the array size. Another point to consider is the different coupling due to the larger distance between slits. According to section 4.4, a decrease in intensity is observed which may also affect the results within an array of slits. This effect is much more pronounced for the arrays with the largest inter-slit distances which do not show any enhancement for the fundamental mode. However, as seen in Figure 4.5.10, there are still effects. In the case of four slits, the intensity is significantly higher close to the outer wall as for the other arrays which show intensity similar to the single slit. At the inner wall on the other hand, the intensity inside the four slit array is similar to the single slit, whereas the other two arrays show a diminished intensity. In the case of three slits, there is almost no intensity variation for the right half of the array; rather it stays as low as in the center of the first slit. Also inside the second slit, the intensity remains as low. According to Table 4.5.5, the size of the three-slit array with d = 680 nm is 1900 nm which is close to λ_1. In summary, the effect of the array size does not seem to be consistent for different inter-slit distances. For d = 100 nm, there seems to be some kind of enhancement or decrease if the array size is close to λ_1 or $\lambda_1/2$. For d = 270 nm, enhancement (at the outer wall) is observed if the array size is $\sim\lambda_1/2$. However for d = 680 nm, a decrease in intensity is observed for an array size similar to $\lambda_1/2$.

In conclusion, if there are effects related of the ratio of the overall array size and λ_1, they are not consistent for the different inter-slit distances. As already stated above, this may be related to the

different coupling related to d/λ_1. The further analysis of this effect is also limited by the limited array sizes in the case of the larger inter-slit distances.

The energy of the fundamental cavity mode is also affected by the parameters of the arrays. Before going into detail, the basic behavior of the energy profile will be discussed. According to Table 4.5.2, inside a single slit, the energy close to the wall is 0.52 eV and experiences a red-shift to 0.45 eV in the slit center. In arrays with an inter-slit distance of d = 100 nm, the basic behavior with a red-shift towards the center of the slit is still observed although the red-shift is much less pronounced. This also stems from a lower energy at the outer wall (at least for arrays of consisting of two, three, and twenty slits). The energy slightly rises towards the inner wall but always remains at a value lower than at the outer wall. Inside the second slit (cf. Figure 4.5.2, Figure 4.5.4, and Figure 4.5.6), the energy close to both walls is identical to the energy at the inner wall in the first slit. The energy is red-shifted towards the slit center and increases again towards the second metal bar. The behavior in the following slits in larger arrays is similar, although the energy level may change slightly. To evaluate these energy shifts within arrays, the energy at the center of the individual slits is taken as an indicator. According to Figure 4.5.8b, the energy shifts continuously towards lower values in the first 3-4 slits of the larger arrays. This is the same scale as for the intensity build-up due to the aforementioned edge effects and may therefore be related to such an effect. After this initial red-shift, the energy does not change significantly inside the array. There are shifts of 0.01 eV visible but these are related to the crude data sampling and the error margin of the energy measurement. In contrast to the first slits, inside the larger arrays, the exact peak positions were not determined by fitting a Gaussian to the fundamental peak; rather they were directly measured in the data. Figure 4.5.8 also shows an increasing red-shift of the energy inside the larger arrays for increasing array sizes. To assess this effect, the lowest energy obtained in a given data set for an array was determined and is shown in Table 4.5.6.

	d = 100 nm	d = 270 nm	d = 680 nm
Single slit	0.45 eV	0.45 eV	0.45 eV
2 slits	0.48 eV	0.46 eV	0.40 eV
3 slits	0.48 eV	0.44 eV	0.40 eV
4 slits	0.48 eV	0.44 eV	0.39 eV
8 slits	0.48 eV	-	-
20 slits	0.46 eV	-	-
60 slits	0.44 eV	-	-

Table 4.5.6 Lowest energy of the fundamental cavity mode measured in arrays of different sizes and inter-slit distances. Error: 0.01 eV.

The slit arrays with fewer than twenty slits all show a similar minimum energy that is higher than inside a single slit. For the larger arrays, however, the energy minimum is further red-shifted and inside the sixty-slit array, the energy is even slightly smaller than for the single slit. The effect of an increasing red-shift of the minimum energy with increasing array size also holds for arrays with larger inter-slit distances. The general shift towards lower energy with increasing inter-slit distance is linked to the different coupling behavior between slits as already discussed in section 4.4.

5 Summary and Outlook

In this work, the hybridization of surface plasmon polaritons (SPPs) and resonant cavity modes in artificial nanostructures were studied by scanning transmission electron microscopy (STEM) in conjunction with electron energy loss spectroscopy (EELS). The investigated nanostructures are rectangular slits in a 200 nm thin Au film. The slits with a standard size of 180 x 960 nm were milled in the metal film by a focused Ga^+-ion beam system. Single slits and multiple-slit systems were analyzed. The effects of varying the slit length, the inter-slit distance and the slit number were studied systematically. The highly focused electron beam in the transmission electron microscope excites SPPs at the slit walls which hybridize with cavity modes that are dictated by the long slit direction. The fundamental cavity modes have low energies < 1 eV and low intensity. The investigation of cavity-mode-related signals in EELS spectra is challenging due to their close proximity to the intense tail of the zero-loss peak. Hence, sophisticated experimental and data processing methods have to be employed to allow the precise evaluation of the low-energy signals. The so-called 'binned gain-averaging' acquisition method is highly beneficial for the data quality by increasing the signal-to-noise ratio significantly and slightly improving the experimental energy resolution. This is accomplished by shifting the spectrum's position on the CCD camera in the spectrometer deliberately which reduces the noise attributed to gain variation with high efficiency. After the correction of the applied energy shifts and summation by self-written scripts, the experimental data is spectrally sharpened by applying the Richardson-Lucy (RL) algorithm adapted to EELS data. The RL algorithm deconvolutes the point-spread function of the employed spectrometer and thereby increases the energy resolution significantly. Using these techniques, the energy resolution of 0.07 eV was achieved in this work. The experimental results are complemented by numerical simulations based on the Discontinous Galerkin Time Domain method adapted to EELS spectra.

In a single slit, the electric field of the electron beam positioned in the slit excites SPPs on the slit walls which excite cavity modes. The observed fundamental cavity mode is enhanced in the near-field region close to the slit walls which shows the hybridization with the evanescent field associated with the SPPs supported on the slits walls. The intensity distributions of the excited higher order modes (up to n = 3) show Fabry-Perot-like behavior.

In a double-slit system, the single slit mode couples with the neighboring slit by SPPs propagating on the metal bar which separates the two slits. For small metal bar widths d, the coupling results in a strong enhancement and slight red-shift of the cavity modes close to inner slit wall. At the outer wall, however, the cavity modes are not affected by the neighboring slit and behave similar to the cavity modes in a single slit. The strong coupling facilitates data processing and the experimental results have higher accuracy in double- and multiple-slit systems. Double-slit systems with small

metal bar width d and varying slit length L show an increasing red-shift for increasing L. The energy of the fundamental cavity mode is directly proportional to 1/L. The red-shift of the fundamental cavity mode energy leads to a smaller spectral separation of the higher harmonics and, hence, higher mode orders up to n = 11 can be excited. The wavelength of the cavity modes can be derived from the spatial variation of the energy-loss intensity of the higher harmonics and, combined with the measured energies, the dispersion relation of the hybridized cavity modes was derived. The measured dispersion relation is similar to the expected SPP dispersion relation and confirms the hybridization of cavity modes and SPPs.

To study the coupling behavior in double-slit systems, the metal bar width d was systematically varied and its effect on the intensity and energy of the fundamental cavity mode was analyzed in detail. In the absence of coupling, the cavity modes in the two slits of the double-slit system would be identical to the single slit and thus degenerate in energy. The degeneracy is lifted by hybridization into a red-shifted and a blue-shifted mode with respect to cavity-mode energy in the single slit. These two modes correspond to anti-symmetric and symmetric coupling of the cavity modes in the two slits. The coupling only depends on the ratio of the metal bar width d and the wavelength λ (given by 2L) of the fundamental cavity mode.

For $d/\lambda < 0.5$, the red-shifted mode is dominant and shifts towards lower energy. It decreases strongly in intensity with increasing d/λ until it almost vanishes. The strong enhancement of the anti-symmetric mode (compared to the intensity of the fundamental mode in a single slit) for small d/λ is related to interaction of SPPs supported on either wall of the metal bar. For $d/\lambda > 0.5$, the blue-shifted mode is dominant. It shifts towards lower energy and increases in intensity until its intensity and energy correspond to the single-slit case at $d/\lambda = 1$. At $d/\lambda = 0.5$, the two modes are equally excited.

Increasing the number of slits only has minor effects on the coupling behavior. At the outer wall of the first slit in an array, the cavity modes are not affected by the neighboring slits at all. Close to the inner wall of the first slit, the behavior is similar to the double-slit systems. Inside the other slits of an array, the cavity mode intensity is reduced at the slit center and is symmetric with respect to the two walls. The coupling is therefore mainly based on next-neighbor coupling. Minor intensity variations of the fundamental cavity mode occur for various array sizes with up to 60 slits. These intensity modulations seem to depend on the ratio of the array length and the wavelength of the fundamental cavity mode which can be considered as an indication of a collective excitation of the array as a whole.

The above explanation of the coupling behavior is solely based on phenomenological models and a deeper understanding of the underlying physics is still needed. Investigating the coupling regime for $d/\lambda > 1$ will be helpful in this respect. Such inter-slit distances may be too large for effective coupling between the slits and thus a behavior similar to a single slit could result. On the other

hand there is also the possibility of another mode splitting at $d/\lambda = 1.5$. It will be also instructive to study the light-optical properties of these structures by catholuminescence because EELS is only sensitive towards changes of the electrical field along the electron-beam direction. Only additional experiments may shed further light on the topic and may enable the derivation of the complete understanding of the involved physical processes.

Bibliography

1. Barnes, W. L.; Dereux, A.; Ebbesen, T. W. Surface plasmon subwavelength optics. *Nature* **2003**, 424, 824-830.

2. Zia, R.; Schuller, J. A.; Chandran, A.; Brongersma, M. L. Plasmonics: the next chip-scale technology. *Mater. Today* **2006**, 9, 20-27.

3. Brongersma, M. L.; Zia, R.; Schuller, J. A. Plasmonics - the missing link between nanoelectronics and microphotonics. *Appl Phys a-Mater* **2007**, 89, 221-223.

4. Seago, A. E.; Brady, P.; Vigneron, J.-P.; Schultz, T. D. Gold bugs and beyond: a review of iridescence and structural colour mechanisms in beetles (Coleoptera). **2009**, 6, S165-S184.

5. Freestone, I.; Meeks, N.; Sax, M.; Higgitt, C. The Lycurgus Cup - A Roman nanotechnology. *Gold Bull.* **2007**, 40, 270-277.

6. Sepulveda, B.; Angelome, P. C.; Lechuga, L. M.; Liz-Marzan, L. M. LSPR-based nanobiosensors. *Nano Today* **2009**, 4, 244-251.

7. Nie, S.; Emory, S. R. Probing Single Molecules and Single Nanoparticles by Surface-Enhanced Raman Scattering. *Science* **1997**, 275, 1102-1106.

8. Ebbesen, T. W.; Lezec, H. J.; Ghaemi, H. F.; Thio, T.; Wolff, P. A. Extraordinary optical transmission through sub-wavelength hole arrays. *Nature* **1998**, 391, 667-669.

9. Egerton, R. F. *Electron energy-loss spectroscopy in the electron microscope*. Plenum Press: New York, **1986**.

10. Maier, S. A. *Plasmonics: Fundamentals and Applications*. Springer Science LLC: New York, **2007**.

11. Otto, A. Excitation of Nonradiative Surface Plasma Waves in Silver by Method of Frustrated Total Reflection. *Z. Angew. Phys.* **1968**, 216, 398-&.

12. Kretschmann, E.; Raether, H. Radiative Decay of Non Radiative Surface Plasmons Excited by Light. *Z Naturforsch Pt A* **1968**, A 23, 2135-&.

13. Jackson, J. D. *Classical Electrodynamics*. John Wiley & Sons: New York, **1962**.

14. Carmeli, I.; Itskovsky, M. A.; Kauffmann, Y.; Shaked, Y.; Richter, S.; Maniv, T.; Cohen, H. Far- and near-field electron beam detection of hybrid cavity-plasmonic modes in gold microholes. *Phys. Rev. B* **2012**, 85, 041405-5.

15. Schlüter, M. Elektronenspektrometrische Untersuchungen zur Natur des 2,48 eV-Energieverlustes von Gold. *Z. Angew. Phys.* **1971**, 247, 263-266.

16. Crewe, A. V. Electron microscopes using field emission source. *Surf. Sci.* **1975**, 48, 152-160.

17. Treacy, M. M. J.; Howie, A.; Wilson, C. J. Z-Contrast of Platinum and Palladium Catalysts. *Philos Mag A* **1978**, 38, 569-585.

18. Williams, D. B.; Carter, C. B. *Transmission Electron Microscopy - A Textbook for Materials Science*. Second Edition ed.; Springer Science LLC: New York, **2009**.

19. Reimer, L.; Kohl, H. *Transmission Electron Microscopy - Physics of Image Formation*. Fifth Edition ed.; Springer Sciene LLC: New York, **2008**.

20. García de Abajo, F. J. Optical excitations in electron microscopy. *Rev. Mod. Phys.* **2010**, 82, 209-275.

21. Raether, H. *Excitation of Plasmons and Interband Transistions by Electrons*. Springer: Berlin Heidelberg New York, **1980**.

22. Reimer, L. *Energy-Filtering Transmission Electron Microscopy*. Springer: Heidelberg, **1995**.

23. Boersch, H.; Geiger, J.; Hellwig, H. Steigerung Der Auflosung Bei Der Elektronen-Energieanalyse. *Phys Lett* **1962**, 3, 64-66.

24. Boersch, H.; Geiger, J.; Stickel, W. Das Auflösungsvermögen des elektrostatisch-magnetischen Energieanalysators für schnelle Elektronen. *Z. Angew. Phys.* **1964**, 180, 415-424.

25. Wang, Z. L.; Cowley, J. M. Surface-Plasmon Excitation for Supported Metal Particles. *Ultramicroscopy* **1987**, 21, 77-93.

26. Wang, Z. L.; Cowley, J. M. Generation of Surface-Plasmon Excitation of Supported Metal Particles by an External Electron-Beam. *Ultramicroscopy* **1987**, 21, 347-365.

27. Wang, Z. L.; Cowley, J. M. Size and Shape Dependence of the Surface-Plasmon Frequencies for Supported Metal-Particle Systems. *Ultramicroscopy* **1987**, 23, 97-107.

28. Cohen, H.; Maniv, T.; Tenne, R.; Hacohen, Y. R.; Stephan, O.; Colliex, C. Near-field electron energy loss spectroscopy of nanoparticles. *Phys. Rev. Lett.* **1998**, 80, 782-785.

29. Nelayah, J.; Kociak, M.; Stephan, O.; de Abajo, F. J. G.; Tence, M.; Henrard, L.; Taverna, D.; Pastoriza-Santos, I.; Liz-Marzan, L. M.; Colliex, C. Mapping surface plasmons on a single metallic nanoparticle. *Nat. Phys.* **2007**, 3, 348-353.

30. Bosman, M.; Keast, V. J.; Watanabe, M.; Maaroof, A. I.; Cortie, M. B. Mapping surface plasmons at the nanometre scale with an electron beam. *Nanotechnology* **2007**, 18, 165505-5.

31. Schaffer, B.; Riegler, K.; Kothleitner, G.; Grogger, W.; Hofer, F. Monochromated, spatially resolved electron energy-loss spectroscopic measurements of gold nanoparticles in the plasmon range. *Micron* **2009**, 40, 269-273.

32. Guiton, B. S.; Iberi, V.; Li, S. Z.; Leonard, D. N.; Parish, C. M.; Kotula, P. G.; Varela, M.; Schatz, G. C.; Pennycook, S. J.; Camden, J. P. Correlated Optical Measurements and Plasmon Mapping of Silver Nanorods. *Nano Lett.* **2011**, 11, 3482-3488.

33. Koh, A. L.; Fernandez-Dominguez, A. I.; McComb, D. W.; Maier, S. A.; Yang, J. K. W. High-Resolution Mapping of Electron-Beam-Excited Plasmon Modes in Lithographically Defined Gold Nanostructures. *Nano Lett.* **2011**, 11, 1323-1330.

34. Mazzucco, S.; Stephan, O.; Colliex, C.; Pastoriza-Santos, I.; Liz-Marzan, L. M.; de Abajo, J. G.; Kociak, M. Spatially resolved measurements of plasmonic eigenstates in complex-shaped, asymmetric nanoparticles: gold nanostars. *Eur Phys J-Appl Phys* **2011**, 54.

35. Chu, M. W.; Myroshnychenko, V.; Chen, C. H.; Deng, J. P.; Mou, C. Y.; de Abajo, F. J. G. Probing Bright and Dark Surface-Plasmon Modes in Individual and Coupled Noble Metal Nanoparticles Using an Electron Beam. *Nano Lett.* **2009**, 9, 399-404.

36. Mirsaleh-Kohan, N.; Iberi, V.; Simmons, P. D.; Bigelow, N. W.; Vaschillo, A.; Rowland, M. M.; Best, M. D.; Pennycook, S. J.; Masiello, D. J.; Guiton, B. S.; Camden, J. P. Single-Molecule Surface-Enhanced Raman Scattering: Can STEM/EELS Image Electromagnetic Hot Spots? *J. Phys. Chem. Lett.* **2012**, 3, 2303-2309.

37. Michaels, A. M.; Jiang, J.; Brus, L. Ag nanocrystal junctions as the site for surface-enhanced Raman scattering of single Rhodamine 6G molecules. *J. Phys. Chem. B* **2000**, 104, 11965-11971.

38. Nelayah, J.; Gu, L.; Sigle, W.; Koch, C. T.; Pastoriza-Santos, I.; Liz-Marzan, L. M.; van Aken, P. A. Direct imaging of surface plasmon resonances on single triangular silver nanoprisms at optical wavelength using low-loss EFTEM imaging. *Opt. Lett.* **2009**, 34, 1003-1005.

39. Schaffer, B.; Hohenester, U.; Trugler, A.; Hofer, F. High-resolution surface plasmon imaging of gold nanoparticles by energy-filtered transmission electron microscopy. *Phys. Rev. B* **2009**, 79.

40. Gu, L.; Sigle, W.; Koch, C. T.; Ogut, B.; van Aken, P. A.; Talebi, N.; Vogelgesang, R.; Mu, J. L.; Wen, X. G.; Mao, J. Resonant wedge-plasmon modes in single-crystalline gold nanoplatelets. *Phys. Rev. B* **2011**, 83.

41. Sigle, W.; Nelayah, J.; Koch, C. T.; van Aken, P. A. Electron energy losses in Ag nanoholes-from localized surface plasmon resonances to rings of fire. *Opt. Lett.* **2009**, 34, 2150-2152.

42. Sigle, W.; Nelayah, J.; Koch, C. T.; Ogut, B.; Gu, L.; van Aken, P. A. EFTEM study of surface plasmon resonances in silver nanoholes. *Ultramicroscopy* **2010**, 110, 1094-1100.

43. Liu, N.; Giessen, H. Coupling Effects in Optical Metamaterials. *Angew Chem Int Edit* **2010**, 49, 9838-9852.

44. von Cube, F.; Irsen, S.; Diehl, R.; Niegemann, J.; Busch, K.; Linden, S. From Isolated Metaatoms to Photonic Metamaterials: Evolution of the Plasmonic Near-Field. *Nano Lett.* **2013**, 13, 703-708.

45. Boudarham, G.; Feth, N.; Myroshnychenko, V.; Linden, S.; de Abajo, J. G.; Wegener, M.; Kociak, M. Spectral Imaging of Individual Split-Ring Resonators. *Phys. Rev. Lett.* **2010**, 105.

46. Pelton, M.; Aizpurua, J.; Bryant, G. Metal-nanoparticle plasmonics. *Laser Photonics Rev.* **2008**, 2, 136-159.

47. Vogelgesang, R.; Dmitriev, A. Real-space imaging of nanoplasmonic resonances. *Analyst* **2010**, 135, 1175-1181.

48. Ringe, E.; Sharma, B.; Henry, A. I.; Marks, L. D.; Van Duyne, R. P. Single nanoparticle plasmonics. *PCCP* **2013**, 15, 4110-4129.

49. Bosman, M.; Keast, V. J. Optimizing EELS acquisition. *Ultramicroscopy* **2008**, 108, 837-46.

50. Barfels, M.; Burgner, P.; Edwards, R.; Brink, H. A new high stability, 4th order aberration corrected spectrometer and imaging filter for a monochromated TEM. *Microsc. Microanal.* **2002**, 8, 614-615.

51. Gubbens, A.; Barfels, M.; Trevor, C.; Twesten, R.; Mooney, P.; Thomas, P.; Menon, N.; Kraus, B.; Mao, C.; McGinn, B. The GIF Quantum, a next generation post-column imaging energy filter. *Ultramicroscopy* **2010**, 110, 962-970.

52. Terauchi, M.; Tanaka, M.; Tsuno, K.; Ishida, M. Development of a high energy resolution electron energy-loss spectroscopy microscope. *J. Microsc.* **1999**, 194, 203-209.

53. Tiemeijer, P. C.; van Lin, J. H. A.; Freitag, B. H.; de Jong, A. F. Monochromized 200kV (S)TEM. *Microsc. Microanal.* **2002**, 8, 70-71.

54. Mitterbauer, C.; Kothleitner, G.; Grogger, W.; Zandbergen, H.; Freitag, B.; Tiemeijer, P.; Hofer, F. Electron energy-loss near-edge structures of 3d transition metal oxides recorded at high-energy resolution. *Ultramicroscopy* **2003**, 96, 469-480.

55. Essers, E.; Benner, G.; Mandler, T.; Meyer, S.; Mittmann, D.; Schnell, M.; Hoschen, R. Energy resolution of an Omega-type monochromator and imaging properties of the MANDOLINE filter. *Ultramicroscopy* **2010**, 110, 971-980.

56. Krivanek, O. L.; Lovejoy, T. C.; Dellby, N.; Carpenter, R. W. Monochromated STEM with a 30 meV-wide, atom-sized electron probe. *Microscopy* **2013**, 62, 3-21.

57. Richardson, W. H. Bayesian-Based Iterative Method of Image Restoration. *J. Opt. Soc. Am.* **1972**, 62, 55-59.

58. Lucy, L. B. An iterative technique for the rectification of observed distributions. *Astron. J.* **1974**, 79, 745.

59. Snyder, D. L.; Helstrom, C. W.; Lanterman, A. D.; Faisal, M.; White, R. L. In *Compensation for Read-Out Noise in HST Image Restoration*, The Restoration of HST Images and Spectra - II, Baltimore, Maryland, Hanisch, R. J.; White, R. L., Eds. Space Telescope Science Institute: Baltimore, Maryland, 1994; pp 139-154.

60. Molina, R.; Mateos, J.; Abad, J. Prior Models and the Richardson-Lucy Restoration Method. In *The Restoration of HST Images and Spectra - II*, Hanisch, R. J.; White, R. L., Eds. Space Telescope Science Institute: Baltimore, Maryland, 1994; pp 118-122

61. Boden, A. F.; Redding, D. C.; Hanisch, R. J.; Mo, J. Massively parallel spatially variant maximum-likelihood restoration of hubble space telescope imagery. *Journal of the Optical Society of America a-Optics Image Science and Vision* **1996**, 13, 1537-1545.

62. Zuo, J. M. Electron detection characteristics of a slow-scan CCD camera, imaging plates and film, and electron image restoration. *Microsc. Res. Tech.* **2000**, 49, 245-68.

63. Gloter, A.; Douiri, A.; Tence, M.; Colliex, C. Improving energy resolution of EELS spectra: an alternative to the monochromator solution. *Ultramicroscopy* **2003**, 96, 385-400.

64. Lazar, S.; Botton, G. A.; Zandbergen, H. W. Enhancement of resolution in core-loss and low-loss spectroscopy in a monochromated microscope. *Ultramicroscopy* **2006**, 106, 1091-103.

65. Bellido, E. P.; Rossouw, D.; Botton, G. A. Toward 10 meV Electron Energy-Loss Spectroscopy Resolution for Plasmonics. *Microsc. Microanal.* **2014**, FirstView, 1-12.

66. Rossouw, D.; Botton, G. A. Plasmonic Response of Bent Silver Nanowires for Nanophotonic Subwavelength Waveguiding. *Phys. Rev. Lett.* **2013**, 110, 066801-5.

67. Al-Bakkar, A. G.; Ipson, S. S.; Porter, G. J.; Gleed, D. G. A parallel implementation of a modified Richardson-Lucy algorithm for image de-blurring. *Int. J. Infrared Millimeter Waves* **1997**, 18, 555-575.

68. Aguiar, J. A.; Reed, B. W.; Ramasse, Q. M.; Erni, R.; Browning, N. D. Quantifying the low-energy limit and spectral resolution in valence electron energy loss spectroscopy. *Ultramicroscopy* **2013**, 124, 130-138.

69. Krivanek, O. L.; Lovejoy, T. C.; Dellby, N.; Aoki, T.; Carpenter, R. W.; Rez, P.; Soignard, E.; Zhu, J. T.; Batson, P. E.; Lagos, M. J.; Egerton, R. F.; Crozier, P. A. Vibrational spectroscopy in the electron microscope. *Nature* **2014**, 514, 209-+.

70. Matyssek, C.; Niegemann, J.; Hergert, W.; Busch, K. Computing electron energy loss spectra with the Discontinuous Galerkin Time-Domain method. *Photonics Nanostruct.* **2011**, 9, 367-373.

71. Busch, K.; Konig, M.; Niegemann, J. Discontinuous Galerkin methods in nanophotonics. *Laser Photonics Rev.* **2011**, 5, 773-809.

72. Johnson, P. B.; Christy, R. W. Optical Constants of Noble Metals. *Phys. Rev. B* **1972**, 6, 4370-4379.

73. Genet, C.; Ebbesen, T. W. Light in tiny holes. *Nature* **2007**, 445, 39-46.

74. Coe, J. V.; Heer, J. M.; Teeters-Kennedy, S.; Tian, H.; Rodriguez, K. R. Extraordinary transmission of metal films with arrays of subwavelength holes. *Annu. Rev. Phys. Chem.* **2008**, 59, 179-202.

75. Garcia-Vidal, F. J.; Martin-Moreno, L.; Ebbesen, T. W.; Kuipers, L. Light passing through subwavelength apertures. *Rev. Mod. Phys.* **2010**, 82, 729-787.

76. Bethe, H. Theory of Diffraction by Small Holes. *Phys Rev* **1944**, 66, 163-182.

77. Ghaemi, H. F.; Thio, T.; Grupp, D. E.; Ebbesen, T. W.; Lezec, H. J. Surface plasmons enhance optical transmission through subwavelength holes. *Phys. Rev. B* **1998**, 58, 6779-6782.

78. Martin-Moreno, L.; Garcia-Vidal, F. J.; Lezec, H. J.; Pellerin, K. M.; Thio, T.; Pendry, J. B.; Ebbesen, T. W. Theory of extraordinary optical transmission through subwavelength hole arrays. *Phys. Rev. Lett.* **2001**, 86, 1114-1117.

79. Krishnan, A.; Thio, T.; Kima, T. J.; Lezec, H. J.; Ebbesen, T. W.; Wolff, P. A.; Pendry, J.; Martin-Moreno, L.; Garcia-Vidal, F. J. Evanescently coupled resonance in surface plasmon enhanced transmission. *Optics Communications* **2001**, 200, 1-7.

80. Barnes, W. L.; Murray, W. A.; Dintinger, J.; Devaux, E.; Ebbesen, T. W. Surface plasmon polaritons and their role in the enhanced transmission of light through periodic arrays of subwavelength holes in a metal film. *Phys. Rev. Lett.* **2004**, 92.

81. Koerkamp, K. J. K.; Enoch, S.; Segerink, F. B.; van Hulst, N. F.; Kuipers, L. Strong influence of hole shape on extraordinary transmission through periodic arrays of subwavelength holes. *Phys. Rev. Lett.* **2004**, 92.

82. Zayats, A. V.; Smolyaninov, I. I.; Maradudin, A. A. Nano-optics of surface plasmon polaritons. *Phys. Rep.* **2005**, 408, 131-314.

83. Garcia-Vidal, F. J.; Moreno, E.; Porto, J. A.; Martin-Moreno, L. Transmission of light through a single rectangular hole. *Phys. Rev. Lett.* **2005**, 95.

84. Garcia-Vidal, F. J.; Martin-Moreno, L.; Moreno, E.; Kumar, L. K. S.; Gordon, R. Transmission of light through a single rectangular hole in a real metal. *Phys. Rev. B* **2006**, 74.

85. Lalanne, P.; Hugonin, J. P.; Rodier, J. C. Theory of surface plasmon generation at nanoslit apertures. *Phys. Rev. Lett.* **2005**, 95.

86. Itskovsky, M. A.; Cohen, H.; Maniv, T. Radiative interaction of a focused relativistic electron beam in energy-loss spectroscopy of nanoscopic platelets. *Phys. Rev. B* **2008**, 78.

87. Alaverdyan, Y.; Sepulveda, B.; Eurenius, L.; Olsson, E.; Kall, M. Optical antennas based on coupled nanoholes in thin metal films. *Nat. Phys.* **2007**, 3, 884-889.

88. Rindzevicius, T.; Alaverdyan, Y.; Sepulveda, B.; Pakizeh, T.; Kall, M.; Hillenbrand, R.; Aizpurua, J.; de Abajo, F. J. G. Nanohole plasmons in optically thin gold films. *J. Phys. Chem. C* **2007**, 111, 1207-1212.

89. Ögüt, B.; Vogelgesang, R.; Sigle, W.; Talebi, N.; Koch, C. T.; van Aken, P. A. Hybridized metal slit eigenmodes as an illustration of Babinet's principle. *ACS Nano* **2011**, 5, 6701-6.

90. Koch, C. T.; Sigle, W.; Höschen, R.; Rühle, M.; Essers, E.; Benner, G.; Matijevic, M. SESAM: Exploring the Frontiers of Electron Microscopy. *Microsc. Microanal.* **2006**, 12, 506-514.

91. Prangsma, J. C.; van Oosten, D.; Kuipers, L. Local investigation of the optical properties of subwavelength rectangular holes with a focused beam of electrons. *Philos T R Soc A* **2011**, 369, 3456-3471.

92. Nicoletti, O.; Wubs, M.; Mortensen, N. A.; Sigle, W.; van Aken, P. A.; Midgley, P. A. Surface plasmon modes of a single silver nanorod: an electron energy loss study. *Opt. Express* **2011**, 19, 15371-15379.

93. Alber, I.; Sigle, W.; Muller, S.; Neumann, R.; Picht, O.; Rauber, M.; van Aken, P. A.; Toimil-Molares, M. E. Visualization of Multipolar Longitudinal and Transversal Surface Plasmon Modes in Nanowire Dimers. *ACS Nano* **2011**, 5, 9845-9853.

94. Rossouw, D.; Couillard, M.; Vickery, J.; Kumacheva, E.; Botton, G. A. Multipolar Plasmonic Resonances in Silver Nanowire Antennas Imaged with a Subnanometer Electron Probe. *Nano Lett.* **2011**, 11, 1499-1504.

95. Alber, I.; Sigle, W.; Demming-Janssen, F.; Neumann, R.; Trautmann, C.; van Aken, P. A.; Toimil-Molares, M. E. Multipole Surface Plasmon Resonances in Conductively Coupled Metal Nanowire Dimers. *ACS Nano* **2012**, 6, 9711-9717.

96. Liang, H. Y.; Zhao, H. G.; Rossouw, D.; Wang, W. Z.; Xu, H. X.; Botton, G. A.; Ma, D. L. Silver Nanorice Structures: Oriented Attachment-Dominated Growth, High Environmental Sensitivity, and Real-Space Visualization of Multipolar Resonances. *Chem. Mater.* **2012**, 24, 2339-2346.

97. Liang, H. Y.; Rossouw, D.; Zhao, H. G.; Cushing, S. K.; Shi, H. L.; Korinek, A.; Xu, H. X.; Rosei, F.; Wang, W. Z.; Wu, N. Q.; Botton, G. A.; Ma, D. L. Asymmetric Silver "Nanocarrot" Structures: Solution Synthesis and Their Asymmetric Plasmonic Resonances. *J. Am. Chem. Soc.* **2013**, 135, 9616-9619.

98. Slater, J. C.; Frank, N. F. *Introduction to Theoretical Phyics*. McGraw-Hill Book Company: New York, **1933**.

99. Ibach, H.; Lüth, H. *Festkörperphysik*. Springer-Verlag: Berlin Heidelberg, **2002**.

100. Dionne, J. A.; Sweatlock, L. A.; Atwater, H. A.; Polman, A. Planar metal plasmon waveguides: frequency-dependent dispersion, propagation, localization, and loss beyond the free electron model. *Phys. Rev. B* **2005**, 72.

101. Hecht, E. *Optik*. Oldenbourg: München, **2005**.

102. Haus, H. A.; Huang, W. P. Coupled-Mode Theory. *Proc. IEEE* **1991**, 79, 1505-1518.

103. Walther, R.; Carmeli, I.; Schneider, R.; Gerthsen, D.; Busch, K.; Matyssek, C.; Shvarzman, A.; Maniv, T.; Richter, S.; Cohen, H. Interslit Coupling via Ultrafast Dynamics across Gold-Film Hole Arrays. *The Journal of Physical Chemistry C* **2014**, 118, 11043-11049.

104. Schaffer, B.; Grogger, W.; Kothleitner, G.; Hofer, F. Comparison of EFTEM and STEM EELS plasmon imaging of gold nanoparticles in a monochromated TEM. *Ultramicroscopy* **2010**, 110, 1087-1093.

105. Fernandez-Dominguez, A. I.; Garcia-Vidal, F. J.; Martin-Moreno, L. Resonant transmission of light through finite arrays of slits. *Phys. Rev. B* **2007**, 76.

List of Figures

List of Tables

Appendix

A. Implemented RL Algorithm Script

The self-written script to apply the RL algorithm on the acquired spectra is shown below. After //, commentaries are included to explain the algorithm. The implementation follows the pseudo-code reported by Al-Bakkar et al.[67]

```
RealImage _g, g0, _f0, f2, _f1, _psf, psf0

      number zlp, poscountmax, i, xsize_g, ysize_g, xsize_psf,
ysize_psf, zlpg, posg, n, shift_g0

      // get number of iterations

      GetNumber("Please specify the number of iterations to be
performed",n,n)

      if(!GetTwoLabeledImagesWithPrompt( "Please select a spectrum and a
ZLP", "data collection", "ZLP", psf0, "Spectrum", g0)) throw("It is
required you supply two spectra")

      GetSize(g0,xsize_g,ysize_g)
      GetSize(psf0,xsize_psf,ysize_psf)

      // get ZLP energy position

      Max(psf0,zlp,poscountmax)
      Max(g0,zlpg,posg)

      _psf = RealImage("PSF",8,2*xsize_psf,1)

      // embed spectra in larger space to avoid Fourier artifacts at the
data boundaries. PSF is centered to give a symmetric FFT.

      _psf[0,xsize_psf-zlp,1,xsize_psf-
zlp+xsize_psf]=psf0[0,0,1,xsize_psf]
      _psf/=sum(_psf)  // normalization of PSF so its integral is unity
(required by the algorithm in this form)

      _g := RealImage("_g",8,2*xsize_g,ysize_g)

      _g[0,xsize_g/2,1,3*xsize_g/2]=g0[0,0,1,xsize_g]

      // set first estimate of sharpened spectra to recorded spectra

      _f0 = _g
      ComplexImage PSF_ := ComplexImage ("PSF_",16,2*xsize_psf,1)
      PSF_ = RealFFT(_psf)

      // main algorithm

      for (i=0;i<n;i++)
            {

                  ComplexImage F_ := ComplexImage ("F_",16,2*xsize_psf,1)
                  ComplexImage A_ := ComplexImage ("A_",16,2*xsize_psf,1)
                  ComplexImage B_ := ComplexImage ("B_",16,2*xsize_psf,1)
```

```
                ComplexImage C_ := ComplexImage ("C_",16,2*xsize_psf,1)

                RealImage _a := RealImage("_a",4,2*xsize_g,1)
                RealImage _b := RealImage ("_b",8,2*xsize_g,1)
                RealImage _c := RealImage ("_c",8,2*xsize_g,1)

                F_ = RealFFT(_f0)
                A_ = PSF_ * F_
                _a = RealIFFT(A_)
                _b = _g/_a
                B_ = RealFFT(_b)
                C_ = B_*PSF_
                _c = RealIFFT(C_)
                _f0 = _f0*_c
            }

      // set result

      f2 := RealImage(ImageGetName(g0) + " - " + n + "
It.",4,xsize_g,ysize_g)
      f2 [0,0,ysize_g,xsize_g] = _f0 [0,xsize_g/2,1,3*xsize_g/2]

      number zlpf,poscountmaxf
      Max(f2,zlpf,poscountmaxf)

      // set result's calibration and tag group (to be recognized as
EELS spectrum)

      Max(g0,zlpg,posg)

      ImageSetDimensionCalibration(f2, 0, (-
zlpf+0)*ImageGetDimensionScale(g0, 0), ImageGetDimensionScale(g0, 0),
ImageGetDimensionUnitString(g0,0), 0)

      TagGroup g0tg = g0.ImageGetTagGroup()
      TagGroup f2tg = f2.ImageGetTagGroup()
      TagGroupCopyTagsFrom(f2tg,g0tg)
      ShowImage(f2)
```

Own Publications and Contributions to Conferences

Reviewed Publications

- R. Walther, I. Carmeli, R. Schneider, D. Gerthsen, K. Busch, C. Matyssek, A. Shvarzman, T. Maniv, S. Richter, and H. Cohen. Interslit Coupling via Ultrafast Dynamics across Gold-Film Hole Arrays. The Journal of Physical Chemistry C **118**, 11043-11049 (2014)

- R. Walther and D. Gerthsen. On the First Application of the Richardson–Lucy Algorithm to Resolve Plasmonic Resonances in EELS Spectra Obtained with a Monochromated Electron Beam. Microscopy and Microanalysis **20**, 993-994 (2014)

Reviewed Publications on other Topics

- R. Walther, D. Litvinov, M. Fotouhi, R. Schneider, D. Gerthsen, R. Vöhringer, D. Z. Hu, and D. M. Schaadt. Microstructure of PAMBE-grown InN layers on Si(111). Journal of Crystal Growth **340**, 34-40 (2012)

Contributions to Conferences

- R. Walther, R. Schneider, E. Müller, I. Carmeli, S. Richter, T. Maniv, H. Cohen, and D. Gerthsen. Surface plasmon polariton mediated collective excitations of cavity resonances in gold sub-wavelength slit-arrays. *Proceedings of the European Microscopy Congress*, Manchester (2012)

- I. Carmeli, R. Walther, R. Schneider, D. Gerthsen, Y. Kauffmann, S. Richter, and H. Cohen. Near- and Far-field Spectroscopy of Au Slit Arrays Using STEM-EELS. *Proceedings of the 47th Annual Scientific Meeting of ISM*, Safed (2013)

- R. Walther, E. Müller, R. Schneider, H. Cohen, T. Maniv, and D. Gerthsen. Cavity standing waves in single slits and slit arrays in a thin Au film revealed by electron energy loss spectroscopy in a transmission electron microscope. *Proceedings of the Fundamental Optical Processes in Semiconductors*, Kodiak Island (2013)

- R. Walther, E. Müller, R. Schneider, and D. Gerthsen. Accessing low-energy cavity modes in rectangular slits in a thin Au film by STEM-EELS in combination with the Richardson-Lucy algorithm. *Proceedings of the Microscopy Congress*, Regensburg (2013)

- S. Fritz, R. Walther, R. Schneider, D. Gerthsen, C. Matyssek, K. Busch, T. Maniv, and H. Cohen. Surface-plasmon-polariton coupling between adjacent submicron slits in a Au-film investigated by STEM-EELS. *Proceedings of the International Microscopy Congress*, Prague (2014)

Contributions to Conferences on other Topics

- R. Walther, D. Litvinov, R. Schneider, M. Fotouhi, D. Gerthsen, R. Vöhringer, D. Z. Hu, and D. M. Schaadt. Structural analysis of InN/AlN/Si(111) heterostructures. *Proceedings of the Microscopy Conference*, Kiel (2011)

Danksagung

Prof. Dr. Dagmar Gerthsen danke ich herzlich für die exzellente Betreuung meiner Arbeit. Zudem bedanke ich mich für die guten Ratschläge und wertvollen Tipps bei Veröffentlichungen und Konferenzbeiträgen. Ihr umfangreiches Fachwissen half maßgeblich bei der Realisierung dieser Arbeit.

Bei Prof. Dr. Kurt Busch bedanke ich mich herzlichst für die Übernahme des Korreferats und die fruchtvollen Diskussionen rund um die Arbeit. Seine Blickweise auf die selbige von einem theoretischen Standpunkt aus zeigte wichtige Aspekte auf und half maßgeblich bei der Interpretation der Daten.

Reinhard Schneider danke ich für die Einweisungen in die Rastertransmissionselektronenmikroskopie und die Elektronenenergieverlustspektroskopie.

Stefan Fritz gilt außerordentlicher Dank. Die etlichen Messungen, die er während seiner Masterarbeit mit großer Geduld und Ausdauer vornahm, trugen maßgeblich zu einem besseren Verständnis der Kopplungsphänomene bei.

Sincere thanks are due to Hagai Cohen for the fruitful discussions and his countless emails that continuously pushed for additional data to acquire and meticulous evaluation of existing one to find the big picture explaining our experiments.

Special thanks go to Tsofar Maniv for the insightful discussions during his visits which helped tremendously in the interpretation and understanding of the experimental data.

Christian Matyssek möchte ich für die zahlreichen Simulationen danken.

Mein besonderer Dank gilt Erich Müller, der enorme Geduld bei der Präparation der Schlitzstrukturen aufbrachte. Und vielen Dank für die zahlreichen philosophischen Diskussionen, die wir während der Präparation (und im Kaffeeraum) führten.

Simon Hettler und Manuel Dries danke ich für die Herstellung der verwendeten Goldfilme.

Frau Sauter danke ich herzlichst für ihre großzügige Unterstützung in Verwaltungsangelegenheiten und ihr offenes Ohr bei allerlei sonstigen Angelegenheiten.

Natürlich geht auch ein großes Dankeschön an alle aktuellen und ehemaligen Kolleginnen und Kollegen, ohne die die Zeit am LEM nicht halb so schön gewesen wäre. Danke für eure tatkräftige Unterstützung, die es mir erst ermöglicht hat diese Arbeit durchzuführen, und für die lustigen Kaffeepausen und die vielen lockeren Abende am Institut. Und natürlich für das unzählige Feingebäck!

Ganz besonders herzlicher Dank gilt meiner Familie und deren Unterstützung während des Studiums, der Promotionszeit und auch sonst.